Universal scaling and coherence properties of an ultracold Rydberg gas

Von der Fakultät Mathematik und Physik der Universität Stuttgart
zur Erlangung der Würde eines Doktors der
Naturwissenschaften (Dr. rer. nat.) genehmigte Abhandlung

vorgelegt von
Ulrich Krohn
aus Göppingen

Hauptberichter:	Prof. Dr. Tilman Pfau
Mitberichter:	Prof. Dr. Charles Adams
Prüfungsvorsitzender:	Prof. Dr. Hans Peter Büchler

Tag der mündlichen Prüfung: 4. November 2008

5. Physikalisches Institut
Universität Stuttgart

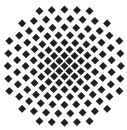

Cover picture

The picture on the front cover shows a photography of a magneto-optical trap with approximately 5×10^{10} rubidium atoms that are illuminated by the blue laser light used for the Rydberg excitation.
The word cloud on the back illustrates the most often used words in this thesis and was produced using the online script that can be found at http://www.wordle.net/

D93 (Dissertation, Universität Stuttgart)

Contents

Zusammenfassung

Die vorliegende Arbeit behandelt die Anregung von ultrakalten Atomen aus dem Grundzustand in einen Rydberg-Zustand bei hohen atomaren Dichten. Rydberg-Zustände sind Zustände bei denen sich mindestens ein Elektron in einen energetisch hochangeregten Zustand, der über die Hauptquantenzahl n charakterisiert ist,befindet. Der klassische Radius des Orbits auf dem sich das Elektron um den Kern bewegt skaliert mit quadratisch mit der Hauptquantenzahl und nimmt Werte an, bei denen das Elektron nur noch schwach an den Kern gebunden ist. Die schwache Bindung des Elektrons an den Kern führt zu einer hohen Polarisierbarkeit des Rydberg-Atoms, die mit n^7 skaliert. Da Rydberg-Atome kein permanentes Dipolmoment besitzen ist die van-der-Waals-Wechselwirkung $\mathcal{V}_{\mathrm{vdW}} = {}^{C_6}/_{r^6}$ dominierend. Der C_6-Koeffizient skaliert auf Grund der hohen Polarisierbarkeit mit n^{11}, das heißt schon bei der Anregung von Atomen in relativ niedrige Rydberg-Zustände gibt die van-der-Waals-Wechselwirkung die dominierende Energieskala an.

Die Entdeckung der Rydberg-Atome geht bis in das neunzehnte Jahrhundert zurück und wurde im Wesentlichen von dem schwedischen Physiker, und Namensgeber dieser hochangeregten Zustände, Johannes Rydberg vorangetrieben. Die von ihm und seinen Vorgänger gefundenen empirischen Gesetze vermochten die beobachteten Linienspektren zwar zu beschreiben, der fundamentale fundamentale physikalische Zusammenhang ihres Auftretens wurde allerdings erst mit Hilfe der Quantenmechanik erklärbar.

Anfängliche Beobachtungen von Rydberg-Atomen waren auf Umgebungen wie Plasmen oder den stellaren Raum beschränkt, da dort die für die Anregung nötigen Energien zur Verfügung stehen. Erst die Entwicklung des Lasers 1960 machte eine selektive Anregung von Rydberg-Zuständen in atomaren Gasen bei Raumtemperatur und Atomstrahlexperimenten möglich. Bis vor ungefähr 20 Jahren wurden die Eigenschaften der Rydberg-Atome intensiv in diesen Systemen untersucht. Die Linienbreiten der beobachteten Spektren waren allerdings durch die Doppler-Verbreiterung oder durch die Verbreiterung auf Grund der kurzen Durchflugzeit durch die Anregungszone limitiert. Dies änderte sich grundlegend mit der Realisierung von Laserkühlverfahren und dem Fangen von Atomen in magneto-optischen Fallen, die Präzensionsmessungen an dreidimensional gefangenen ultrakalten Atomen zulässt. Die Verringerung der Temperatur um typische acht Größenordnungen führt zu einer Verringerung der Doppler-Verbreiterung und der Durchflugsver-

breiterung um fünf Größenordnungen.

Für die Entdeckung der Laserkühlung und deren Beschreibung erhielten S. Chu, C. Cohen-Tannoudji und W. D. Philips den Nobelpreis für Physik im Jahre 1997 [Chu98, CT98, Phi98]. Des Weiteren führte die Laserkühlung, welche den ersten Schritt in fast allen Experimenten mit ultrakalten Atomen darstellt, und die weitere Entwicklung verschiedener anderer Kühlverfahren 1995 zur ersten Erzeugung eines quantenentarteten Gases von bosonischen Atomen und Temperaturen im Bereich von einigen Nano-Kelvin. Die so genannte Bose-Einstein-Kondensation wurde bereits 1924 von S. N. Bose und A. Einstein vorhergesagt [Bos24, Ein24, Ein25]. Die im selben Jahr veröffentliche Dissertation von L. V. de Broglie sagt ebenfalls das Auftreten einer Quantenentartung auf Grund des Welle-Teilchen-Dualismus von Atomen für niedrige Temperaturen voraus [dB24]. Die experimentelle Realisierung der Bose-Einstein-Kondensation wurde 2001 mit dem Nobelpreis für Physik für E. A. Cornell, C. E. Wieman und W. Ketterle gewürdigt [Cor02, Ket02].

Für die Forschung an Rydberg-Atomen ergeben sich durch Herstellung von ultrakalten atomaren Gasen völlig neue Perspektiven. Herausragend ist dabei zum einen die Möglichkeit Experimente auf einer Zeitskala durchzuführen auf der sich die Atome nicht bewegen da die Bewegungsfreiheitsgrade größtenteils ausgefroren sind. In diesem Zusammenhang hat sich der Begriff der 'gefrorenen Rydberg-Gase' etabliert. Eine weiterer wichtiger Vorteil der Experimente in einem gefrorenen Rydberg-Gas ist die Möglichkeit vergleichsweise hohe Dichten, in dem in dieser Arbeit vorgestellten Experiment bis mehreren $10^{20}\,\mathrm{m}^{-3}$, zu erreichen. Die Wechselwirkung zwischen den Rydberg-Atomen ist stark von atomaren Dichte Abhängig, so dass diese Wechselwirkung mit der Variation der Dichte eingestellt werden kann.

Allen Experimenten mit ultrakalten atomaren Gasen ist gemein, dass die Wechselwirkung zwischen den Atomen die entscheidende Rolle spielt. Die Vielfalt an beobachteten physikalischen Phänomenen ist allein auf die verschiedenen Wechselwirkungen, sowie deren stärke zurückzuführen. Die Wechselwirkung zwischen den Rydberg-Atomen führt zu einer energetischen Verschiebung der Rydberg-Zustände von Atomen in der Nähe eines bereits angeregten Rydberg-Atoms. Ist die Wechselwirkung stark genug, so wird das durch den Anregungslaser sättigunsverbreiterte Energieniveau des Rydberg-Zustands soweit verschoben, dass der Übergang aus der Resonanz bezüglich des Anregungslasers mit der Kopplungsstärke Ω_0 geschoben wird und keine Anregung in den Rydberg-Zustand mehr stattfindet. Somit führt eine starke Wechselwirkung zu einer Blockade der Rydberg-Anregung in einem kugelförmigen Volumen mit dem Blockaderadius r_b.

Die in dieser Arbeit betrachteten Rydberg-Atome befinden sich in dem Zustand $43\mathrm{S}_{1/2}$, welcher ausschließlich eine repulsive van-der-Waals-Wechselwirk-

ung $\mathcal{V}_{\mathrm{vdW}} = -C_6/r^6$ aufweist. Dabei hat C_6 für den $43S_{1/2}$-Rydberg-Zustand einen Wert von $-1.6 \times 10^{-60}\,\mathrm{Jm}^6$ [Sin05], wohingegen der Wert im Grundzustand $C_6 = 4.5 \times 10^{-76}\,\mathrm{Jm}^6$ um 16 Größenordnungen kleiner ist [Dal66]. Formal kann der Blockaderadius als $r_\mathrm{b} = \sqrt[6]{|C_6|/\hbar\Omega}$ angegeben werden und nimmt in dem hier vorgestellten Experiment Werte für den $43S_{1/2}$-Zustand im Bereich von 5 µm an. Aus diesem Argument ist ersichtlich, dass sich in einer Blockadekugel bis zu mehrere tausend Grundzustandsatome befinden.

Die Anregung in den Rydberg-Zustand kann nicht einem bestimmten Atom in der Blockadekugel zugeordnet werden, sondern wird kollektiv von allen N Atomen in dem Volumen getragen. Die Beschreibung dieses verschränkten Zustands kann als effektives Zweiniveauatom erfolgen, wodurch sich der Begriff des 'Superatom' für die Beschreibung des kollektiven Zustands von mehreren tausend Atomen durchgesetzt hat [Vul06]. Das auftreten einer kollektiven Anregung von N Grundzustandsatomen kann durch die Messung der Zeitentwicklung zwischen Grundzustand und Rydberg-Zustand erfolgen. Das Dipolmatrixelement, dass diese Kopplung beschreibt, geht in die Rabi-Frequenz Ω_0 ein. Die Normierung des symmetrisierten kollektiven Zustandes resultiert in einer kollektiven Rabi-Frequenz $\Omega_\mathrm{c} = \sqrt{N}\Omega_0$, die gegenüber der Einzelatom-Rabi-Frequenz Ω_0 um einen Faktor $\sqrt{N}$ größer ist.

Das Auftreten des kollektiven Zustands und die damit verbundene kollektive Rabi-Frequenz wurde erstmals mit dem in dieser Arbeit besprochenen experimentellen Aufbau untersucht und in den Referenzen [Hei07, Hei08a] dokumentiert. Um die Dynamik der Rydberg-Anregung zu untersuchen wurde die Anzahl der Atome im Rydberg-Zustand für verschiedene Anregungszeiten gemessen. Die resultierende Anregungskurve zeigt in erster Näherung ein exponentielles Sättigungsverhalten für lange Anregungszeiten. Die Dynamik der Rydberg-Anregung wurde bereits für wesentlich kleinere Dichten in den Referenzen [Ton04, Sin04b, Vog06] untersucht.

Aus der Skalierung der Rate, mit der die Rydberg-Atomzahl für kurze Anregungszeiten ansteigt, und der Grundzustandsdichte, sowie der Laserleistung, die Proportional zu Ω_0^2 ist, konnte gezeigt werden, dass die Anregung in den Rydberg-Zustand sowohl kollektiv als auch kohärent ist. Aus der Skalierung des Sättigungswertes konnte gezeigt werden, dass die Wechselwirkung zwischen den Rydberg-Atomen durch die van-der-Waals-Wechselwirkung dominiert wird. Des Weiteren wurde gezeigt, dass die Anregung auf Grund der Wechselwirkung stark blockiert ist. Aufbauend auf diesen Ergebnissen sollen in dieser Arbeit weitere Aspekte der Rydberg-Anregung und der Wechselwirkung zwischen den Rydberg-Atomen untersucht werden.

Universelle Skalierung

Die weitere Untersuchung der Rydberg-Anregungsdynamik geschieht im Hinblick auf die Untersuchung einer universellen Skalierung nach der die charakteristischen Größen der Rydberg-Anregungsdynamik, nämlich die anfängliche Rate und der Sättigungswert, mit Potenzgesetzen skalieren, dessen Exponenten universell sind. Eine solche universelle Skalierung wurde von der Arbeitsgruppe um H. P. Büchler an der Universität Stuttgart für die Anregung von Rydberg-Atomen vorhergesagt [Wei08].

Universelle Skalierungen sind in allen Teilen der Physik, aber auch darüber hinaus, von großem Nutzen, da sie das Verhalten vieler sich ähnlicher Systeme voraussagen, ohne dass das Wissen der genauen mikroskopische Realisierung nötig ist. Beispiele aus vielen Bereichen der Natur können zum Beispiel in Referenz [Wes04] gefunden werden. In dieser Veröffentlichung wird beispielsweise geschildert wie die Metabolismusrate mit der Masse von Organismen nach einem Potenzgesetz, welches die selben Exponenten für eine Variation der Masse über 27 Größenordnungen zeigt, skaliert. In Referenz [Gug45] werden die physikalischen Eigenschaften verschiedenster Atome und Moleküle in der Nähe eines Phasenübergangs zweiter Ordnung untersucht und nachgewiesen, dass sich alle Substanzen nach den gleichen Potenzgesetzen verhalten. Generell kann das Auftreten von universellen Skalierungen in der Nähe eines kritischen Punktes eines Phasenübergangs zweiter Ordnung gezeigt werden [Hua87].

Im Falle der Anregung vom Rydberg-Atomen ist die genaue mikroskopische Realisierung, das heißt die Abstände der Grundzustandsatome, die angeregt werden, Poisson-verteilt und damit ebenfalls unbekannt. Die globale Anregungsdynamik lässt allerdings Rückschlüsse auf das mikroskopische Verhalten zu. Der Phasenübergang wird zwischen der ‘paramagnetischen Phase’, in der sich kein Atom im Rydberg-Zustand befindet, und der ‘kristallinen Phase’ gebildet. Die kristalline Phase bildet sich durch die Anordnung der Superatome in einem kubischflächenzentrierten Kristall, da dies die Energie zwischen den Superatomen minimiert. Die physikalisch makroskopisch zugängliche Observable ist als der Anteil der Atome f, die sich im Rydberg-Zustand befinden bezogen auf den Anteil der Atome im Grundzustand.

Eine universelle Skalierung zu finden heißt nun, dass für jede das System beschreibende Variable ein Potenzgesetz existiert, das deren Verhalten um den kritischen Punkt des Phasenübergangs beschreibt. Im Fall der Rydberg-Anregung kann der Rydberg-Anteil f durch ein Potenzgesetz in dem Parameter $\alpha = {}^{\hbar\Omega}/_{C_6 n_\mathrm{g}^2}$ mit der Grundzustandsdichte n_g gefunden werden. Der dimensionsloser Parameter α vergleicht dabei die Anregungsenergie mit der Wechselwirkungsenergie.

Die vorliegende Arbeit berichtet über die Messungen um eine universel-

le Skalierung der Form $f \sim \alpha^{\nu}$ zu finden und die universellen Exponenten ν zu bestimmen. Durch Rückschlüsse, die aus dem Superatom-Modell gezogen werden können, wird erwartet das der universelle Exponent nur von der Dimensionalität der Atomwolke, sowie der Art der Wechselwirkung abhängt. Sämtliche Systemgrößen wie die atomare Dichte, die Rabi-Frequenz und der Koeffizient der van-der-Waals-Wechselwirkung sind in α zusammengefasst und führen zu keinem Beitrag in dem kritischen Exponenten. Eine Messung des kritischen Exponenten ν lässt also bei bekannter Wechselwirkung Rückschlüsse auf die Dimensionalität der Dichteverteilung der gefangenen Atome zu. Dabei ist die Dimensionalität immer in Bezug auf die Größe der Superatome, also des Blockaderadiuses, zu sehen. Eine eindimensionale Dichteverteilung kann beispielsweise durch einen zweidimensionalen Einschluss der Atomwolke auf Werte kleiner als der Blockaderadius erzeugt werden.

Die Messungen zur universellen Skalierung wurden daher sowohl in einer Magnetfalle als auch in einer Dipolfalle, die einen stärkeren Einschluss in zwei Dimensionen aufweist, durchgeführt. Die Daten die zur Bestimmung der kritischen Exponenten mit magnetisch gefangen Atomen aufgenommen wurden sind bereits in Referenz [Hei07] veröffentlicht. Obwohl die radiale Ausdehnung der atomaren Wolke in dieser Messung mit 8.7 µm größer als der Blockaderadius war, zeigte sich ein Skalierungsverhalten, das eher auf eine eindimensionale Dichteverteilung schliessen lässt. Die durchgeführten Messungen mit Atomen die in eine Dipolfalle geladen wurden führten im Wesentlichen zu den selben Ergebnissen. Obwohl der größere radiale Einschluss zu einer Verkleinerung der radialen Ausdehnung der Wolke um circa einen Faktor zwei führte, konnte dennoch keine eindeutige Tendenz der kritischen Exponenten in Richtung einer noch eindimensionaleren Situation als in der Magnetfalle gefunden werden. Daher werden in dieser Arbeit Vorschläge für die Durchführung künftiger Experimente, die in der Lage sein sollten eine eindimensionalere Situation zu erzeugen und die universelle Skalierung in Abhängigkeit der Dimensionalität der Dichteverteilung eingehender zu untersuchen, gegeben.

Bei den gezeigten Messungen ist insbesondere hervorzuheben das eine universelle Skalierung mit einem Potenzgesetz gefunden werden konnte. Der dimensionslose Parameter α wurde dazu über bis zu 15 Größen ordnungen variiert. Die Messungen zeigen in doppeltlogarithmischer Auftragung einen eindeutig linearen Zusammenhang, das heißt, dass der Zusammenhang zwischen dem Verhältnis der Atome im Rydberg-Zustand zu denen im Grundzustand durch ein Potenzgesetz gegeben der Form α^{ν} ist. Das Auftreten dieser universellen Skalierung ist ein deutliches Anzeichen dafür bei der stark blockierten Anregung in einen Rydberg-Zustand tatsächlich einen Quantenphasenübergang zweiter Ordnung finden zu können.

Dephasierungseffekte

Der zweite Teil der vorliegenden Arbeit widmet sich der Untersuchung der Wechselwirkungseffekte auf die Kohärenzeigenschaften der Rydberg-Anregung. Die mit den vorgestellten Messmethoden gewonnen Erkenntnisse sind insbesondere im Hinblick auf die Verwirklichung von Quantengattern, wie sie beispielsweise in den Referenzen [Jak00, Luk01] vorgeschlagen werden, interessant.

Jede Störung durch die Wechselwirkung der Rydberg-Atome mit ihrer Umgebung oder untereinander stellt eine mögliche Quelle der Dekohärenz oder der Dephasierung dar und würde eine Gatteroperation stören. In einem experimentellen Aufbau zur Implementierung von Quanteninformationsprozessen gilt es die verschiedenen Dekohärenzquellen zu beseitigen. Dies geschieht zum Beispiel durch die Kühlung der Atome und deren vollständigen Isolierung von der thermischen Umgebung. Des Weiteren finden die Experimente auf Zeitskalen statt, die kurz gegen die Lebensdauer der Rydberg-Zustände sind. Dadurch wird die Dekohärenz durch spontane Emission unterdrückt.

Die in einem solchen Aufbau präparierten Rydberg-Atome würden sich im Hinblick auf die Quanteninformationsverarbeitung besonders eignen, da der kollektive Zustand (Superatome) einen voll verschränkten Zustand darstellt, dessen Verschränkung äußerst robust gegenüber Anzahlfluktuationen ist. Derartige Zustände werden in der Literatur als W-Zustände bezeichnet [Dür00, Sto03].

Die in der vorliegenden Arbeit gezeigten Experimente sollen zum einen direkten Beweis der kohärenten Anregung in den Rydberg-Zustand geben, zum anderen sollen sie zwei Methoden vorstellen um die Wechselwirkungseffekte zwischen den Rydberg-Atomen zu quantifizieren.

Bereits die in Referenz [Hei07] gezeigten Messungen ließen den mit Hilfe von Skalierungsgesetzen gefundenen indirekten Schluss zu, dass die Anregung in den Rydberg-Zustand kohärent ist. Ein direkter Beweis über Rabi-Oszillationen, also Oszillationen der Population zwischen dem Grund- und dem Rydberg-Zustand, sind mit der in dieser Arbeit gezeigten Art von Experiment nicht möglich, da die inhomogene Dichteverteilung in der Magnetfalle zu einer inhomogenen Verteilung von kollektiven Rabi-Frequenzen $\sqrt{N}\Omega_0$ führt. Da in dem bestehenden System nicht ohne Weiteres möglich ist direkt einzelne Superatome zu beobachten, sondern nur das Ensemble, misst man die Summe über viele verschiedene Oszillationen, was zu den oben erwähnten Anregungskurven mit exponentieller Sättigung führt.

Ein direkten Nachweis der kohärenten Anregung von Rydberg-Atomen über die Beobachtung von Rabi-Oszillationen wird in den Referenzen [Joh08, RL08] für einzelnen Rydberg-Atome beziehungsweise ein schwach wechselwirkendes

Gas von Rydberg-Atomen gezeigt.

In dieser Arbeit wird zum direkten Beweis der kohärenten Anregung ein anderer Weg beschrieben. In dem Forschungsgebiet der magnetischen Kernspinresonanz ist das Problem einer inhomogenen Rabi-Frequenz schon seit langem bekannt, da beispielsweise verschiedene Kerne in einem komplexen Molekül verschiedene Umgebungen haben und damit verschiedene Wechselwirkungen ausgesetzt sind. Die von uns adaptierte Sequenz um das Problem der inhomogenen Rabi-Frequenz zu umgehen ist die so genannte 'Rotationsechosequenz' [Sol59]. In dieser Sequenz wird das Vorzeichen der Anregung nach einer Zeit $\tau_\mathrm{p} \leq t$, wobei τ die Gesamtpulsdauer ist, invertiert. Die Anregung der Atome in den Rydberg-Zustand wird durch die Rabi-Frequenz Ω_0 beschrieben. Durch eine Phasenumkehr des Anregungslichtes um 180 ° kann also die Anregung von Ω_0 auf $-\Omega_0$ umgekehrt werden.

In einem System in dem es keine Dekohärenz oder keine Dephasierung gibt würden in der Rotationsechosequenz für eine Zeit τ_p Atome vom Grundzustand in den Rydberg-Zustand angeregt und für die restliche Zeit $\tau - \tau_\mathrm{p}$ wieder abgeregt. Nach einer Zeit $2\tau_\mathrm{p}$ befänden sich damit alle Atome wieder im Grundzustand.

Wie oben bereits geschildert handelt es sich im Fall der Rydberg-Anregung um ein stark wechselwirkendes System, dessen Anregungsdynamik eine starke Blockade zeigt. Die starke Wechselwirkung führt zur Bildung der kollektiven Zustände, oder Superatomen, die als effektive Zweiniveauatome beschrieben werden können. Die Wechselwirkung zwischen den Superatomen führt zu einer Dephasierung, das heißt die Phasenbeziehung der Rabi-Oszillationen der einzelnen Superatome wird abhängig von der Position des Superatoms in der atomaren Wolke gestört. Eine Phasenumkehr des Anregungslasers kann nun nicht mehr alle Rydberg-Atome in den Grundzustand zurückbringen. Ein Maß für die Dephasierung ist die Sichtbarkeit des Echosignals, die definiert ist als $V = (N_\mathrm{R}(0) - N_\mathrm{R}(\tau/2))/(N_\mathrm{R}(0) + N_\mathrm{R}(\tau/2))$, wobei $N_\mathrm{R}(t)$ die Anzahl der Rydberg-Atome zum Zeitpunkt t ist.

Um die Dephasierung des Rydberg-Systems zu untersuchen wurde die Sichtbarkeit des Rotationsechosignals in Abhängigkeit von der Pulsdauer und der Grundzustanddichte untersucht. In einem ersten Experiment wurde gezeigt, dass die Rydberg-Anregung trotz der kurzen Anregungszeiten von nur einigen hundert Nanosekunden stark blockiert ist. In Referenz [Rai08a] ist diese Messung und die erste systematische Untersuchung der Kohärenzeigenschaften von Rydberg-Atomen mit Hilfe der Rotationsechomethode für magnetisch gefangene Atome gezeigt.

Des Weiteren wurde die Dephasierung des Systems für Atome, die in einer Dipolfalle gefangen sind, untersucht. Der stärkere radiale Einschluss der Atomwolke in der Dipolfalle sollte zu einer Reduktion der Anzahl der nächsten

Nachbarn und damit effektiv zu einer kleineren Dephasierung durch die Wechselwirkung zwischen den Superatomen führen.

Eine andere Möglichkeit die Dephasierung des Rydberg-Systems zu untersuchen bietet die elektromagnetisch induzierte Transparenz [Har90, Fle05]. Dabei handelt es sich um einen Effekt der durch die kohärente Kopplung von zwei Zuständen in einem Dreiniveausystem beobachtet werden kann. Zwei Laser koppeln dazu zwei langlebige Zustände an einen kurzlebigen Zustand. Die Intensität der Laser ist so zu wählen, dass die resultierende Rabi-Frequenz des einen Lasers ('Prüflaser') viel kleiner ist als die Linienbreite des kurzlebigen Zustandes. Die Intensität des anderen Lasers ('Kopplungslaser') kann vergleichbar mit der Linienbreite werden. Durch diese Kopplung entsteht eine destruktive Fano-Interferenz der Anregungspfade in den kurzlebigen Zwischenzustand [Fan61], wodurch dieser nicht besetzt wird. Daraus resultiert eine kohärente Überlagerung zwischen den beiden langlebigen Zuständen ohne Beimischung des mittleren Zustandes.

Angenommen der Prüflaser ist resonant mit dem Übergang vom Grund- zum mittleren Zustand, so wird dieser absorbiert, wenn der Kopplungslaser nicht vorhanden oder nicht resonant ist. Bringt man den Kopplungslaser in Resonanz mit dem Übergang vom mittleren in das obere angeregte Niveau verhindert die kohärente Überlagerung ohne Beimischung des mittleren Zustandes eine Absorption auf dem unteren Übergang: Das System wird für den Prüflaser transparent. Das auftretende Fenster in dem das System ohne Wechselwirkung vollständig transparent wird kann wesentlich kleiner als die natürliche Linienbreite des unteren Übergangs sein. Dessen Nachweis ist ein direkter Beweis für die Existenz des kohärenten Überlagerungszustandes.

Jede Art von Dekohärenz und Dephasierung stört den Aufbau des kohärenten Übleragerungzustandes, wodurch die Transparenz auf Resonanz verringert wird. Dies ermöglicht wieder die gezielte Untersuchung der Dephasierung im Rydberg-System in Abhängigkeit von der Laserleistung, also der Rabi-Frequenz Ω_0 und der atomare Grundzustandsdichte. Der untere Zustand des Dreiniveausystems ist in den Experimenten, die in dieser Arbeit diskutiert werden, durch den $5S_{1/2}$-Grundzustand gegeben. Der mittlere Zustand ist der $5P_{3/2}$-Zustand, der über den schwachen Prüflaser mit dem Grundzustand gekoppelt ist. Als oberer Zustand wird der $43S_{1/2}$-Rydberg-Zustand mit dem Kopplungslaser an den $5P_{3/2}$-Zustand gekoppelt. Die Lebensdauern des Grund- und Rydberg-Zustandes sind im Vergleich zu der Lebensdauer des $5P_{3/2}$-Zustandes sehr lang, womit die Grundvoraussetzungen für die Beobachtung van elektromagnetisch induzierter Transparenz gegeben ist.

Um die Messungen der Abhängigkeit der Dephasierung von der atomaren Grundzustandsdichte und der Laserleistung, also der Rabi-Frequenz Ω_0, durchzuführen wird der die Atomzahl mit Hilfe einer Absorptionsabbildung gemes-

sen. Bei diesem Abbildungsverfahren, das standardmäßig eingesetzt wird um die Atomzahl im Grundzustand in Experimenten mit ultrakalten Atomen zu bestimmen, wird ein mit dem $5S_{1/2}$ nach $5P_{3/2}$-Zustand resonantes Licht auf die Atomwolke geschienen und danach von einer Kamera detektiert. Da die Atomwolke das Licht absorbiert entsteht an der Stelle der Atome ein Schatten, der Auskunft über die Dichteverteilung gibt.

Strahlt man nun zusätzlich noch den Kopplungslaser auf der $5P_{3/2}$ nach $43S_{1/2}$-Resonanz ein, so verringert sich die Absorption auf Grund der elektromagnetisch induzierter Transparenz und der Schattenwurf auf der Kamera verschwindet. Die gemessene Atomzahl ist damit direkt ein Maß für die aufgebaute Kohärenz zwischen dem Grund- und dem Rydberg-Zustand. Eine Störung dieser Kohärenz durch eine Dekohärenz oder einer Dephasierung kann direkt als eine Zunahme der gemessenen Atomzahl beobachtet werden.

Über die Beobachtung von elektromagnetisch induzierter Transparenz in einem Rydberg-System wurde bereits in Referenz [Moh07] berichtet. Die dort gezeigten Experimente wurde in einer Gaszelle bei Raumtemperatur durchgeführt. Die in Referenz [Wea08] gezeigten Experimente wurden mit Atomen, die in einer magneto-optischen Falle gefangen waren, durchgeführt.

Die in dieser Arbeit gezeigten Experimente zur elektromagnetisch induzierten Transparenz werden mit Atomwolken, die Temperaturen im Bereich von einigen Mikro-Kelvin besitzen durchgeführt. Die Temperaturen sind damit deutlich niedriger als in allen vorangegangenen Experimenten zur elektromagnetisch induzierter Transparenz in einem Rydberg-System. Zur Präparation der Experimente wurden die magnetisch gefangenen Atome in eine optische Dipolfalle umgeladen, da es nur so möglich ist ein homogenes Magnetfeld über die Atomwolke anzulegen und so Sorge zu tragen, dass alle Atome resonant mit den Anregungslasern sind. Um die atomare Dichte so weit zu reduzieren, dass elektromagnetisch induzierte Transparenz zu beobachten war, wurden die Experimente in einer frei expandierenden Atomwolke kurz nach dem Abschalten der Dipolfalle durchgeführt. Trotzdem waren die atomaren Dichten etwa um vier Größenordnungen höher als in die, die für die in Referenz [Wea08] gezeigten Experimente genutzt wurde. Die mit den hohen Dichten verbundene Wechselwirkung zwischen den Rydberg-Atomen und die daraus resultierende Dephasierung konnte deutlich anhand der Merkmale der elektromagnetisch induzierter Transparenz nachgewiesen und vermessen werden.

Part I.

Introduction

The research field of ultracold Rydberg gases has attracted the interest of scientists all over the world in the recent years. The combination of the relatively well known physics of Rydberg atoms, which were discovered 120 years ago, with the relatively young research field of ultracold atomic gases leads to completely new perspectives. Answers to fundamental questions of the interaction between particles might be found as well as the development of completely new devices for quantum information processing.

This introduction covers very briefly the main goals and the motivation of the experiments with ultracold Rydberg atoms as well as the basic ideas of the theoretical description of this system. It also aims at giving a short historical overview about the development of this rapidly growing field of research.

Ultracold atoms

The idea of cooling atoms to the microKelvin regime is simply triggered by the interest in removing the motional degrees of freedom from the system to study the underlying physics of the interaction between the atoms. Removing the thermal energy from the atomic sample and increasing its density would lead to a description of the dynamics that is governed by the interactions of the atoms and their environment, e.g. other atoms.

The first step in nearly every experiment dealing with ultracold atoms is the cooling of atoms using laser cooling techniques. The invention of the techniques for laser cooling and trapping of atoms in magneto-optical traps has been awarded with the Nobel Prize in 1997 for S. Chu, C. Cohen-Tannoudji and W. D. Philips [Chu98, CT98, Phi98].

Further techniques for trapping and confining the atoms have been developed over the years. Using magnetic traps or optical dipole traps it is possible to achieve high densities at ultracold temperatures. For a bosonic sample of atoms this leads to the creation of Bose-Einstein condensates, originally proposed by S. N. Bose and A. Einstein in 1924 [Bos24, Ein24, Ein25], and for fermions to degenerate gases well below the Fermi temperature [DeM98]. In the same year L.-V. de Broglie intensively investigated the quantum nature of matter waves [dB24]. The crossing of the border to the quantum degenerate regime of Bose-Einstein condensation and the fundamental studies of its properties was awarded with the Nobel Prize in 2001 for E. A. Cornell, C. E. Wieman and W. Ketterle [Cor02, Ket02].

Having now the ability of removing any perturbing effect of the environment one can focus on the interaction of the atoms with each other. Usually ultracold atoms interact with each other via the isotropic short range contact interaction, where short means a distance on the order of the effective range of the s-wave scattering length, which is for rubidium on the order of

100 in units of the Bohr radius. However, the production of ultracold gases of chromium atoms and heteronuclear molecules led to the investigation of long range dipole-dipole interactions, which have an anisotropic character, i.e. the interaction depends on the alignment of the dipoles with respect to each other [Stu05]. The alignment of the dipoles can be adjusted by applying an external magnetic field or by adjusting the geometry of the trap resulting in an adjustability of the interaction between the atoms [Koc08].

While chromium atoms have the advantage of relatively large magnetic dipole moments, alkali atoms, which are of particular interest in ultracold atoms physics due to their simple level structure, can nevertheless experience strong dipole-dipole interaction. A proposal for using light to induce an anisotropic interaction in alkali atoms is given in reference [Löw05] using light induced dipoles and in reference [O'D00] using an attractive $1/r$ potential also induced by a light field.

Another avenue for the creation of large dipole-dipole interactions in alkali atoms is discovered using the admixture of electrically polarised Rydberg states [San00]. The investigation of the effects due to the interaction between Rydberg atoms or between Rydberg atoms and ground state atoms is the key point of the research field of ultracold Rydberg gases.

Rydberg atoms

Systematic research on the field of flourescence spectroscopy started with the discovery by Isaac Newton in 1666 that white light is a superposition of all colours. It was he who invented the name 'spectrum' for the splitting up of light into its frequency components. After more than one hundred years without any major achievements in spectroscopy this field of research intensively came back to the focus of scientists. Starting in 1802 with the discovery of black lines in the solar spectrum by William Hyde Wollaston. Joseph von Fraunhofer independently investigated the same phenomena and recorded several hundred of these spectral lines in 1814 using his invention of the diffraction grating. However, nobody found the reason for the appearance of the black lines prior to the work of Robert Wilhelm Bunsen and Gustav Robert Kirchhoff in 1859. Their spectral analysis led not only to the precise assignment of the spectral lines to specific elements in the periodic table, but also made it possible to find two new alkali metals, namely Caesium and Rubidium. Finally, a complete understanding of the appearance of the element specific lines were given with the upcoming theory of quantum mechanics in the years after Plancks seminal talk in 1900 [Pla01].

The swedish physicist Johannes Robert Rydberg was the first to intensively investigate the spectral properties of highly excited atoms in 1888. These

atoms, nowadays called Rydberg atoms, have at least one electron excited to a high principal quantum number n. The meaning of n became clear only after Niels Bohr presented his model of the hydrogen atom in 1913, connecting the principal quantum number to the energetic state of the atom and by this to the frequency of the emitted light.

Rydberg atoms can be described to some extent in the classical atom picture of electrons orbiting the core, in which case the principal quantum number is a measure of the size of the atom. In this sense Rydberg atoms can have a size on the order of micrometer or even larger [Mes08]. Due to the large distance of the electron from the core, Rydberg atoms are very sensitive to electric fields and interactions with neighbouring Rydberg atoms. Many of the properties, such as the polarisability and the strength of the interaction, are highly dependent on the principal quantum number and, thus, can be tuned by choosing an appropriate principal quantum number. The tunability of the strength of interaction and the manipulation of their dipolar character using electric fields make Rydberg atoms particularly interesting for the research field of quantum information processing.

The investigation of Rydberg atoms were limited in the beginning to plasmas and to stellar environments due to the high excitation energy needed for their creation. The invention of laser light sources in 1960 made it possible to selectively excite atoms into Rydberg states. For some decades the research with Rydberg atoms took only place in room temperature vapour cells and atom beams [Har77, Dal83]. In these experiments the observable linewidth of the Rydberg spectra was limited due to the Doppler or transient time broadening of the atoms moving with room temperature velocities in the cell or due to a transient time broadening in the atomic beam. Nevertheless a spectral line perturbation due to the van der Waals interaction between Rydberg atoms is shown in a atomic beam experiment [Rai81]. A sample of ultracold Rydberg atoms not only increases the interaction time and removes the Doppler broadening, but also increases the density of Rydberg atoms and, thus, their interaction with respect to each other. Only this increase in density, using the setup shown in this thesis, made it possible to observe of the blockade of Rydberg excitation due to the interaction and the resulting collective behaviour of the atomic sample as introduced in the following sections.

In order to prepare a sample of ultracold Rydberg gases only two approaches have been realised by now. A recent method uses the high sensitivity of Rydberg atoms on electric field due to the large polarisability. Applying an inhomogeneous electric field over a beam of Rydberg atoms leads to a deceleration [Vli06]. The principle of an electrostatic trap for Rydberg atoms in two dimensions is shown in [Vli07].

The approach used for the experiments in this thesis uses a sample of ul-

tracold atoms subsequently excited into Rydberg states. This method has the advantage that the time consuming part of the experiment, namely the preparation of the ultracold atomic sample, is not limited by the lifetime of the Rydberg atoms. The accessible range of atomic densities from $10^{14}\,\mathrm{m}^{-3}$ in a magneto-optical trap to $10^{20}\,\mathrm{m}^{-3}$ in a Bose-Einstein condensate trapped in either a magnetic or dipole trap is also a major advantage of this experimental scheme. The density in the magnetic or dipole trap can be varied over a large range using well known techniques from the research field of ultracold atomic physics.

Such high densities are achieved in usual cold atom experiments by cooling the atomic sample to temperature on the order of microKelvin. At these low temperatures the atomic motion can be neglected on the timescale of the experiments, that is much shorter than the lifetime of the Rydberg state. This state of matter is usually referred to as a frozen Rydberg gas [And98, Mou98].

Although collisions due to the movement of the atoms can be neglected on the timescale of the experiments an attractive interaction between the Rydberg atoms could still lead to collisions and ionisation even on the short timescale [Li05, Knu06]. The dynamics of the resulting ultracold plasma has been investigated, e.g. in the references [Rob00, Kil07].

Collectivity

Strong interactions between atoms lead also to strong correlations. Atoms in the ground state interact via s-wave scattering. Hence, the length scale of this interaction a is on the order of the interparticle distance $r \propto n_\mathrm{g}^{-1/3}$, where n_g is the atomic density. The s-wave scattering length a can be increased by means of Feshbach resonances. The strong correlation of ground state atoms in a fermionic system has been investigated in reference [Chi04] in the BEC-BCS crossover regime. The coherence of this strongly interacting system has been observed by the investigation of the superfluid behaviour of a strongly interacting Fermi gas [Zwi05].

Strongly correlated bosonic systems with ground state atoms have been realised by the production of a Mott insulator state in an optical lattice, where the interaction between the atoms are tailored by the strength of the trapping potential [Gre02]. The previously mentioned magnetic dipole-dipole interaction in ultracold chromium atoms could also lead to strongly correlated states.

Excited states can also be correlated by strong interactions, leading to collective states and blockade phenomena. The blockade of the excitation into a Rydberg state is shown for the van der Waals interaction and for dipolar interactions between Rydberg atoms [Sin04b, Ton04, Cub05b, Vog06, Hei07]. For reasonably strong interactions the excitation of a second atom into a Rydberg

state is blocked in a certain volume around a Rydberg atom.

The 'blockade radius' r_b of this volume defines a characteristic length scale for the interaction, analogue to the s-wave scattering length a. The blockade of the excitation into the Rydberg state can be understood in terms of a energy shift of the Rydberg state of the second atom in the vicinity of the already excited Rydberg atom.

An excitation into the Rydberg state is only possible if the shift of the state is smaller than the power broadening due to the Rabi frequency Ω_0 of the coupling laser. The blockade radius reads $r_\mathrm{b} \propto \sqrt[6]{|C_6|/\hbar\Omega_0}$ in the case of van der Waals interaction $V_\mathrm{vdW} = -C_6/r^6$. This length scale is on the order of 5 µm for the $43\mathrm{S}_{1/2}$ state and exceeds the interatomic distance between ground state atoms in experiments with ultracold atomic samples by orders of magnitudes. Hence, one blockade sphere may contain thousands of ground state atoms.

The excitation into the Rydberg state is then shared by thousands of ground state atoms: A collective state of the participating atoms is formed. The appearance of a collective state, which can be found in many mesoscopic systems [Rai89, Phi01, Col07], manifests itself by an excitation dynamics which is sped up by a factor $\sqrt{N}$ resulting from the normalisation of the collective state with N members. Hence, the system oscillates with the collective Rabi frequency $\sqrt{N}\Omega_0$ between the ground state and the one Rydberg state. The formation of a collective state in a strongly interacting Rydberg gas is shown in references [Hei07, Hei08a] using the experimental setup shown in this thesis.

Collective states are of particular interest for the research field of quantum information processing since such a state is an extremely robust realisation of a highly entangled W state [Dür00, Sto03]. The robustness results from the large number of participants: If one atom is removed from the collective state the remaining $N-1$ participants are left unaffected and the information is preserved. Due to its similarity to a two-level atom the collective state is referred to as a 'superatom' [Vul06]. Superatoms can be used as a realisation of a qbit for the storage of quantum information. The information is stored in two long-lived ground states, where the interaction between the Rydberg atoms provide the nonlinearity needed for any gate operation. Experimental schemes that make use of the dipole blockade are proposed in the references [Jak00, Luk01].

Another crucial ingredient for the realisation of a quantum gate using Rydberg states is the coherent excitation into the excited state. In the recent years three approaches have successfully demonstrated the coherent excitation into Rydberg states. In the case of non interacting Rydberg atoms a STIRAP (stimulated Raman adiabatic passage) sequence is used in reference [Cub05a] for the excitation of atoms from a magneto-optical trap. The coherence of the Rydberg excitation is also been shown in room temperature vapour cells

in reference [Moh07] using an EIT (electromagnetically induced transparency) excitation scheme. A direct proof of the coherence is shown by directly observing Rabi oscillations between the ground and Rydberg state at very low densities [RL08] or even by the observation of single atoms [Joh08]. Finally, the coherent excitation of a strongly interacting Rydberg gas is investigated in reference [Hei07] and as a part of this thesis and the resulting publication [Rai08a].

Universal scaling

Universal scaling laws are a very powerful tool as they can be used to predict the behaviour of a system without the exact knowledge of its microscopic composition. Universal scaling laws can be found everywhere in nature: May it be the prediction for the metabolic rate of completely different life forms in reference [Wes04] or the investigation of the normalised density as a function of the normalised temperature of many different atoms and molecules in reference [Gug45].

In the case of superatoms the exact description of the atomic state would require the knowledge of the state of all N members of the superatom. Considering the superatom as an effective two-level atom a Hilbert space of the size 2^N is needed to describe the collective state exactly. Since this is neither theoretically nor experimentally possible it is useful to have simple scaling laws to hand that describe the dynamics of the complete ensemble and draw conclusions from the collective dynamics to its members.

A proof for the coherent collective excitation into the Rydberg state was given in the references [Hei07, Hei08a] by observing the scaling behaviour of the ensemble as a function of the atomic density of ground state atoms and the Rabi frequency Ω_0. The third possible scaling with the principal quantum number, namely the van der Waals coefficient C_6, was kept constant in these experiments. The direct observation of coherent dynamics via Rabi oscillations is impossible in our experiment because we excite many superatoms at once and the inhomogeneous density distribution results in an inhomogeneous distributed $\sqrt{N}$ factor. The population of every of these superatoms oscillate with its own collective Rabi frequency, $\sqrt{N}\Omega_0$, between the ground state and the Rydberg state. This leads to a superposition of many different oscillation smearing out the individual Rabi oscillation of one superatom.

Universal scaling aims to predict such scaling laws for all systems that fall into the same universality class [Fis98]. A universality class is formed by systems that are governed by the same fundamental process. The underlying process in the case of the driven Rydberg system is a second order quantum phase transition, that is theoretically predicted in reference [Wei08]. The phase

transition happens between the phase where all atoms are in the ground state and the phase where the maximal number atoms are excited to the Rydberg state. In the picture of the superatom the maximal number of excited Rydberg atoms corresponds to the number of superatoms that fill the volume of the atomic sample as densly as possible, i.e. dense sphere packing. The dense sphere packing of the superatoms can be described in the case of van der Waals interaction in terms of a face centred cubic crystal.

A general prediction of statistical thermodynamics is that one can find a universal scaling behaviour of the characteristic variables describing the system in the vicinity of a second order phase transition. Here, the characteristic variable is the Rydberg fraction f, which is the number of Rydberg atoms divided by the number of ground state atoms. This Rydberg fraction is expected to depend on a dimensionless parameter α with a universal scaling law. The parameter $\alpha = \mathcal{V}_\mathrm{e}/\mathcal{V}_\mathrm{i}$ compares the excitation energy $\mathcal{V}_\mathrm{e}$ driving the system with the interaction energy $\mathcal{V}_\mathrm{i}$ between the Rydberg atoms. Hence, a universal scaling law of the form $f \sim \alpha^\nu$ is expected to be found in the critical region around the second order phase transition. The universal exponent depends only on the kind of interaction, i.e. whether it is van der Waals or dipole-dipole interaction, and the dimensionality of the system. The universality class is then given for all systems that interact with the same interaction, or to be more precise with the same spatial dependence of the interaction, and are confined in the same dimension.

The dimensionality of the density distribution of ground state atoms can be tailored in the presented setup in a wide range using a magnetic trap or optical dipole potentials. Furthermore, different Rydberg states can be excited by using the large tunability of the excitation laser, which makes it possible to change the interaction from van der Waals to resonant dipole-dipole interaction using electric fields. The measurements of the universal scaling behaviour shown in this thesis will present data taken for a van der Waals interacting sample of ultracold Rydberg atoms trapped either in a magnetic trap or in an optical dipole trap.

Coherence properties

The proposals in the references [Jak00, Luk01] dealing with Rydberg atoms for the purpose of building a quantum gate or processing quantum information assume that the excitation into the Rydberg state is coherent. Furthermore the atomic sample must stay coherent with respect to the excitation laser in order to read out the information after the gate operation.

Due to the interaction between the Rydberg atoms or the interaction between Rydberg atoms and their environment sources of decoherence during

the gate operation could disturb the measurement. Furthermore, a dephasing of the Rydberg state with respect to the ground state would also lead to a disturbance of the result if the dephasing cannot be canceled out by the choice of an appropriate experimental sequence.

As already mentioned above the coherent excitation into the Rydberg state is successfully demonstrated in many experimental schemes. The timescale on which the information is preserved, however, needs to be investigated. The experimental setup presented in this thesis eliminates nearly all sources of decoherence, e.g. collisions between Rydberg atoms and other atoms and interactions with walls at room temperature or perturbing electric fields due to randomly produced ions applying uncontrolled electric fields over the atomic sample.

However, two sources of dephasing cannot be removed. On the one hand the inhomogeneous density distribution in our experiment leads to an inhomogeneous distribution of the collective Rabi frequency $\sqrt{N}\Omega_0$, i.e. the Rabi frequency depends on the spatial position of the superatom in the atomic sample. Using adequate experimental techniques adapted from the research field of nuclear magnetic resonance this dephasing effect can be removed allowing an investigation of the second source of dephasing: The interaction between the superatoms. The exact interaction between the superatoms, assuming that the model is correct, is up to now unknown and under theoretical and experimental investigation. The exact knowledge of this interaction is a crucial ingredient on the way of realising the first quantum gate operations with neutral atoms.

This thesis

The thesis at hand aims to give two examples of the previously discussed fields of research: The investigation of the universal scaling of the Rydberg excitation and the characterisation of the coherence properties due to the interaction between Rydberg atoms.

The thesis is organised in three major parts. Part II briefly introduces basic concepts for the theoretical description of the Rydberg system. This includes the description of the Rydberg atom as a two-level atom and the interaction between the Rydberg atoms leading to the formation of collective states as well as an introduction to the basic concept of the universal scaling. Furthermore, the basic physics of a three-level atom is introduced to accurately describe the observed effects of electromagnetically induced transparency.

Part III introduces the experimental setup used for this investigations. The setup is already described in some extend in the references [Kro04, Löw06, But07, Hei07]. A magnetic trap is used for the cooling and trapping to temper-

atures near or below the critical temperature of the Bose-Einstein condensate phase transition. The setup is specifically designed to conduct experiments with Rydberg atoms in the magnetic trap or in an optical trap with an confinement in up to three dimensions. Eight capacitor plates, which are included in the ultrahigh vacuum chamber, allow the application of nearly arbitrary electric fields over the atomic sample. Furthermore, two charged particle detectors in the chamber can be used for the simultaneous detection of ionised Rydberg atoms or their accompanied electrons.

Special attention is drawn to the linewidth of the laser system for the Rydberg excitation. The stability has to be suffcient to spectroscopically resolve the excitation lines of the Rydberg state and exclude any perturbing decoherence process due to a drift of the laser frequency. Hence, the lasers must be stable during one experiment, i.e. on the hundred microsecond timescale, as well as on the long, i.e. minute timescale, between the experiments.

Part IV shows the experimental results on the observation of the universal scaling of the driven Rydberg system as well as the results on the measurement of the coherence properties.

The universal scaling is investigated by measuring the initial increase and the saturation value of the excitation dynamics into the Rydberg state for a large range of atomic densities and Rabi frequencies, i.e. laser powers. The presented measurements are done with magnetically trapped atoms and with atoms trapped in an optical dipole trap. The two measurements are evaluated particularly with regard to the dimensionality of the atomic density distribution, that is reduced by the stronger confinement of the optical dipole trap with respect to the density distribution in the magnetic trap.

The investigation of the coherence properties include two different methods. The first method uses a technique known from the research field of nuclear magnetic resonance: The rotary echo sequence [Sol59]. This sequence was invented to overcome problems due to inhomogeneous Rabi frequencies, a situation very similar to that in experiments with ultracold Rydberg atoms at high atomic densities. The Rabi frequency in the Rydberg system is inhomogeneous due to the inhomogeneous atomic density distribution leading to a spatial variation of the collective Rabi frequency $\sqrt{N}\Omega_0$. The rotary echo sequence is furthermore technically relatively simple to implement into the present setup by only switching the phase of one excitation laser by $180\,^\circ$. This results in a reversion of the sign of the excitation laser field from Ω_0 to $-\Omega_0$. Removing the effect of the inhomogeneous Rabi frequency from the measurements leads to the ability to solely investigate the dephasing effects due to the interaction between the Rydberg atoms.

The second method for the investigation of the coherence properties uses an experimental scheme called electromagnetically induced transparency. As the

name already implies, an electromagnetic field renders a medium transparent under certain conditions. By using electromagnetically induced transparency it is possible to coherently excite the atoms from the ground state into the Rydberg state. The dephasing of the Rydberg state affects this coherent excitation and manifests itself in a frequency broadening of the EIT feature and a decreasing transparency of the atomic sample.

Part II.

Theoretical pillars

1. Atom light interaction

Understanding the interaction between atoms and light is crucial for dealing with ultracold atoms. The simplest model is that of one atom with two states interacting with a light field of distinct frequency. Although this two-level atom is artificial it gives insight into the principles of atom light interaction, such as cooling and trapping. Furthermore, assuming good control of the laser frequency, the two-level atom can be used to model alkali atoms to some extent. The first sections will introduce briefly the physics of the two-level atom including the description using the density matrix formalism and the useful picture of the Bloch vector. The sections 1.6 and 1.7 deal with the physics of a three-level atom. The three-level atom model assumes one atom with three non-degenerate energy levels and two light modes. In this work this system is of interest to explain electromagnetically induced transparency.
Section 1.8 presents under which circumstances the description of a three-level atom can be reduced to the description of an effective two-level atom, which is useful in most of the experiments presented in part IV.

1.1. Two-level atom

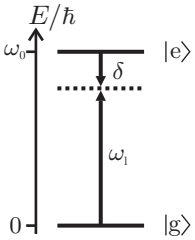

Figure 1.1.: A two-level atom with ground state $|g\rangle$ and an exited state $|e\rangle$ with an energy difference of $\hbar\omega_0$. The laser coupling the states has a frequency of ω_l and a detuning $\delta = \omega_l - \omega_0$ from resonance.

The interaction between an atom with two levels, a ground state $|g\rangle$ with zero energy and an excited state $|e\rangle$ with energy $\hbar\omega_0$, and one light mode with frequency ω_l is given by the Hamiltonian

$$\mathcal{H} = \mathcal{H}_a + \mathcal{H}_l + \mathcal{H}_i \,. \tag{1.1}$$

The three contributions are [Met99]

$$\mathcal{H}_\mathrm{a} = \frac{\boldsymbol{p}^2}{2m} + \hbar\omega_0 \left|\mathrm{e}\right\rangle \left\langle\mathrm{e}\right| , \tag{1.2}$$

$$\mathcal{H}_\mathrm{l} = \hbar\omega_\mathrm{l}(a^\dagger a + 1/2) , \tag{1.3}$$

$$\mathcal{H}_\mathrm{i}(\boldsymbol{r}, t) = -\boldsymbol{d} \cdot \boldsymbol{E}(\boldsymbol{r}, t) . \tag{1.4}$$

In the case of ultracold atoms one can neglect the kinetic energy in equation (1.2). The eigenvalues of H_l are $E_\mathcal{N} = \hbar\omega_\mathrm{l}(\mathcal{N} + 1/2)$, where $a^\dagger$ and a are the creation and annihilation operator for photons in the light mode with frequency ω_l, respectively. Thus, this term accounts for the number $\mathcal{N}$ of photons in the light mode with frequency ω_l. For a start, this quantisation of the light field will be neglected. Taking the quantisation of the light field into account yields to the dressed atom picture discussed in section 1.4.
Finally, the interaction between the atom and the light field is given by the Hamiltonian H_i in equation (1.4), using the dipole approximation, which is valid for wavelengths much larger than the Bohr radius. In this case the dipole $\boldsymbol{d} = e_0\boldsymbol{r}$ interacts with the electric field travelling along the z-direction $\boldsymbol{\mathcal{E}}(\boldsymbol{r}, t) = \mathcal{E}_0\boldsymbol{\epsilon}\cos(kz - \omega_\mathrm{l}t)$ with a polarisation along $\boldsymbol{\epsilon}$. By introducing the Rabi frequency

$$\Omega \equiv -\frac{e_0\mathcal{E}_0}{\hbar} \left\langle\mathrm{e}\right| \boldsymbol{r} \left|\mathrm{g}\right\rangle \tag{1.5}$$

the interaction Hamiltonian $\mathcal{H}_\mathrm{i}$ reads in the eigensystem of $\mathcal{H}_\mathrm{a}$

$$\mathcal{H}_\mathrm{i} = \frac{1}{2}\hbar\Omega \left(\mathrm{e}^{-i\omega_\mathrm{l}t} + \mathrm{e}^{i\omega_\mathrm{l}t}\right)\left(\left|\mathrm{e}\right\rangle \left\langle\mathrm{g}\right| + \left|\mathrm{g}\right\rangle \left\langle\mathrm{e}\right|\right) . \tag{1.6}$$

1.2. Density matrix

In general the atomic state is, e.g. due to dissipation, a statistical mixture $\{\left|\psi\right\rangle_i\}$ of different pure states $\left|\psi\right\rangle = c_\mathrm{g}(t)\left|\mathrm{g}\right\rangle + c_\mathrm{e}(t)\left|\mathrm{e}\right\rangle$. The introduction of the density matrix formalism allows to solve the Schrödinger equation for this statistical mixture with the Hamiltonian from equation (1.1) by means of matrix manipulations. Considering only pure states $\left|\psi\right\rangle$, i.e. in absence of dissipation, the density matrix is given by

$$\boldsymbol{\rho} \equiv \left|\psi\right\rangle \left\langle\psi\right| = \begin{pmatrix} \rho_\mathrm{gg} & \rho_\mathrm{ge} \\ \rho_\mathrm{eg} & \rho_\mathrm{ee} \end{pmatrix} = \begin{pmatrix} \left|c_\mathrm{g}\right|^2 & c_\mathrm{g}c_\mathrm{e}^* \\ c_\mathrm{e}c_\mathrm{g}^* & \left|c_\mathrm{e}\right|^2 \end{pmatrix} . \tag{1.7}$$

The dynamics of the density matrix is given by the Liouville equation

$$\dot{\boldsymbol{\rho}} = -\frac{i}{\hbar}\left[\mathcal{H}, \boldsymbol{\rho}\right] . \tag{1.8}$$

The dynamics of the atom that is fast with respect to the laser frequency is usually not of interest and can be separated from the slow dynamics using the rotating wave approximation. This is done by transforming $\boldsymbol{\rho}$ to a coordinate system, that rotates with the laser frequency ω_l and neglecting all terms that rotate with $\omega_0 + \omega_\mathrm{l}$ as those correspond to two-photon excitations. The transformed density matrix becomes

$$\boldsymbol{\varsigma} = \begin{pmatrix} \rho_{\mathrm{gg}} & \rho_{\mathrm{ge}}\, \mathrm{e}^{i\omega_\mathrm{l} t} \\ \rho_{\mathrm{eg}}\, \mathrm{e}^{-i\omega_\mathrm{l} t} & \rho_{\mathrm{ee}} \end{pmatrix} . \tag{1.9}$$

Introducing the detuning of the laser from the resonance $\delta = \omega_\mathrm{l} - \omega_0$ the Hamiltonian for the atom light interaction becomes

$$\mathcal{H} = \frac{\hbar}{2} \begin{pmatrix} 0 & \Omega \\ \Omega^* & -2\delta \end{pmatrix} . \tag{1.10}$$

All light modes except the laser mode with frequency ω_l are nearly unoccupied and do not cause an excitation of the atom. However, the atom is able to emit in these light modes. This can be understood as a reservoir and can be covered by a decay rate Γ, which leads to the Lindblad master equation

$$\mathcal{L}(\boldsymbol{\varsigma}) = \dot{\boldsymbol{\varsigma}} = -\frac{i}{\hbar}[\mathcal{H}, \boldsymbol{\varsigma}] + \mathcal{L}_\mathrm{d}(\boldsymbol{\varsigma}) , \tag{1.11}$$

with

$$\mathcal{L}_\mathrm{d}(\boldsymbol{\varsigma}) = \sum_k \Gamma_k \left(\mathcal{A}_k \boldsymbol{\varsigma} \mathcal{A}_k^\dagger - \frac{1}{2} \mathcal{A}_k^\dagger \mathcal{A}_k \boldsymbol{\varsigma} - \frac{1}{2} \boldsymbol{\varsigma} \mathcal{A}_k^\dagger \mathcal{A}_k \right) . \tag{1.12}$$

The $\mathcal{A}_k$ are of the form $\mathcal{A}_k = |m\rangle \langle n|$ and Γ_k is the decay rate from $|n\rangle$ to $|m\rangle$, where $k \in \{\mathrm{gg}, \mathrm{ge}, \mathrm{eg}, \mathrm{ee}\}$ for a two-level atom. Neglecting any thermal excitation and dephasing, hence $\Gamma_{\mathrm{gg}} = 0$ and $\Gamma_{\mathrm{ge}} = \Gamma_{\mathrm{eg}} = 0$, equation (1.12) becomes with $\Gamma_{\mathrm{ee}} = \Gamma$

$$\mathcal{L}_\mathrm{d}(\boldsymbol{\varsigma}) = \Gamma \begin{pmatrix} \varsigma_{\mathrm{ee}} & -\frac{1}{2}\varsigma_{\mathrm{ge}} \\ -\frac{1}{2}\varsigma_{\mathrm{eg}} & -\varsigma_{\mathrm{ee}} \end{pmatrix} . \tag{1.13}$$

The solution of the Lindblad master equation can be conveniently illustrated using the Bloch sphere introduced in the next section. The MatLab program in appendix A.3 solves equation (1.11) for a two-level atom if the parameter Ω_c of this program is set to zero.

1.3. Bloch vector

Using equations (1.13) and (1.10) in equation (1.11) one finds the Bloch equations [Sar93]

$$\begin{aligned}
\dot{\varsigma}_{gg} &= -\frac{i}{2}\Omega\left(\varsigma_{eg} - \varsigma_{ge}\right) + \Gamma\,\varsigma_{ee}\,,\\
\dot{\varsigma}_{ge} &= -\frac{i}{2}\Omega\left(\varsigma_{ee} - \varsigma_{gg}\right) - \left(i\delta + \frac{\Gamma}{2}\right)\varsigma_{ge}\,,\\
\dot{\varsigma}_{eg} &= +\frac{i}{2}\Omega\left(\varsigma_{ee} - \varsigma_{gg}\right) + \left(i\delta - \frac{\Gamma}{2}\right)\varsigma_{eg}\,,\\
\dot{\varsigma}_{ee} &= +\frac{i}{2}\Omega\left(\varsigma_{eg} - \varsigma_{ge}\right) - \Gamma\,\varsigma_{ee}\,,
\end{aligned} \tag{1.14}$$

and their steady state solutions

$$\begin{aligned}
\varsigma'_{gg} &= 1 - \varsigma'_{ee}\,,\\
\varsigma'_{ge} &= \frac{2\Omega\left(\delta + i\frac{\Gamma}{2}\right)}{4\delta^2 + \Gamma^2 + 2\Omega^2}\,,\\
\varsigma'_{eg} &= \varsigma'^{*}_{ge}\,,\\
\varsigma'_{ee} &= \frac{\Omega^2}{4\delta^2 + \Gamma^2 + 2\Omega^2}\,.
\end{aligned} \tag{1.15}$$

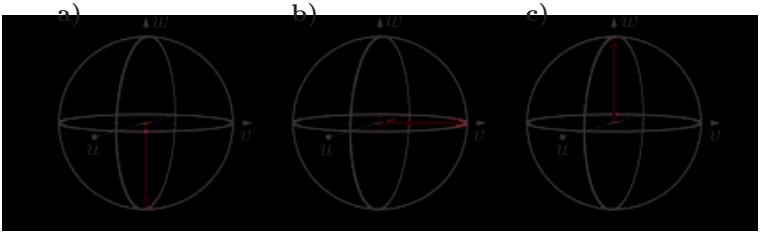

Figure 1.2.: Three examples of the representation of an atomic state as a Bloch vector in a unit sphere. The top of the Bloch sphere represents the exited state $|e\rangle$, the bottom the ground state $|g\rangle$. **a)** All atoms are in the ground state $|g\rangle$. **b)** After a $\pi/2$-pulse the atoms are in a coherent superposition between $|g\rangle$ and $|e\rangle$. **c)** All atoms are excited into $|e\rangle$ after a π-pulse.

Introducing the new variables $u = \frac{1}{2}(\varsigma_{eg} + \varsigma_{ge})$, $v = \frac{i}{2}(\varsigma_{eg} - \varsigma_{ge})$ and $w = \frac{1}{2}(\varsigma_{ee} - \varsigma_{gg})$ the Bloch equations (1.14) can be rewritten in a convenient way as

$$\dot{\boldsymbol{\beta}} = \boldsymbol{\Omega} \times \boldsymbol{\beta} - \boldsymbol{\Gamma}\,. \tag{1.16}$$

The similarity to a spinning top implies the picture of the Bloch vector $\boldsymbol{\beta} = (u, v, w)^{\mathrm{t}}$ in a unit sphere, where the bottom represents $|\mathrm{g}\rangle$ and the top $|\mathrm{e}\rangle$ (see figure 1.2). Applying a light pulse to the atom means in this picture rotating the Bloch vector around the u-axis from the bottom towards the top. The Bloch vector $\boldsymbol{\beta}$ precesses around $\boldsymbol{\Omega} = (\Omega, 0, -\delta)^{\mathrm{t}}$. In the absence of dissipation, i.e. $\boldsymbol{\Gamma} = \mathbf{0}$, the Bloch vector keeps unity length. If the decay rate Γ is finite the dissipation is included into the Bloch equations by $\boldsymbol{\Gamma} = \frac{\Gamma}{2}(u, v, 2w - 1)^{\mathrm{t}}$ and the length of $\boldsymbol{\beta}$ decreases with time. For times long compared to $1/\Gamma$ the steady state value according to equation (1.15) is reached

$$\boldsymbol{\beta}_{\mathrm{ss}} = \frac{s}{1+s} \begin{pmatrix} \frac{\delta}{\Omega} \\ \frac{\Gamma}{2\Omega} \\ -\frac{1}{2s} \end{pmatrix} , \tag{1.17}$$

with the saturation parameter

$$s = \frac{\Omega^2/2}{\delta^2 + (\Gamma/2)^2} . \tag{1.18}$$

1.4. Dressed atoms

Many effects of excitation, e.g. the Mollow triplet and electromagnetically induced transparency (see section 1.7), can be explained if the quantisation of the light field, and thus equation (1.3), is taken into account. A comprehensive description was given by J. Dalibard and C. Cohen-Tannoudji in [Dal85]. Their dressed atom approach combines the atomic bare state $|\mathrm{g}\rangle$ and $|\mathrm{e}\rangle$ with the eigenstates of the light field $|\mathcal{N}\rangle$. Figure 1.3 shows the bare energy states of the atom and the light as well as the coupled dresses states $|+, \mathcal{N}\rangle$ and $|-, \mathcal{N}\rangle$.

The new eigenstates can be found be diagonalising the Hamiltonian in equation (1.10) resulting in

$$\mathcal{H}' = -\frac{\hbar}{2} \begin{pmatrix} \delta - \Omega' & 0 \\ 0 & \delta + \Omega' \end{pmatrix} , \tag{1.19}$$

with

$$\Omega' = \sqrt{\Omega^2 + \delta^2} , \tag{1.20}$$

and

$$\begin{aligned} |+, \mathcal{N}\rangle &= \sin\frac{\vartheta}{2} |\mathrm{g}, \mathcal{N}+1\rangle + \cos\frac{\vartheta}{2} |\mathrm{e}, \mathcal{N}\rangle , \\ |-, \mathcal{N}\rangle &= \cos\frac{\vartheta}{2} |\mathrm{g}, \mathcal{N}+1\rangle - \sin\frac{\vartheta}{2} |\mathrm{e}, \mathcal{N}\rangle . \end{aligned} \tag{1.21}$$

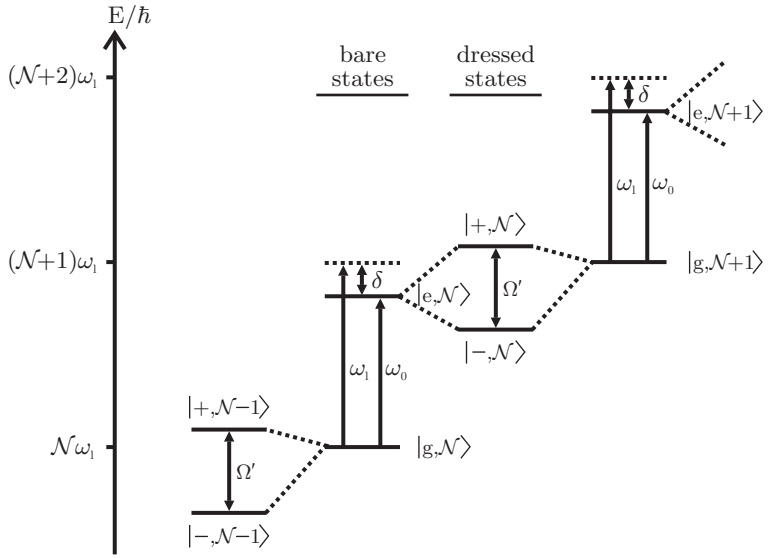

Figure 1.3.: Dressed atom picture for a two-level atom. The uncoupled basis with the atomic eigenstates $|\mathrm{g}\rangle$ and $|\mathrm{e}\rangle$ and the eigenstates of the quantised light field $|\mathcal{N}\rangle$ are coupled by the Hamiltonians H_l and H_i given by equations (1.2) and (1.3) to new eigenstates $|+,\mathcal{N}\rangle$ and $|-,\mathcal{N}\rangle$. For the sake of readability the level scheme is shifted horizontally while going from $|\mathcal{N}\rangle$ to $|\mathcal{N}+1\rangle$. The energy difference between $|\mathrm{g},\mathcal{N}\rangle$ and $|\mathrm{g},\mathcal{N}+1\rangle$ is $\hbar\omega_\mathrm{l}$.

The Stückelberg angle describes the admixture of the bare states in the dressed states

$$\vartheta = \arctan\left(-\frac{\Omega}{\delta}\right) . \tag{1.22}$$

Hence, every new eigenstate is a mixture of the old eigenstates to $\mathcal{H}_\mathrm{a}$, where the mixing is 50 % for $\delta = 0$. The new eigenstates evolve asymptotically into the old for large detunings $\delta \gg \Omega$: $|+,\mathcal{N}\rangle$ evolves into $|\mathrm{e},\mathcal{N}\rangle$ and $|-,\mathcal{N}\rangle$ evolves into $|\mathrm{g},\mathcal{N}\rangle$.

1.5. Light shift and optical dipole trap

A very important application is directly connected to the situation where $\delta \gg \Omega$, namely the trapping of atoms using the dipole force of the light field. The

light shift of the ground state is for $\delta \gg \Omega$ according to (1.19) and (1.20)

$$\Delta E_\mathrm{g} \approx \frac{\hbar\Omega^2}{4\delta}\,. \tag{1.23}$$

For red detuning, i.e. $\delta < 0$ the light shift for the ground state is negative and the atoms are attracted towards regions of high intensity. When dealing with real atoms a laser beam forming an optical dipole trap couples not only two states. Thus, the internal structure of the atom has to be taken into account and the Rabi frequency can be calculated according to [Met99, Hei08a] using

$$\begin{aligned}\Omega = \quad & (-1)^{l'+s+i-m'_f+1}\sqrt{\tfrac{2I}{c\hbar^2\epsilon_0}}\;\langle n', l'||r||n, l\rangle \\ & \times\sqrt{(2j+1)(2j'+1)(2f+1)(2f'+1)} \\ & \times \begin{Bmatrix} l' & j' & s \\ j & l & 1 \end{Bmatrix} \begin{Bmatrix} j' & f' & i \\ f & j & 1 \end{Bmatrix} \begin{pmatrix} f & 1 & f' \\ m_f & q & -m'_f \end{pmatrix}.\end{aligned} \tag{1.24}$$

The braces and the curly braces denote the Wigner 3j and 6j symbols, respectively, decomposing the atomic state from the f-basis into the uncoupled basis. The variables l, s and i denote the orbital angular momentum, the spin and the nuclear angular momentum, respectively. The prime denotes the final state. The Russell-Saunders coupling couples l and s to $j = l + s$ and the hyperfine couples j and i to the total angular momentum $f = j + i$, with m_f being the projection of f onto the quantisation axis. Furthermore, I is the intensity of the laser and $\langle n', l'||r||n, l\rangle$ is the radial part of the dipole matrix element. The radial part for a transition $|a\rangle$ to $|b\rangle$ is related to the Einstein-A coefficient $A_{ba} = \Gamma_{ba}$ by

$$\langle n', l'||r||n, l\rangle = \sqrt{\frac{3\pi c^3\varepsilon_0\hbar A_{ba}}{\omega_{ba}^3}}\,\sqrt{2l_b+1}\,. \tag{1.25}$$

The scattering rate $\Gamma_\mathrm{s} \equiv \Gamma_{ba}\varsigma'_\mathrm{ee}$ is for a large detuning $\delta_{ba} \gg (\Gamma_{ba}, \Omega)$ with equations (1.15), (1.24) and (1.25)

$$\Gamma_\mathrm{s} = \frac{3\pi c^2}{2\hbar\omega_{ba}^3}\left(\frac{\Gamma_{ba}}{\delta_{ba}}\right)^2 I\,, \tag{1.26}$$

with $\Gamma_{ba} = A_{ba}$ and $\delta_{ba} = \omega_\mathrm{l} - \omega_{ba}$. Hence, the trap potential is proportional to $1/\delta_{ba}$, while the scattering rate decreases with $1/\delta_{ba}^2$, which means that it is favourable to use high power lasers with a large detuning from the atomic transition.

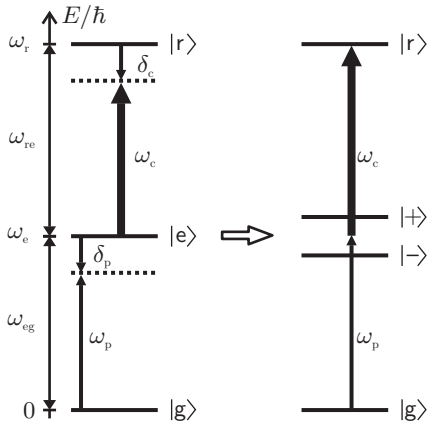

Figure 1.4.: Three-level atom. An atom with a ground state $|\mathrm{g}\rangle$ a first excited state $|\mathrm{e}\rangle$ and a second exited state $|\mathrm{r}\rangle$. The energy difference between the states $|\mathrm{g}\rangle$ and $|\mathrm{e}\rangle$ is $\hbar\omega_{\mathrm{eg}}$ and $\hbar\omega_{\mathrm{re}}$ between $|\mathrm{e}\rangle$ and $|\mathrm{r}\rangle$. The states are coupled by light with a frequency of ω_{p} ('probe laser') and ω_{c} ('coupling laser'), respectively. The frequency ω_{p} is far detuned with respect to the upper transition and ω_{c} is far detuned with respect to the lower transition. The probe laser has a detuning of $\delta_{\mathrm{p}} = \omega_{\mathrm{p}} - \omega_{\mathrm{eg}}$ and the coupling laser has a detuning of $\delta_{\mathrm{c}} = \omega_{\mathrm{c}} - \omega_{\mathrm{re}}$.

1.6. Three-level atom

The description of a three-level atom follows basically the description of a two-level atom, but the physics of the three-level atom is enriched by a number of effects, of which the electromagnetically induced transparency and Autler-Townes splitting are of special interest in this thesis and will be introduced in section 1.7. The three levels are labeled as (see figure 1.4) $|\mathrm{g}\rangle$ (ground state), $|\mathrm{e}\rangle$ (excited state) and, to cause less confusion later on, $|\mathrm{r}\rangle$ (Rydberg state).

The Hamiltonian of the three-level atom is, assuming cold atoms and the dipole approximation, similar to equation (1.1) with

$$\mathcal{H}_{\mathrm{a}} = \hbar\omega_{\mathrm{e}} |\mathrm{e}\rangle\langle\mathrm{e}| + \hbar\omega_{\mathrm{r}} |\mathrm{r}\rangle\langle\mathrm{r}| \,, \tag{1.27}$$

$$\mathcal{H}_{\mathrm{l}} = \hbar\omega_{\mathrm{p}}(a_{\mathrm{p}}^{\dagger}a_{\mathrm{p}} + 1/2) + \hbar\omega_{\mathrm{c}}(a_{\mathrm{c}}^{\dagger}a_{\mathrm{c}} + 1/2) \,, \tag{1.28}$$

$$\mathcal{H}_{\mathrm{i}} = \frac{\hbar}{2}\left(\Omega_{\mathrm{p}}\, \mathrm{e}^{-i\omega_{\mathrm{p}}t} |\mathrm{e}\rangle\langle\mathrm{g}| + \Omega_{\mathrm{c}}\, \mathrm{e}^{-i\omega_{\mathrm{c}}t} |\mathrm{r}\rangle\langle\mathrm{e}| + \mathrm{h.c.}\right) . \tag{1.29}$$

Thus, equation (1.10) becomes in the basis $|\mathrm{g}\rangle = (1,0,0)^{\mathrm{t}}$, $|\mathrm{e}\rangle = (0,1,0)^{\mathrm{t}}$ and $|\mathrm{r}\rangle = (0,0,1)^{\mathrm{t}}$

$$\mathcal{H} = \frac{\hbar}{2}\begin{pmatrix} 0 & \Omega_{\mathrm{p}} & 0 \\ \Omega_{\mathrm{p}}^{*} & -2\delta_{\mathrm{p}} & \Omega_{\mathrm{c}} \\ 0 & \Omega_{\mathrm{c}}^{*} & -2(\delta_{\mathrm{p}} + \delta_{\mathrm{c}}) \end{pmatrix} , \tag{1.30}$$

and the Liouville operator becomes according to equation (1.12)

$$\begin{aligned}
\mathcal{L}_{\mathrm{d}} = &\Gamma_{\mathrm{eg}} \begin{pmatrix} \varsigma_{\mathrm{ee}} & -\frac{1}{2}\varsigma_{\mathrm{ge}} & 0 \\ -\frac{1}{2}\varsigma_{\mathrm{eg}} & -\varsigma_{\mathrm{ee}} & -\frac{1}{2}\varsigma_{\mathrm{er}} \\ 0 & -\frac{1}{2}\varsigma_{\mathrm{re}} & 0 \end{pmatrix} \\
&+\Gamma_{\mathrm{rg}} \begin{pmatrix} \varsigma_{\mathrm{rr}} & 0 & -\frac{1}{2}\varsigma_{\mathrm{gr}} \\ 0 & 0 & -\frac{1}{2}\varsigma_{\mathrm{er}} \\ -\frac{1}{2}\varsigma_{\mathrm{rg}} & -\frac{1}{2}\varsigma_{\mathrm{re}} & -\varsigma_{\mathrm{rr}} \end{pmatrix} \\
&+\Gamma_{\mathrm{re}} \begin{pmatrix} 0 & 0 & -\frac{1}{2}\varsigma_{\mathrm{gr}} \\ 0 & \varsigma_{\mathrm{rr}} & -\frac{1}{2}\varsigma_{\mathrm{er}} \\ -\frac{1}{2}\varsigma_{\mathrm{rg}} & -\frac{1}{2}\varsigma_{\mathrm{re}} & -\varsigma_{\mathrm{rr}} \end{pmatrix} \\
&+\gamma_{\mathrm{ed}} \begin{pmatrix} 0 & -\frac{1}{2}\varsigma_{\mathrm{ge}} & 0 \\ -\frac{1}{2}\varsigma_{\mathrm{eg}} & 0 & -\frac{1}{2}\varsigma_{\mathrm{er}} \\ 0 & -\frac{1}{2}\varsigma_{\mathrm{re}} & 0 \end{pmatrix} \\
&+\gamma_{\mathrm{rd}} \begin{pmatrix} 0 & 0 & -\frac{1}{2}\varsigma_{\mathrm{gr}} \\ 0 & 0 & -\frac{1}{2}\varsigma_{\mathrm{er}} \\ -\frac{1}{2}\varsigma_{\mathrm{rg}} & -\frac{1}{2}\varsigma_{\mathrm{re}} & 0 \end{pmatrix},
\end{aligned} \tag{1.31}$$

where γ_{ed} and γ_{rd} take, according to [Fle05], additional energy conserving dephasing processes into account. These dephasing rates have no contribution to the diagonal entries of the Liouville operator and, thus, do not change the population of the state but only the coherence between the states. Phase fluctuations of the driving laser field or the interaction between Rydberg atoms are processes which could lead to such dephasing rates γ_{ed} and γ_{rd}. The effects of γ_{ed} and γ_{rd} are discussed in section 1.7 and depicted in figure 1.6.

In analogy to the two-level atom the three-level atom can be written in terms of dressed states. For a weak probe laser with frequency ω_{p} and a strong coupling laser with frequency ω_{c}, i.e. $\Omega_{\mathrm{c}} \gg \Omega_{\mathrm{p}}$, the dressed atom picture is shown in figure 1.5. Again, one sees a splitting of the new eigenstates by Ω' due the atom light interaction. This Autler-Townes splitting [Aut55] can now be detected using the probe transition (see figure 1.6 c)). A similar picture for the case $\Omega_{\mathrm{p}} \gg \Omega_{\mathrm{c}}$ can be found in [Hei08a] figure 2.4. If the Rabi frequencies of the coupling and probe laser are on the same order of magnitude the dressed atom level scheme is a combination of both pictures.

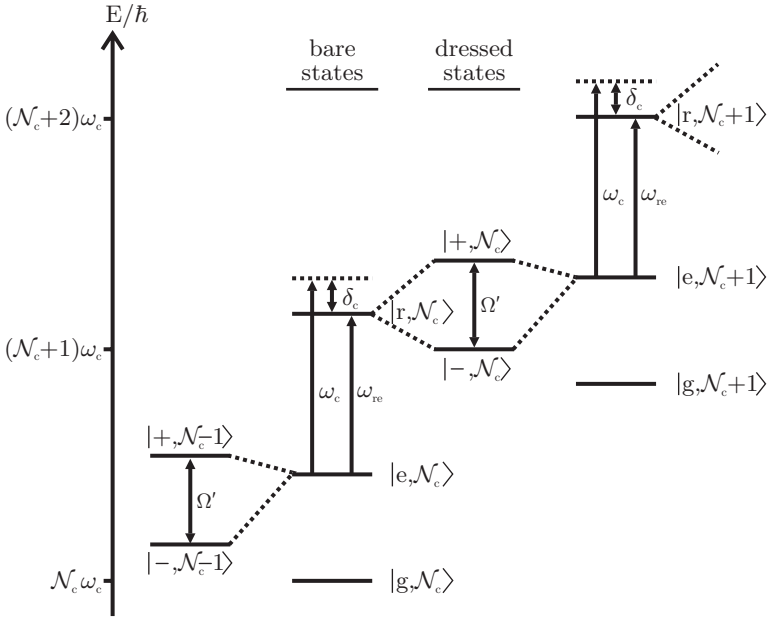

Figure 1.5.: Dressed atom picture for a three-level atom and two light modes, where $\Omega_c \gg \Omega_p$, which is the case for an EIT scheme (see section 1.7). The uncoupled basis with the atomic eigenstates $|g\rangle$, $|e\rangle$ and $|r\rangle$ and the eigenstates of the quantised light field $|\mathcal{N}_c\rangle$ with frequency ω_c are coupled by the Hamiltonians given by equations (1.27) and (1.28) to new eigenstates $|+,\mathcal{N}_c\rangle$ and $|-,\mathcal{N}_c\rangle$. For the sake of readability the level scheme is shifted horizontally while going from $|\mathcal{N}_c\rangle$ to $|\mathcal{N}_c+1\rangle$. The energy difference between $|g,\mathcal{N}_c\rangle$ and $|g,\mathcal{N}_c+1\rangle$ is $\hbar\omega_c$.

The digonalisation of equation (1.30) gives the new eigenstates for the three-level atom in terms of the atomic bare states [Fle05]

$$\begin{aligned} |+\rangle &= \sin\vartheta\,\sin\varphi\,|g\rangle + \cos\varphi\,|e\rangle + \cos\vartheta\,\sin\varphi\,|r\rangle\ , \\ |\emptyset\rangle &= \cos\vartheta\,|g\rangle - \sin\vartheta\,|r\rangle\ , \\ |-\rangle &= \sin\vartheta\,\cos\varphi\,|g\rangle - \sin\varphi\,|e\rangle + \cos\vartheta\,\cos\varphi\,|r\rangle\ . \end{aligned} \tag{1.32}$$

On two-photon resonance ($\delta = \delta_\mathrm{p} + \delta_\mathrm{c} = 0$) the Stückelberg angles are

$$\begin{aligned} \vartheta &= \arctan \frac{\Omega_\mathrm{p}}{\Omega_\mathrm{c}} , \\ \varphi &= \frac{1}{2} \arctan \frac{\sqrt{\Omega_\mathrm{p}^2 + \Omega_\mathrm{c}^2}}{\delta_\mathrm{p}} . \end{aligned} \tag{1.33}$$

Especially the case where the states $|\mathrm{g}\rangle$ and $|\mathrm{r}\rangle$ have a long lifetime compared to the state $|\mathrm{e}\rangle$ is of interest since the state $|\emptyset\rangle$ has no contribution of the radiative state $|\mathrm{e}\rangle$. Thus, if the dephasing rate $\gamma_\mathrm{rd} = 0$ and the lifetime of $|\mathrm{e}\rangle$ due to radiation short compared to those of $|\mathrm{g}\rangle$ and $|\mathrm{r}\rangle$, the system will evolve on a timescale given by Γ_eg towards the state $|\emptyset\rangle$. A laser probing between the states $|\mathrm{g}\rangle$ and $|\mathrm{e}\rangle$ hence will not be absorbed. This effect is called coherent population trapping (CPT) [Alz76, Ari76, Whi76]. If the dephasing rate $\gamma_\mathrm{rd} \neq 0$ the resulting state will not be $|\emptyset\rangle$, but some mixture of all atomic bare states and the probe laser will partially be absorbed. Additionally the time scale for the decoherence is than given by the lifetime $1/\Gamma_\mathrm{eg}$ of the intermediate state. The different situations are depicted in figure 1.6.

1.7. Electromagnetically induced transparency

Electromagnetically induced transparency (EIT) describes an effect in a three-level system, where the three levels are coherently coupled with two lasers as described in section 1.6 in the special case that one of the two lasers is weak [Har90]. Weak in this context means that the Rabi frequency Ω_p of this probe laser is small in comparison to the decay rate of the corresponding transition.

EIT was first experimentally observed by Boller *et al.* [Bol91]. As the term EIT already implies, a medium becomes transparent under certain conditions, namely if both lasers ω_p and ω_c are resonant to the transitions ω_eg and ω_re, respectively. EIT can be understood using the dressed atom scheme depicted in figure 1.5. Considering a strong coupling laser with frequency ω_c on the transition from $|\mathrm{e}\rangle$ to $|\mathrm{r}\rangle$ and a weak probe laser with frequency ω_p on the transition from $|\mathrm{g}\rangle$ to $|\mathrm{e}\rangle$, i.e. $\Omega_\mathrm{c} \gg \Omega_\mathrm{p}$, and hence $\sin\vartheta \to 0$ and $\cos\vartheta \to 1$. This leads to the new eigenstates

$$\begin{aligned} |+\rangle &= \sin\varphi\ |\mathrm{r}\rangle\ + \cos\varphi\ |\mathrm{e}\rangle\ , \\ |\emptyset\rangle &= |\mathrm{g}\rangle\ , \\ |-\rangle &= \sin\varphi\ |\mathrm{r}\rangle\ - \cos\varphi\ |\mathrm{e}\rangle\ . \end{aligned} \tag{1.34}$$

If the probe laser comes into resonance, i.e. $\delta_\mathrm{p} = 0$ the states are $|+\rangle = (|\mathrm{r}\rangle + |\mathrm{e}\rangle)/\sqrt{2}$ and $|-\rangle = (|\mathrm{r}\rangle - |\mathrm{e}\rangle)/\sqrt{2}$. The probe light couples only to the $|\mathrm{e}\rangle$ part of $|+\rangle$ and $|-\rangle$, which have opposite signs in these states. This causes an

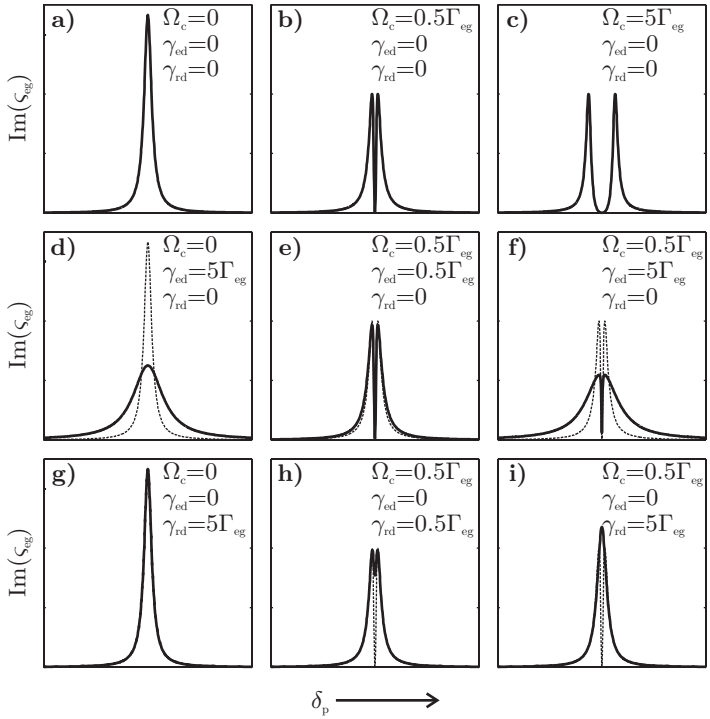

Figure 1.6.: Absorption spectra for different coupling strengths and dephasing rates. The absorption is proportional to the imaginary part of the susceptibility χ, while the real part of χ is proportional to the dispersion. The susceptibility is a function of the coherence ς_{eg}. The dashed lines in figures **d)** to **i)** indicate the absorption without dephasing rate as depicted in **a)** and **b)**. In figures with $\Omega_c < \Gamma_{eg}$ the EIT feature with a width much smaller than the natural linewidth is visible (**b)**). For large coupling Rabi frequencies the absorption line splits according to the Autler-Townes splitting (**c)**). The dephasing rate γ_{ed} basically broadens the line, but the visibility of the EIT feature is unbowed (**d)** to **f)**). The EIT signal vanishes if the dephasing rate γ_{rd} is increased (**g)** to **i)**).

Fano interference [Fan61] of the two excitation paths from $|g\rangle$ to $|+\rangle$ and $|g\rangle$ to $|-\rangle$, leading to zero absorption on the probe transition from $|g\rangle$ to $|e\rangle$. The absorption is proportional to the imaginary part of the susceptibility χ, which in turn is a function of the coherence ς_{eg} between the states $|e\rangle$ and $|g\rangle$.

The coherence ς_{eg}, among other properties, of the three-level atom can be obtained from the MatLab program given in appendix A.3, which calculates the density matrix entries for a three level atom according to to equation (1.11). Some results of these calculations are shown in figure 1.6 in order to illustrate the expected signals for different values of the coupling Rabi frequency Ω_c and dephasing rates γ_{ed} and γ_{rd}.

Figure 1.6 b) shows an EIT feature in the case $\Gamma_{eg} > \Omega_c$. The width of this feature is smaller than the linewidth Γ_{eg} of the absorption line without coupling laser (see figure 1.6 a)). In the case where $\Omega_c > \Gamma_{eg}$ the EIT feature vanishes and Autler-Townes splitting appears (see figure 1.6 c)). Figures 1.6 d) to i) show the behaviour of the EIT signal for different values of the dephasing rates γ_{ed} and γ_{rd}. If the dephasing rate γ_{ed} of the intermediate state is increased the linewidth of the signal increases, while the visibility of the EIT feature stays unaltered. On the other hand, increasing the dephasing rate of the Rydberg level γ_{rd} results in a decreasing depth of the EIT feature, which even vanishes for large dephasing rates.

Observing an EIT feature is a direct proof for the coherence of the system since the feature is smaller than the linewidth due to the lifetime of the state. Hence, for the observation it is necessary to cancel out the effects of the radiative state. This is, in case the lasers are switched on, only possible via a coherent superposition of the two remaining states.

1.8. Effective two-level atom

The physics of a three-level atom is very much enriched by the third level. However, along with the third level comes the, in comparison with the the two-level atom, much more complicated description of the system.

Under some circumstances it is possible to describe a three-level atom as an effective two-level atom. The requirement for this is, that one of the three levels must not be occupied, at least not significantly. Here it is the intermediate state $|e\rangle$ into which no atom should be excited. This can be achieved by choosing a detuning δ_p (see figure 1.4 for clarification of the symbols) that is large compared to the Rabi frequencies Ω_p and Ω_c. A large detuning from the intermediate state is especially important for the coherent excitation of Rydberg atoms involving the intermediate state as its decay rate Γ_{eg} causes an incoherent scattering of photons.

In the case that $\delta_p \gg \Omega_p\Omega_c$ and the decay rate Γ_{eg} is large compared to Γ_{re}

the state $|e\rangle$ can be adiabatically eliminated [Mey01]. This means, that the fast varying variable ς_{ee} is removed from the system by solving the Lindblad equation with $\dot{\varsigma}_{ee} = 0$. Finally, this results in an effective Hamiltonian [Bri07]

$$\mathcal{H}_{\text{eff}} = \frac{\hbar}{2} \begin{pmatrix} -\delta_{\text{eff}} & \Omega'_{\text{eff}} \\ \Omega'^{*}_{\text{eff}} & \delta_{\text{eff}} \end{pmatrix} . \tag{1.35}$$

On two-photon resonance the effective Rabi frequency is given by

$$\Omega_{\text{eff}} = \frac{\Omega_{\text{p}}\Omega_{\text{c}}}{2\delta_{\text{p}}} , \tag{1.36}$$

and the effective detuning is

$$\delta_{\text{eff}} = \delta_{\text{c}} + \frac{\Omega_{\text{p}}^2}{4\delta_{\text{p}}} - \frac{\Omega_{\text{c}}^2}{4\delta_{\text{p}}} . \tag{1.37}$$

With equation (1.20) the off-resonant two-photon detuning becomes

$$\Omega'_{\text{eff}} = \sqrt{\Omega_{\text{eff}}^2 + \delta_{\text{eff}}^2} . \tag{1.38}$$

Coherent effects, e.g. Rabi oscillations, can be observed on a timescale $\tau = {}^{1}/_{\Omega_{\text{eff}}}$ if no dephasing or decoherence happens on this timescale. Considering a decay rate $\Gamma \simeq \Gamma_{\text{re}}$ results with equation (1.15) in a scattering rate

$$\Gamma_{\text{s}} \equiv \Gamma\varsigma'_{ee} = \frac{\Gamma\,\Omega_{\text{p}}^2}{4\delta_{\text{p}}^2 + \Gamma^2 + 2\Omega_{\text{p}}^2} , \tag{1.39}$$

which is for large δ_{p}

$$\Gamma_{\text{s}} \simeq \frac{\Gamma\,\Omega_{\text{p}}^2}{4\,\delta_{\text{p}}^2} . \tag{1.40}$$

Another issue of decoherence is a dephasing rate γ_{d} due to, for example, collisions, laser linewidths or interaction between atoms. For a coherent evolution of the system any decay or decoherence rate must be smaller than the Rabi frequency on two-photon resonance: $\Omega_{\text{eff}} > (\Gamma_{\text{s}}, \gamma_{\text{d}})$. This results with equations (1.36) and (1.40) in the inequality

$$\frac{2\,\Omega_{\text{c}}}{\Gamma} > \frac{\Omega_{\text{p}}}{\delta_{\text{p}}} > \frac{2\gamma_{\text{d}}}{\Omega_{\text{c}}} , \tag{1.41}$$

which leads to the requirement $\Omega_{\text{c}} > \sqrt{\Gamma\,\gamma_{\text{d}}}$ for the second Rabi frequency in the two-photon excitation. Thus, the task of maximising Ω_{eff} given by equation (1.36) must be achieved by maximising the Rabi frequency Ω_{c} of the

upper transition rather than maximising the fraction Ω_P/δ_p in order to assure that the effective two-photon Rabi frequency is larger than any decoherence or dephasing.

Especially the technical aspect of minimising γ_d, i.e. minimising the laser linewidth, is subject of section 6.2. The contribution to γ_d caused by the interaction between Rydberg atoms will be subject of experimental investigation described in section 9.3.

2. Rydberg atoms

Rydberg atoms are atoms with at least one electron excited to a high principal quantum number. The large distance of this electron to its core determines the most physical properties of Rydberg atom and make them interesting for quantum computing issues [Jak00, Luk01].
This chapter will only briefly introduce the properties of Rydberg atoms that are important with respect to this thesis. Moreover, only atoms with one electron excited to a Rydberg state will be discussed, as no other is used in this thesis. For more details on Rydberg atoms see [Gal94, Gra06, Hei08a]. The first section 2.1 introduces the basic properties of Rydberg atoms. Section 2.2 focuses on the interaction between Rydberg atoms, especially on the van der Waals interaction, which is the dominant interaction for Rydberg atoms used for the experiments in this thesis.

2.1. Basic properties

The simplest picture of a Rydberg atom is an electron orbiting the core in analogy to the Bohr model of the hydrogen atom. In a hydrogen atom the electron is attracted by a Coulomb potential. The energy and the classical radius for a hydrogen atom with an electron in a state with principal quantum number n is given by

$$E_n = -\frac{R_\infty hc}{n^2}\,, \tag{2.1}$$

$$r_n = a_0 n^2\,, \tag{2.2}$$

with the Bohr radius a_0 and the Rydberg constant R_∞

$$R_\infty = \frac{m_e e_0^4}{8\epsilon_0^2 h^3 c}\,. \tag{2.3}$$

Due to the similarity between a hydrogen atom and an alkali atom equations (2.1) and (2.2) can to some degree be used for the description of alkali Rydberg atoms. In alkali atoms the potential of the core with Z positive charges is shielded by $Z-1$ core electrons. The probability to find the electron in the vicinity of the core is small for large angular quantum numbers $l > 4$

and since the energy shift due to the $Z-1$ core electrons are small and the Rydberg electron basically experiences only a $1/r$-potential these states are called 'hydrogen like states'. Rydberg states with a smaller angular momentum $l < 4$ are called 'defect states'. The energy shift due to the core electrons constitutes a significant perturbation to the $1/r$-potential. This energy shift can be taken into account by replacing the principal quantum number n with an effective principal quantum number $n^* = n - \delta_l$, with the 'quantum defect' δ_l [Gal94]. By doing so basically all discovered properties can be translated from the hydrogen atom to the alkali atoms. Table 2.1 lists the, with respect to this thesis, most important properties and their dependence on n^*.

Property	Symbol or expression
Binding energy	$E_n = -R_\infty hc\,(n^*)^{-2}$
Level spacing	$\Delta = E_n - E_{n-1} \sim (n^*)^{-3}$
Radius	$\langle r \rangle = (3(n^*)^2 - l(l+1))/2$
Geometric cross section	$\pi \langle r \rangle^2 \sim (n^*)^4$
Dipole moment	$d = \langle nl \vert\, e\boldsymbol{r} \,\vert nl' \rangle \sim (n^*)^2$
Polarisability	$\alpha \sim (n^*)^7$ [Gra06]
Lifetime (spontaneous decay)	$\tau_{\mathrm{lt}} = 1.43(n^*)^{2.94}$
Lifetime (black body radiation)	$\tau_{\mathrm{bb}} = {}^{3\hbar}/_{(4\alpha^3 k_{\mathrm{B}} T)}\,(n^*)^2$
van der Waals coefficient	$C_6 \sim (n^*)^{11}$

Table 2.1.: Most important properties and dependences on the effective principal quantum number n^* for alkali atoms in Rydberg states. All entries, if not cited differently, were taken from [Gal94].

2.2. Interaction between Rydberg atoms

The dipole-dipole interaction is the dominant interaction between atoms at moderate densities, where the contact interaction becomes more and more pronounced for increasing atomic densities. One can distinguish two types, namely the magnetic and the electric dipole-dipole interaction.

The interaction energy between two dipoles $\boldsymbol{d}_1$ and $\boldsymbol{d}_2$ separated by a distance $\boldsymbol{r}$ and aligned along the same axis with an angle θ to $\boldsymbol{r}$ is given by

$$\begin{aligned} \mathcal{V}_{\mathrm{dd}}^{\mathrm{el}} &= \frac{d_1^{\mathrm{el}} d_2^{\mathrm{el}}}{r^3} \cdot (1 - 3\cos^2\theta)\,, \\ \mathcal{V}_{\mathrm{dd}}^{\mathrm{mag}} &= \frac{d_1^{\mathrm{mag}} d_2^{\mathrm{mag}}}{r^3} \cdot (1 - 3\cos^2\theta)\,. \end{aligned} \tag{2.4}$$

The strength of both interactions can be compared by comparing their coupling constants, which are d^2/ϵ_0 and $\mu_0\mu^2$ for the electric and magnetic dipole-dipole interaction, respectively. The comparison of both constants yields a factor of $(\alpha_{\mathrm{S}}/2)^2$, with the Sommerfeld fine structure constant α_{S}. Thus, the magnetic dipole-dipole interaction is roughly a factor of 75000 weaker than its electric counterpart.

The electric dipole moment $d^{\mathrm{el}} \sim n^2$ can be several orders magnitude larger than the magnetic dipole moment, which scales maximal as $d^{\mathrm{mag}} \sim n^1$ for $\ell = n - 1$. However, for neutral atoms in the ground state the magnetic dipole moment is sufficient to trap atoms as it will be discussed in chapter 5. High magnetic moments, up to $10\mu_{\mathrm{B}}$ have been observed with neutral atoms [Han04]. For large magnetic moments and small distances R, i.e. high densities, effects of the magnetic dipole-dipole interaction can be observed [Stu05].

The magnetic dipole-dipole interaction between Rydberg atoms can be neglected in comparison to the electric dipole-dipole interaction. Usually unperturbed atoms do not have a permanent electric dipole moment. Electric ac dipoles however can be induced by applying an electric field or by means of Förster resonances [För48] using the degeneracy of two pair states, e.g. $n\mathrm{s} + n\mathrm{s} \leftrightarrow (n-1)\mathrm{p} + (n+1)\mathrm{p}$.

In this thesis the $43\mathrm{S}_{1/2}$ Rydberg state is solely used. This state has no Förster resonance at moderate electric fields. The next order in the perturbation theory after the dipole-dipole interaction given in equation (2.4) is the van der Waals interaction. The van der Waals interaction can be understood as a dipole-dipole interaction between a fluctuating dipole in one atom, which induces a dipole in a second atom. In a quantum mechanical treatment the classical dipoles d^{el} in equation (2.4) are replaced by matrix elements $\langle\phi|\, e\boldsymbol{r}\,|\phi'\rangle$, where the prime denotes the final state. Neglecting the spatial orientation of

the dipoles the potential of the dipole-dipole interaction between two atoms in the states $|\phi_1\rangle$ and $|\phi_2\rangle$ is in terms of the pair states $|\phi_1\phi_2\rangle$ given by

$$\mathcal{V}_{\mathrm{dd}} \sim \sum_{|\phi_1'\phi_2'\rangle} \langle\phi_1\phi_2| \frac{d_1 d_2}{R^3} |\phi_1'\phi_2'\rangle \tag{2.5}$$

Figure 2.1 shows the coupling of three states into pair states considering two Rydberg atoms in equal states $|s\rangle$ and only the neighbouring states $|p\rangle$ and $|p'\rangle$, which angular momenta shall be $l_p = l_{p'} = l_s \pm 1$.

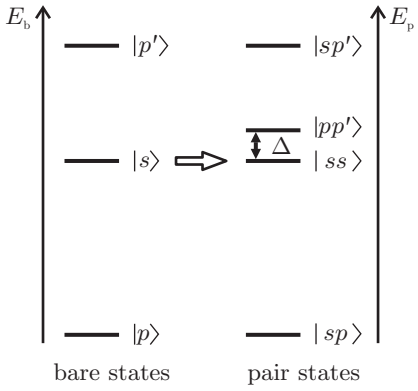

Figure 2.1.: Coupling of the atomic states to pair states due to the interaction between two dipoles. The origin of the dipole-dipole interaction between two atoms in the state $|s\rangle$ can be understood as a fluctuating dipole inducing a dipole in an atom at distance R (van der Waals interaction). This picture assumes that all atoms are in $|s\rangle$. The energy splitting $E_s - E_p$ and $E_{p'} - E_s$ is large compared to $\Delta = E_{ss} - E_{pp'}$.

The energy differences between the atomic states are large compared to the energy difference of the paired state $|ss\rangle$ and $|pp'\rangle$. Equation (2.5) can be rewritten in terms of a two-level atom in the basis $|ss\rangle = (1,0)^{\mathrm{t}}$ and $|pp'\rangle = (0,1)^{\mathrm{t}}$ as

$$\mathcal{H}_{\mathrm{dd}} = \begin{pmatrix} 0 & \frac{d_1 d_2}{R^3} \\ \frac{d_1 d_2}{R^3} & \Delta \end{pmatrix}, \tag{2.6}$$

with $\Delta = (E_s - E_p) - (E_{p'} - E_s) = E_{ss} - E_{pp'} < 0$. In this picture the atomic states are coupled to the pair states due the interaction between the dipoles d_1 and d_2. Diagonalisation of (2.6) leads to the new eigenenergies

$$E_{\pm} = \frac{\Delta}{2} \pm \sqrt{\left(\frac{\Delta}{2}\right)^2 + \left(\frac{d_1 d_2}{R^3}\right)^2}. \tag{2.7}$$

Usually the energy difference Δ is non-zero. For large distances R one can expand (2.7), which leads in the case $\Delta \gg {}^{d_1 d_2}/_{R^3}$ to the eigenenergy of $|ss\rangle$

$$E_{\mathrm{vdW}} = E_- = -\frac{1}{\Delta} \frac{(d_1 d_2)^2}{R^6} \equiv \frac{C_6}{R^6}. \tag{2.8}$$

The van der Waals C_6 coefficient is proportional to $1/\Delta$, hence the sign of the interaction can be positive (repulsive) or negative (attractive) depending on the energies E_{ss} and $E_{pp'}$. In the case of ^{87}Rb the interaction between two Rydberg atoms in an nS state is for $14 \leq n \leq 236$ repulsive [Sin05], while the interaction between Rydberg atoms in an nD state are predominantly attractive [Sin04a]. Due to the scalings of $1/\Delta$ with n^{-3} and d with n^2 (see table 2.1) the C_6 coefficient scales $\sim n^{11}$.

The case of a vanishing energy difference Δ is called Förster resonance: Equation (2.7) has again the form of a dipole-dipole interaction with the energy $E_F = d_1 d_2 / R^3$. Although it has been mentioned above that $\Delta \neq 0$ for most of the atoms, $\Delta = 0$ still can be achieved by tuning the energies E_s, E_p and $E_{p'}$ using an electric field. In other words it is possible to tune the range of the interaction from a van der Waals to the long range dipole-dipole interaction by means of the electric field using the Förster resonance at $\Delta = 0$.

3. Collectivity

Strong interactions change the dynamics of a system considerably. If an atom is excited into a Rydberg state the van der Waals interaction suppresses the excitation of a second Rydberg atom in its vicinity. The smallest distance between two Rydberg atoms is called blockade radius, which is introduced in section 3.1. The suppression of the excitation into the Rydberg state leads to collective effects on the excitation and the formation of collective states. The collective excitation of many ground state atoms due to the blockade is covered by section 3.2.
Collective effects on the excitation into a Rydberg state are investigated in a thermal cloud in reference [Hei07] as well as in Bose-Einstein condensates in reference [Hei08b]. The validity of the concepts briefly introduced in this chapter is shown in this references.
The last two sections of this chapter introduces the simple, though, powerful superatom model (section 3.3) and its generalisation (section 3.4). The description of the excitation dynamics in terms of the superatom model will be of importance for the interpretation of the results of the universal scaling presented in chapter 8.

3.1. The blockade radius

If the interaction between the Rydberg atoms becomes large compared to all other energy scales in the system, i.e. to the natural linewidth Γ and the power broadened linewidth of the Rydberg state caused by the Rabi frequency Ω, the excitation of more than one atom into the Rydberg state is blocked. An example is shown in figure 3.1 for a purely repulsive van der Waals interaction as it will be the case in the experiments presented in this thesis. Two atoms with ground state $|\mathrm{g}\rangle$ and Rydberg state $|\mathrm{r}\rangle$can be described in terms of pair states $\{|\mathrm{g,g}\rangle, |\mathrm{g,r}\rangle, |\mathrm{r,g}\rangle, |\mathrm{r,r}\rangle\}$, where $|\mathrm{g,r}\rangle$ for example denotes atom one in the ground state and atom two in the Rydberg state. Due to the small polarisability of the ground state atoms the energy of the states $|\mathrm{g,g}\rangle$ and $|\mathrm{g,r}\rangle$ is not shifted. The van der Waals interaction shifts the energy level of the state $|\mathrm{r,r}\rangle$ out of the laser resonance. This energy shift depends on the distance r

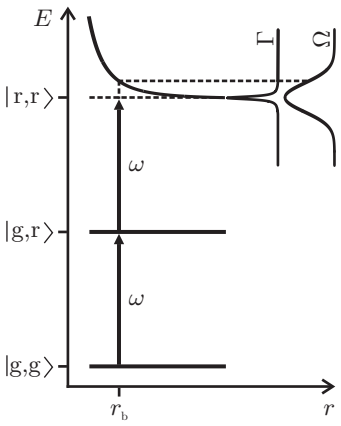

Figure 3.1.: Blockade of the Rydberg excitation due to the van der Waals interaction. A laser with frequency ω drives the transition $|\mathrm{g}\rangle$ to $|\mathrm{r}\rangle$ from the ground state to the Rydberg state. Considering two atoms, the energies of the pair states $|\mathrm{g,g}\rangle$ and $|\mathrm{g,r}\rangle$ remain unshifted due to the small polarisability of the ground state atom. The transition $|\mathrm{g,r}\rangle$ to $|\mathrm{r,r}\rangle$ however is dependent on the interparticle distance r because the energy level is shifted due to van der Waals interaction between the two Rydberg atoms. Dependent on the larger of both 'linewidths', Γ or Ω, one can define a blockade radius r_b, which is the smallest distance between two Rydberg atoms.

between the two atoms. A transition from $|\mathrm{g,r}\rangle$ to $|\mathrm{r,r}\rangle$ is suppressed if

$$\mathcal{V}_\mathrm{vdW} = \frac{C_6}{r^6} > \hbar \max(\Gamma, \Omega)\,. \tag{3.1}$$

Assuming that the decay rate of the Rydberg state Γ is much smaller than the Rabi frequency Ω, as it is the case in the experiments presented in this thesis, the blockade radius is defined as

$$r_\mathrm{b} \equiv \sqrt[6]{\frac{C_6}{\hbar\Omega}}\,. \tag{3.2}$$

The blockade radius defines a smallest volume $V_\mathrm{b} = {}^{4\pi}/_{3} \cdot r_\mathrm{b}^3$ in which only one atom can be excited into a Rydberg state.

3.2. Collective states

The experiments discussed in this thesis are conducted in a system with large atom numbers and high densities. Thus, the volume of a blockade sphere given by r_b contains up to several thousand ground state atoms. Taking this into account changes the excitation dynamics completely from a single atom behaviour to a collective behaviour.
Considering N interacting two-level atoms that are driven with a Rabi frequency Ω_0 results in a Hamiltonian in the $|\mathrm{g}\rangle = (1,0)^\mathrm{t}$ and $|\mathrm{r}\rangle = (0,1)^\mathrm{t}$ basis

$$\mathcal{H} = \sum_{j=1}^{N} \mathcal{H}_j^\mathrm{s} + \sum_{k<l} \mathcal{V}_{kl}\, \frac{1}{2}(\mathbb{1} - \boldsymbol{\sigma}_z)_k\, \frac{1}{2}(\mathbb{1} - \boldsymbol{\sigma}_z)_l\,, \tag{3.3}$$

with the single atom Hamiltonian

$$H_j^{\mathrm{s}} = \frac{\hbar}{2}\Omega_0 \left(\boldsymbol{\sigma}_x\right)_j + \frac{\hbar}{2}\delta \left(\mathbb{1} - \boldsymbol{\sigma}_z\right)_j \tag{3.4}$$

and the well known Pauli matrices

$$\boldsymbol{\sigma}_x = \begin{pmatrix} 0 & 1 \\ 1 & 0 \end{pmatrix}, \boldsymbol{\sigma}_y = \begin{pmatrix} 0 & -i \\ i & 0 \end{pmatrix}, \boldsymbol{\sigma}_z = \begin{pmatrix} 1 & 0 \\ 0 & -1 \end{pmatrix}. \tag{3.5}$$

The index j, k and l accordingly, denote the subspace of the Hilbert space for the respective atom. Equation (3.4) is in analogy to (1.10) with a shifted zero energy. Dissipation according to (1.13) is not taken into account as for Rydberg states the lifetime is large and, thus, Γ is small. Moreover, in the experiments presented in this thesis the Rabi frequency Ω_0 is much larger than the decay rate Γ.

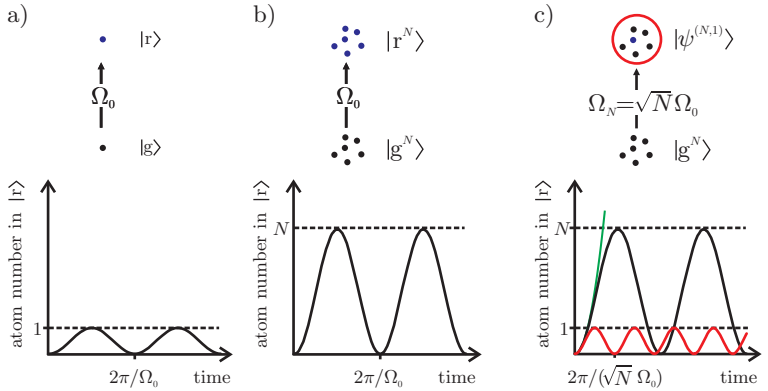

Figure 3.2.: Three different types of coherent excitation. **a)** Single atom Rabi oscillation occurs if an atom is driven by a Rabi frequency Ω_0. **b)** N non-interacting atoms undergo the same Rabi oscillation. The amplitude of the population in state $|\mathrm{r}\rangle$ equals N. **c)** In the case of a collective excitation all N atoms carry one excitation. The amplitude of the population in the Rydberg state is one and the the frequency of the Rabi oscillation is enhanced by a factor of $\sqrt{N}$ (red curve). The collective state, depicted by a red circle is sometimes called superatom and is the subject of section 3.3. The green parabola indicates the quadratic onset of the non-interacting excitation.

At this point, depending on the strength of the interaction $\mathcal{V}_{kl}$, three different excitations can be distinguished. Figure 3.2 depicts in a) the single

atom excitation, in b) the excitation of N non-interacting atoms and in c) the collective excitation in the presence of strong interaction. The ground state of the system is

$$\left|\psi^{(N,0)}\right\rangle = |\mathrm{g}_1,\mathrm{g}_2,\ldots,\mathrm{g}_N\rangle \ . \tag{3.6}$$

Exciting the jth atom result in a state $|\mathrm{g}_1,\mathrm{g}_2,\ldots,\mathrm{r}_j,\ldots,\mathrm{g}_N\rangle$. Due to symmetry with respect to permutation the collective state with one excitation reads

$$\left|\psi^{(N,1)}\right\rangle = \frac{1}{\sqrt{N}} \sum_{j=1}^{N} |\mathrm{g}_1,\mathrm{g}_2,\ldots,\mathrm{r}_j,\ldots,\mathrm{g}_N\rangle \ , \tag{3.7}$$

if the phases between all states are one. In general the atoms forming the collective state have distances larger than the wavelength of the excitation light and therefore experience individual phases of the light field.

Calculating the matrix element for the transition from the ground state $\left|\psi^{(N,0)}\right\rangle$ to $\left|\psi^{(N,1)}\right\rangle$ yields

$$\left\langle\psi^{(N,1)}\right| \sum_{j=1}^{N} \frac{\hbar}{2}\Omega_0(\boldsymbol{\sigma}_x)_j \left|\psi^{(N,0)}\right\rangle = \sum_{j=1}^{N} \frac{1}{\sqrt{N}}\frac{\hbar}{2}\Omega_0 = \frac{\hbar}{2}\Omega_N \ , \tag{3.8}$$

with the collective Rabi frequency

$$\Omega_N = \sqrt{N}\Omega_0 \ . \tag{3.9}$$

The appearance of the $\sqrt{N}$ factor is typical for a collective excitation. The N ground state atoms inside the blockade sphere equally share one excitation and form a two-level 'superatom' [Vul06] with the states $\left|\psi^{(N,0)}\right\rangle$ and $\left|\psi^{(N,1)}\right\rangle$. In contrast to the usual two-level atom the superatom oscillates with an Rabi frequency, which is enhanced by a factor of $\sqrt{N}$.

The effective Hamiltonian for the collective excitation has form (see equation (1.10))

$$\mathcal{H} = \frac{\hbar}{2}\begin{pmatrix} 0 & \Omega_N \\ \Omega_N^* & 2\delta \end{pmatrix} . \tag{3.10}$$

The interaction from the Hamiltonian in (3.3) is absorbed in the collective Rabi frequency and the appearance of $\left|\psi^{(N,1)}\right\rangle$. The picture given in figure 3.2 c) illustrates the superatom oscillating with the collective Rabi frequency between the states $\left|\psi^{(N,0)}\right\rangle$ and $\left|\psi^{(N,1)}\right\rangle$.

The collective state was introduced as an effect of strong interaction. Strong means to have only one excitation in N atoms, the excitation into the state $\left|\psi^{(N,2)}\right\rangle$ with two excitation must be impossible. The strength of the transition $\left|\psi^{(N,1)}\right\rangle$ to $\left|\psi^{(N,2)}\right\rangle$ is given by the matrix element [Hei08a]

$$\left\langle\psi^{(N,2)}\right| \sum_{j=1}^{N} \frac{\hbar}{2}\Omega_0(\boldsymbol{\sigma}_x)_j \left|\psi^{(N,1)}\right\rangle = \sqrt{2(N-1)}\,\frac{\hbar}{2}\Omega_0\,. \tag{3.11}$$

Thus, the interaction between the Rydberg atoms must be much stronger than the corresponding energy of the excitation into the state $\left|\psi^{(N,2)}\right\rangle$

$$\mathcal{V}_{kl} \gg \sqrt{2(N-1)}\,\frac{\hbar}{2}\Omega_0\,. \tag{3.12}$$

3.3. The superatom model

The introduction above assumes only one superatom formed by all N available atoms. This is valid if the N atoms are placed in a sphere with radius r_b. In the experiments in this thesis the size of the atomic cloud will be larger than this sphere, which means that many superatoms will be found.

In principle an exact solution of the dynamics could be obtained by solving the Schrödinger equation using the Hamiltonian from (3.3). Due to number of atoms of real systems the Hilbert space would have 2^N, with $N \approx 10^7$, dimensions, which is impossible to solve. Several approaches to circumvent this problem by lowering the dimensions of the Hilbert space and, never the less describing the system accurately have been made. Ates and coworkers derive in [Ate07] a solution by substituting the quantum correlations between all N atoms with simpler rate equations. This approach works under certain conditions, i.e. in systems with a low density of atoms. Tong and coworkers favoured a mean field approach [Ton04] solving the Bloch equation for a superatom. The pair correlation function for Rydberg atoms are calculated by Robicheaux *et al.* [Rob05].

For the superatom model this pair correlation function is assumed to be a Heaviside function, resulting in separated spheres with a radius of $r_\mathrm{b}/2$. Figure 3.3 shows the arrangement of the superatoms assuming close sphere packing. The close sphere packing minimises the energy by maximising the distance between the atoms for a given volume.

Generally, the density distribution n_g of ground state atom is not constant, but a function of the spatial coordinate r. Assuming that $n_\mathrm{g}(r)$ is not varying too much on the length scale of the blockade radius one can use the local

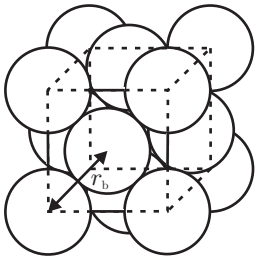

Figure 3.3.: Arrangement of superatoms in a close sphere packing. The distance between the centres of two superatoms and their diameter is the blockade radius r_b.

density approximation to calculate the dynamics of the superatoms. It has also to be stressed that in the simple superatom model the superatoms are assumed to be non-interacting. The interaction between superatoms would require a detailed knowledge of the pair correlation function and is currently subject to theoretical investigation.

The spatial dependence of the density distribution of ground state atoms results in a spatial variation of the number N of ground state atoms constituting a superatom. With the density of Rydberg atoms n_R in the saturation regime the number of atoms per superatom is

$$N(r) = \frac{n_\mathrm{g}(r)}{n_\mathrm{R}(r)}\,, \tag{3.13}$$

and with this the collective Rabi frequency becomes according to

$$\Omega_N(r) = \sqrt{N(r)}\Omega_0\,, \tag{3.14}$$

a function of the spatial coordinate.

From figure 3.3 the density of Rydberg atoms is $n_\mathrm{R} = \sqrt{2}r_\mathrm{b}^{-3}$. Therefore, equation (3.2) becomes

$$\frac{ZC_6}{r_\mathrm{b}^6(r)} = ZC_6\frac{1}{2}n_\mathrm{R}^2(r) = \kappa\hbar\Omega_N(r)\,, \tag{3.15}$$

with $Z = 14.4$ accounting for the next and next-next neighbours interacting via the van der Waals interaction. The factor $\kappa \simeq 1$ is constant and accounts for the factor $\sqrt{2}$ in (3.12).

The density of Rydberg atoms and the collective Rabi frequency can be calculated from the density of ground state atoms and the single atom Rabi frequency using equations (3.13) and (3.15)

$$n_\mathrm{R}(r) = \left(\frac{2\kappa\hbar}{ZC_6}\right)^{2/5}(n_\mathrm{g}(r)\Omega_0^2)^{1/5}\,, \tag{3.16}$$

$$\Omega_N(r) = \left(\frac{ZC_6}{2\kappa\hbar}\right)^{1/5}(n_\mathrm{g}(r)\Omega_0^2)^{2/5}\,. \tag{3.17}$$

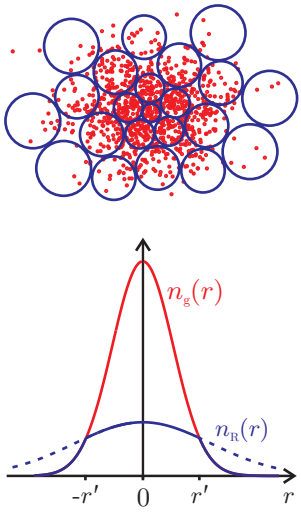

Figure 3.4.: Illustration of the density of Rydberg atoms (blue) in a harmonic trap. The red dots symbolise the ground state atoms, the blue circles are the superatoms. The blockade radius is dependent on the spatial coordinate. The superatom model breaks down at the position $\pm r'$ where the atomic ground state density $n_g(\pm r')$ equals the Rydberg density $n_R(\pm r')$. For $|r| > r'$ the density of Rydberg atoms follows the density of ground state atoms (red), which is equivalent of a single atom behaviour. For $|r| < r'$ the Rydberg density is according to equation (3.16) $n_R \sim n_g^{1/5}$.

The experiments described in this thesis are solely done in a thermal cloud of atoms trapped in a potential, which can be approximated to be harmonic. Hence, the density distribution n_g equals a Gaussian distribution with a width σ_r. Figure 3.4 illustrates the situation in such a trap, where for simplicity the cloud is assumed to be round.

The density of Rydberg atoms and the collective Rabi frequency given by equations (3.16) and (3.17) are valid as long as $|r| < r'$, where r' is given by $n_g(\pm r') = n_R(\pm r')$. The Gaussian width of n_R is a factor of $\sqrt{5}$ larger than the width of n_g. Hence n_R would exceed n_g for $|r| > r'$, which would be unphysical. For $|r| > r'$ the superatom model breaks down and the dynamics is given by a simple single atom behaviour, i.e. $n_g(r) = n_R(r)$ and $\Omega_N(r) = \Omega_0$.

The Rydberg atom number N_R at a time τ can be calculated using equations (3.13) and (3.15)

$$N_R(\tau) = \int n_R(r) \sin^2\left(\frac{1}{2}\Omega_N(r)\tau\right) \mathrm{d}^3 r\,. \tag{3.18}$$

The integral simply sums the contribution of every superatom, whose excitation oscillates with its collective Rabi frequency. These Rabi oscillations are however not observable in our experiments due to the distribution of $\Omega_N(r)$ in a harmonic trap. To clarify this argument figure 3.2 c) has to be modified. The result is shown in figure 3.5.

Every superatom is oscillating with its own local collective Rabi frequency. The sum of all these oscillations leads to a saturation curve. This excitation

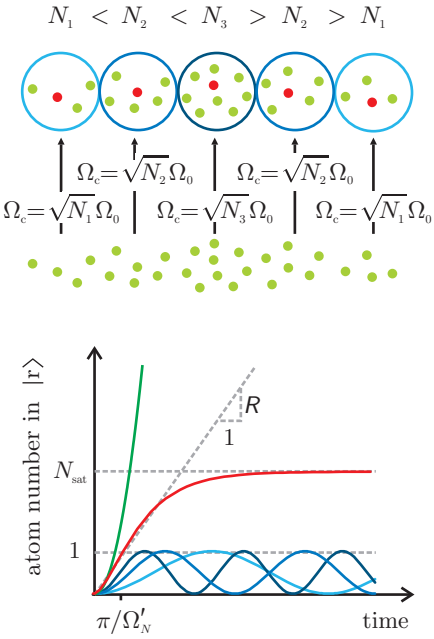

Figure 3.5.: Rydberg excitation dynamics in the superatom picture. Due to the inhomogeneous density distribution $n_g(r)$, every superatom is oscillating with the local collective Rabi frequency $\Omega_N(r)$. The Rydberg atom number at time τ is the sum of the contributions of all superatoms. Hence, instead of visible Rabi oscillations (blue) a smeared out saturation curve (red) is found. This curve can, in good approximation, be characterised by the initial slope R and the saturation value N_{sat}. The green curve indicates again the quadratic onset of the function for excitation times shorter than π/Ω'_N.

curve shows a quadratic onset for times $\tau < \pi/\Omega'_N$, where Ω_N is the averaged collective Rabi frequency. For longer times the dynamics evolves linearly with a slope R and finally saturates to a value N_{sat}. These two variables, R and N_{sat} can be used to characterise the dynamics, especially to gain insight about the type of the dynamics and the underlying interaction. This is done by investigating the scaling behaviour of R and N_{sat} with n_g and Ω_0, which was systematically done in [Hei08a, Hei08b].

3.4. Generalisation of the superatom model

Since this thesis will discuss the scaling behaviour of the Rydberg excitation for different spatial dimensions (see chapter 8) it is required to generalise the superatom model, that was introduced in the last section for the case of three dimensions. This has already been done in reference [Hei08a] and only the most important points for this thesis will be repeated here.

Rydberg excitation can be categorised by three different regimes, namely the incoherent dynamics, the coherent single atom dynamics and, finally, the coherent collective dynamics. The distinction is due to the dominating fre-

quency in the system. In the case of an incoherent dynamics the decay rate Γ dominates over both, the single atom Rabi frequency Ω_0 and collective Rabi frequency Ω_N. If $N \leq 1$ and $\Omega_0 > \Gamma$ the dynamics will follow the prediction of the coherent individual dynamics. Finally, if $N \gg 1$ and, thus, $\Omega_N > (\Gamma, \Omega_0)$ the scaling behaviour of R and N_{sat} will follow the predictions given by equations (3.16) and (3.17) for a coherent collective dynamics in a strong interacting system.

Regime	Dominating frequency	R	N_{sat}
incoherent	Γ	$n_0\Omega_0^2/\Gamma$	$n_0\Omega_0^2/\Gamma$
coherent, individual	Ω_0	$n_0\Omega_0$	n_0
coherent, collective	$\Omega_N \propto (n_0\Omega_0^2)^{\beta/(2\beta+1)}$	$\Omega_N^{(\beta+1)/\beta}$	$\Omega_N^{1/\beta}$

Table 3.1.: Overview over the scaling laws for the three regimes of Rydberg excitation [Hei08a]. The scaling in the coherent collective regime are obtained from a generalisation of equations (3.16) and (3.17). The exponent $\beta = p/d$ depends on the power of the r-dependence of the potential, i.e. $\mathcal{V} \sim r^{-p}$, and the dimensionality d of the system.

Interaction	d	p	β	μ_R	μ_{sat}
dipole-dipole	1	3	3	$4/7$	$1/7$
	2	3	$3/2$	$5/12$	$1/4$
	3	3	1	$2/3$	$1/3$
van der Waals	1	6	6	$7/13$	$1/13$
	2	6	3	$4/7$	$1/7$
	3	6	2	$3/5$	$1/5$

Table 3.2.: Scaling of the characteristics $R \sim (n_0\Omega_0^2)^{\mu_R}$ and $N_{\mathrm{sat}} \sim (n_0\Omega_0^2)^{\mu_{\mathrm{sat}}}$ of the excitation curve with the exponent $\beta = p/d$ of n_{R} for different interactions and dimensions.

The general form of the blockade condition introduced in equation (3.2) in terms of the density of Rydberg atoms reads

$$n_{\mathrm{R}}^{\beta} \sim \max(\Gamma, \Omega_0, \Omega_N)\,. \tag{3.19}$$

The exponent of the power law is $\beta = p/d$. It is given by the power p of the

$1/r$-dependence in the interaction, i.e. $\mathcal{V} \sim r^{-p}$, and the dimension d of the system.

The generalised scaling laws for R and N_{sat} are found by using equation (3.19) and

$$\begin{aligned} R \quad &\sim {}^{N_{\mathrm{R}}(\tau)}/_{\tau} \sim V n_{\mathrm{R}}(\tau)\, \Omega_N \sim n_{\mathrm{R}}(\tau)\, \Omega_N \,, \\ N_{\mathrm{sat}} &\sim N_{\mathrm{R}}(\tau) \sim V n_{\mathrm{R}}(\tau) \sim n_{\mathrm{R}}(\tau) \,, \end{aligned} \tag{3.20}$$

with a volume V from the integral in (3.18).

Table 3.1 gives an overview over these scaling laws of R and N_{sat} with the peak density of ground state atoms n_0 and Ω_0 in the different regimes. For the investigation of the scaling behaviour it is sufficient to replace the density of ground state atoms $n_{\mathrm{g}}(r) = n_0 \tilde{n}_{\mathrm{g}}(r)$ by its peak value n_0. This is possible as long as $\tilde{n}_{\mathrm{g}}(r)$ is fixed for all experiments.

Table 3.2 summarises the expected exponents and the dependence of R and N_{sat} on n_0 and Ω_0 for the dipole-dipole and the van der Waals interaction.

4. Universal Scaling

Universal scaling laws are a very powerful tool in physics and other fields of science, which gives the opportunity to describe the behaviour of a system without actually knowing all details on the microscopic length scale. Examples can be found everywhere in nature. For instance the number of heart beats in the lifetime is the approximately the same for all mammals and the metabolic rate of organisms, completely independent of their exact microscopic realisation, can be described using the same power law within 27 orders of magnitude in mass [Wes04].
This chapter aims to introduce universal scaling to the issue of Rydberg excitation very briefly. A comprehensive description will be found in H. Weimer's thesis. In order to understand the rather abstract concept it is helpful to introduce the universal scaling using known systems from text books, e.g. the ferro magnet, as it is done in section 4.1. In section 4.2 the vocabulary and the grammar found must be translated to the physics of the Rydberg excitation.

4.1. Basic concept of critical phenomena

Text books like reference [Hua87] introduce the universal scaling as a critical phenomenon, which can be found for example near the critical point of a second order phase transition. At this critical point two things happen. Firstly, the symmetry of the system will change when crossing the critical point and secondly, one can assume that at the critical point only one characteristic 'length scale' ξ exists and that all observables depend on this length scale with some critical exponent.

The first point can be understood in terms of a magnet near the Curie temperature T_C, with a phase diagram depicted in figure 4.1 . If $T > T_\mathrm{C}$ the system is completely demagnetised and, thus, rotational symmetric. Lowering the temperature below the Curie temperature causes the solid to magnetise, due to which the system loses symmetry. The description of the system if $T < T_\mathrm{C}$ requires an additional parameter M called the 'order parameter', which is in the case of a magnet just the magnetisation.

In the region near the critical point the order parameter is assumed to be the only important property of the system. One of the major tasks is usually to identify this order parameter and its 'conjugate field', which in the case of the magnet is the external magnetic field H. Near but below the critical

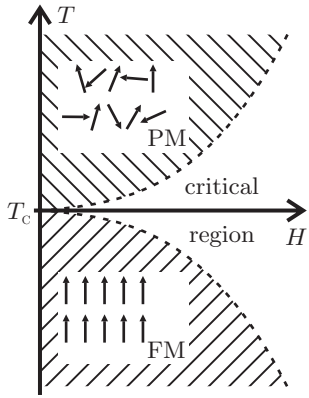

Figure 4.1.: Schematic of the phase diagram of a ferromagnet around the Curie temperature T_C. For $T > T_C$ the system is in the paramagnetic phase PM. If $T < T_C$ the system is magnetised even without external field H, i.e. the system is in the ferromagnetic phase FM.

temperature M is fully described by a proportionality to a power of H and to another power of a dimensionless parameter t. These powers of H and t are called the critical exponents and are generally fractional numbers. In case of a magnet $t = {}^{T}/_{T_C} - 1$ and the critical point is reached for $t \to 0$. Another characteristic at a critical point and, thus, for the appearance of a universal scaling, is that the length scale $\xi \sim {}^{1}/_{t^{\nu}}$, with $\nu > 0$, is diverging.

The critical exponents are of special interest because they are universal through out many different systems, at least if these systems fall in the same universality class [Fis98]. A list of experimentally obtained values for the critical exponents in the ferromagnetic system can be found in table 16.2 of reference [Hua87] in comparison to the theoretically expected exponents.

Another experimental example was given in [Gug45] showing the universality of the critical exponents in a different system. Guggenheim investigated the behaviour of the reduced density ${}^{n}/_{n_c}$ dependent on the reduced temperature ${}^{T}/_{T_c}$ near the gas-liquid critical point for noble gases and some different molecules. He showed by this that the dependence of the reduced density behaves according to a universal scaling with a power law of the reduced temperature for all investigated systems, independent of their exact atomic composition.

4.2. Translation into the Rydberg system

The description of the critical exponents and their universality given above on the example of a magnet needs now to be translated into the Rydberg system, which is done in [Wei08]. Given the Hamiltonian in the basis $|\mathrm{g}\rangle = (0, 1)^{\mathrm{t}}$ and

$|\mathrm{r}\rangle = (1,0)^{\mathrm{t}}$

$$\mathcal{H} = -\frac{\hbar\delta}{2}\sum_i \boldsymbol{\sigma}_z^{(i)} + \frac{\hbar\Omega}{2}\sum_i \boldsymbol{\sigma}_x^{(i)} + C_6 \sum_{j<i} \frac{\mathcal{P}_{\mathrm{rr}}^{(i)}\mathcal{P}_{\mathrm{rr}}^{(j)}}{|\boldsymbol{r}_i - \boldsymbol{r}_j|^6}\,, \tag{4.1}$$

where $\boldsymbol{\sigma}^{(i)}$ are the Pauli matrices, $\boldsymbol{r}_i$ are the positions of the atoms and $\mathcal{P}_{\mathrm{rr}}^{(i)} = |\mathrm{r}\rangle_i \langle \mathrm{r}|_i = (\mathbb{1} + \boldsymbol{\sigma}_z^{(i)})/2$ is the projector onto the excited Rydberg state. The two-photon detuning is given by δ (see figure 4.2).

The order parameter is simply the Rydberg fraction

$$f \equiv \left\langle \mathcal{P}_{\mathrm{rr}}^{(i)} \right\rangle = \frac{N_{\mathrm{R}}}{N_{\mathrm{g}}}\,, \tag{4.2}$$

with N_{R} being the Rydberg atom number and N_{g} the number of atoms in the ground state. The diverging correlation length ξ is given by the ratio of the distance a_{R} between the Rydberg atoms and a_{g} the distance between the atoms in the ground state

$$\xi \equiv \frac{a_{\mathrm{R}}}{a_{\mathrm{g}}} = \frac{1}{a_{\mathrm{g}}}\sqrt[6]{\frac{C_6}{\hbar\Omega_N}}\,, \tag{4.3}$$

where the blockade condition according to equation (3.19) was used.

The missing part to describe the universal scaling of f near the critical point is the 'conjugate field', which is given by the dimensionless parameter α comparing the coupling strength with the interaction energy

$$\alpha \equiv \frac{\hbar\Omega_0}{C_p n_{\mathrm{g}}^{\beta}}\,. \tag{4.4}$$

The second order phase transition happens for $\alpha \ll 1$ between the phase where all atoms are in the ground state ('paramagnetic phase') and the phase where the Rydberg atoms arrange themself in the crystalline structure depicted in figure 3.3. Figure 4.2 shows the phase diagram in the Δ-α plane with $\Delta = {}^{\hbar\delta}/_{C_p n_{\mathrm{g}}^{\beta}}$, where δ is the two-photon detuning, n_{g} the atomic density in the ground state. The exponent $\beta = {}^{p}/_{d}$ is given by the dimensionality d of the system and the exponent p of the r-dependence of the interaction, i.e. $\mathcal{V} \sim r^{-p}$. The energy scale Δ is the equivalent to the dimensionless parameter t in section 4.1.

The correlation length ξ can be written with equation (4.3) in terms of the Rydberg fraction f according to

$$\xi \sim \left(\frac{n_{\mathrm{g}}}{n_{\mathrm{R}}}\right)^{1/d} \sim \frac{1}{f^{1/d}}\,. \tag{4.5}$$

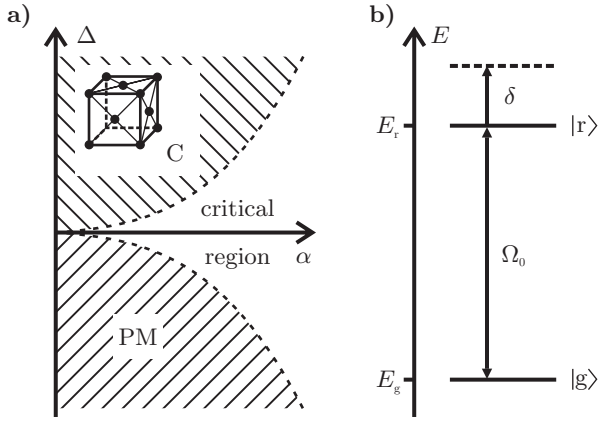

Figure 4.2.: **a)** Illustration of the second order phase transition in a driven Rydberg system in the Δ-α plane. The 'paramagnetic phase' PM corresponds for $\Omega_0 = 0$ to $f = 0$, i.e. no Rydberg atom excited. The crystalline phase C corresponds to the arrangement of the maximum number of Rydberg atoms, which is a face centred cubic lattice in the case of three dimensions and van der Waals interaction. The exponents for the scaling of f are universal in the critical region between these two phases, where the scaling is expected to be universal. **b)** Energy level diagram to clarify the symbols used in the text and in equation (4.1): δ is the two-photon detuning and Ω the coupling strength between the ground state $|\mathrm{g}\rangle$ and the Rydberg state $|\mathrm{r}\rangle$.

Since ξ diverges for $f \to 0$, it is expected, as pointed out in section 4.1, to find a universal scaling for $\Delta = 0$. In other words, for $\Delta = 0$ the system is independent of the exact microscopic realisation as the characteristic length scale ξ diverges.
Similar to the ideas introduced in the previous section one finds that the order parameter f near the critical point fully characterised by Δ and α. The dependence of f on these parameters is given by

$$f \sim \Delta^{\kappa}\,, \tag{4.6}$$

and the equation of state for $\Delta = 0$

$$f \sim \alpha^{\nu}\,, \tag{4.7}$$

with the universal scaling exponents κ and ν in the critical region, i.e. $\alpha \ll 1$ and $\Delta \ll 1$.

The derived equations will be used in section 8.1 to find equations describing the initial slope R and the saturation value N_{sat} of the Rydberg excitation curve depicted in figure 3.5.

Part III.

Experimental pillars

5. Cooling and trapping neutral atoms

A setup for experiments with frozen Rydberg gases consists of hundreds of parts including lasers, electronics, opto-mechanics, opto-electronics and vacuum parts. This chapter covers the basics of cooling and trapping of neutral atoms by means of laser cooling, evaporative cooling and trapping of the atoms in magnetic and optical traps as well as their detection. The setup will be introduced briefly in section 5.1. Only the points required for this thesis are pronounced as the setup was already described extensively in [Löw06, Löw07, Kro04]. Section 5.2 introduces the basics of the laser cooling technique, which is the first step towards the creation of an dense ultracold atomic sample. The sections 5.3 and 5.4 introduce two different techniques to trap neutral atoms, namely the magnetic trap and the optical dipole trap.

5.1. The setup

Working with ultracold atoms requires the use various techniques. First, it is necessary to isolate the atoms from the thermal environment. This is done by setting up ultrahigh vacuum chambers with pressures below 10^{-11} mbar. At these low pressures the collisional rate between atoms and the background gas is $< {}^{1}/_{\mathrm{min}}$. We use in our setup a $200\,{}^{\mathrm{l}}/_{\mathrm{s}}$ ion pump and a titanium sublimation pump with a cryogenic shield to evacuate the main chamber to the desired pressure.

The second requirement is a source of precooled atoms, which can be further cooled down and trapped. In the oven part (see figure 5.2) a piece of rubidium in natural abundance (28 % ^{87}Rb, 72 % ^{85}Rb) is heated to a temperature of 160 K. For the initial cooling step we chose an increasing field Zeeman slower from the diversity of different cold atom sources [Phi82, Rii90, Lu96, Ber98] to cool ^{87}Rb atoms from initial temperature to the few Kelvin regime. The effusive gas jet is spatially filtered by apertures and passes a cooling shield. Afterwards, the collimated atom beam passes the differential pumping tube, which separates the high vacuum part from the ultrahigh vacuum part, and enters the Zeeman slower. The principle of the Zeeman slower is based on laser cooling by spontaneous scattering of photons as it will be discussed in section 5.2 with the addition that the decreasing Doppler shift due to the decreasing velocity of the atoms is compensated by the Zeeman shift induced by an increasing magnetic field [Löw06, Kro04]. The atoms reach the centre

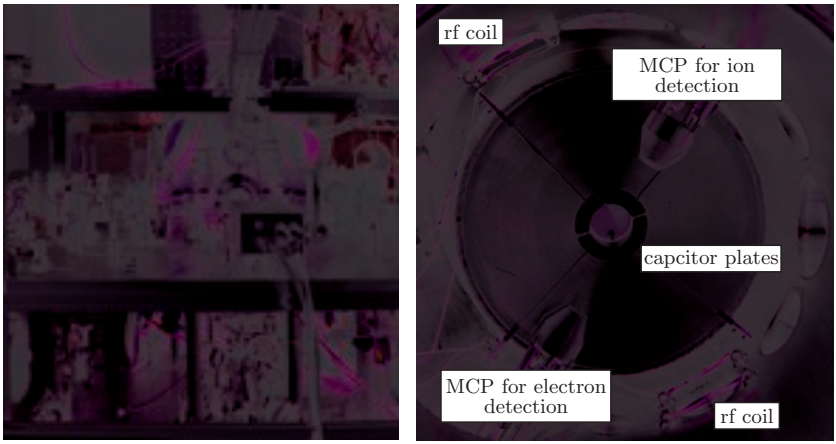

Figure 5.1.: Left: Current picture of the setup. Right: Inside of the main chamber with the radio-frequency coils, two multichannel plates (MCPs) and four of the eight capacitor plates around the centre of the chamber. Considering the coordinate system in figure 5.2 the view is along the z-direction.

of the main chamber with a velocity on the order of $10\,{}^{\mathrm{m}}/_{\mathrm{s}}$, where they are further laser cooled and loaded into a conservative magnetic trapping potential as discussed in section 5.3.

A picture of the current setup and from the inside of the main chamber is shown in 5.1. This picture shows the radio-frequency (rf) coils for evaporative cooling, the multichannel plates (MCPs) for detection of ions and electrons, respectively, and four of eight capacitor plates. The capacitor plates are placed around the centre of the main chamber and allow the application of electric fields over the trapped atomic sample. The segmentation of the capacitor enables us to apply nearly arbitrary electric fields over the atomic cloud and to guide the electrically charged particles towards the MCPs for detection as described in section 7.2.

Additionally to the magnetic trap the setup is build such, that an optical lattice in three dimension can be realised. In this thesis I will present experiments which were done in an optical dipole trap described in section 5.4.

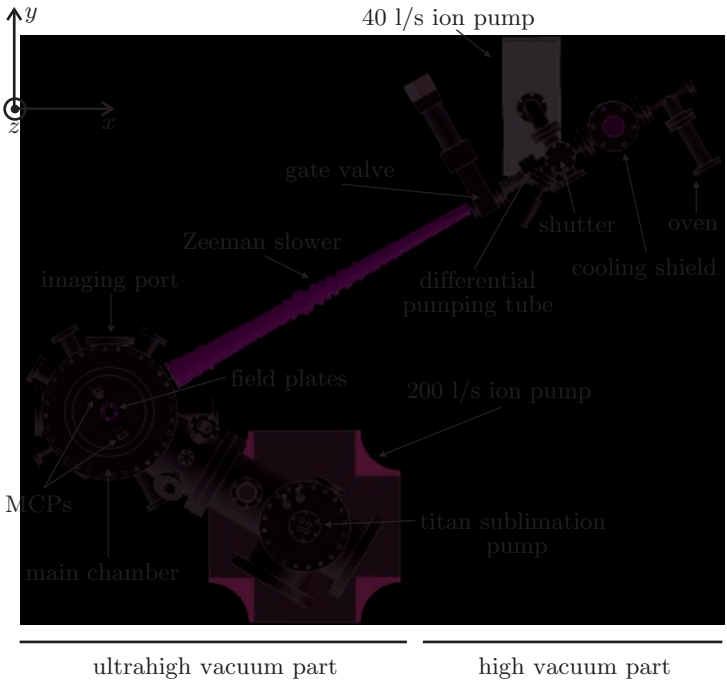

Figure 5.2.: The experimental setup splits into two parts. The oven part in the upper right corner is under high vacuum with typical pressures of 10^{-7} mbar. This part basically consist of a tubing containing 5 g of rubidium, a nozzle and a cooling shield to produce a collimated atom beam and a shutter to switch this beam on and off. The oven part can be separated from the main chamber by a valve and is pumped with a 40 l/s ion pump. The ultrahigh vacuum part, situated in the lower left corner of the picture, consist mainly of the main chamber which is pumped by a 200 l/s ion pump and a titanium sublimation pump. It is connected to the oven part via the Zeeman slower and a differential pumping tube. The design of the main chamber is based on the second generation cloverleaf trap experiments built at the M.I.T. [Str06]. Our setup additionally contains eight capacitor plates in the centre of the chamber (see figure 5.1 for details) and two multichannel plates in order to manipulate and detect Rydberg atoms. The coordinate system in the upper left corner will be used throughout this thesis to identify the direction of the quantisation axis and laser beams.

5.2. Laser cooling

Laser cooling of atoms is based on the spontaneous scattering of photons or, to be more precise, it is based on a statistical redistribution of photons from the laser mode with a frequency of ω_l and a wave vector k_l into other modes $\{k_\mu, \omega_\mu\}$. The scattering rate is $\Gamma_\mathrm{s} = \Gamma\varsigma'_\mathrm{ee}$ with the steady state solution of the Linblad equation of the two-level atom given by equation (1.15) and the natural linewidth Γ. By scattering a photon from the laser mode the atom experiences a force $F = \hbar k_\mathrm{l}\Gamma\varsigma'_\mathrm{ee}$. Linearising the force of two counter propagating lasers around $v = 0$ leads to [Met99]

$$F \approx -\beta v\,, \tag{5.1}$$

with

$$\beta = -\frac{4\hbar k_\mathrm{l}^2 \delta s_0}{\Gamma(1 + s_0 + (\frac{2\delta}{\Gamma})^2)^2}\,, \tag{5.2}$$

and the on-resonance saturation parameter given by equation (1.18) $s_0 \equiv {}^{I}/_{I_\mathrm{sat}} = {}^{2\Omega^2}/_{\Gamma^2}$.

Thus, the motion of the atoms is damped towards $v = 0$ if $\delta < 0$. Due to the emission of the photon the atom experiences a second momentum transfer, which is statistically distributed and adds to zero when averaging over the time. On the other hand this impulse leads to a random walk in the momentum space, which results in a lowest possible temperature of $T_\mathrm{D} = {}^{\hbar\Gamma}/_{(2k_\mathrm{B})}$ for the described Doppler cooling.

Temperatures below T_D are possible with multilevel atoms using techniques like the polarisation gradient cooling, where the lowest temperature is given by the recoil energy one photon transfers to the atom. Even lower temperatures than this recoil limit are possible using velocity-selective dark states or Raman transitions. These techniques are described extensively in textbooks like [Met99, Mey01].

A magnetic field gradient can be used to trap the atoms as it causes, due to the Zeeman shift, an additional position depending detuning $\delta_\mathrm{Z} = {}^{\mu}/_{\hbar} \cdot \nabla B \cdot z$. This leads to a resulting force

$$F = -\beta v - \kappa r\,, \tag{5.3}$$

with β from equation (5.2) and

$$\kappa = \frac{\mu_\mathrm{eff}\nabla B}{\hbar k}\beta\,, \tag{5.4}$$

where $\mu_\mathrm{eff} = (g_\mathrm{e}m_\mathrm{e} - g_\mathrm{g}m_\mathrm{g})$ is the effective magnetic moment for the transition.

Applying this force in all three spatial directions leads to a cooling and confinement of the atoms. This setup is referred to as the magneto-optical trap (MOT), which constitutes usually the first atom trap in cold atom experiments.

The light for the laser cooling is provided by the laser setup shown in figure 5.3. The main light source is a Nd:YAG[1] laser which pumps a titanium sapphire laser[2] (Ti:Sa). This laser provides the light for the cooling and trapping for the Zeeman slower and the MOT. It is additionally used to spin polarise the atoms into the $5S_{1/2}(f = 2, m_f = 2)$ state, which is magnetically trapped (see section 5.3) and, finally, to image the atoms.

Additionally a diode laser system is used to repump atoms which are accidentally transferred into the $5P_{3/2}(f = 2)$ state back into the cooling cycle. This is necessary since atoms in the state $5P_{3/2}(f = 2)$ decay with a probability of 50 % into the $5S_{1/2}(f = 1)$ state, which does not couple to the $5S_{1/2}(f = 2)$ to $5P_{3/2}(f = 3)$ cooling transition and, thus, the atoms are lost.

[1] Verdi V-10, Coherent
[2] MBR E-110, Coherent

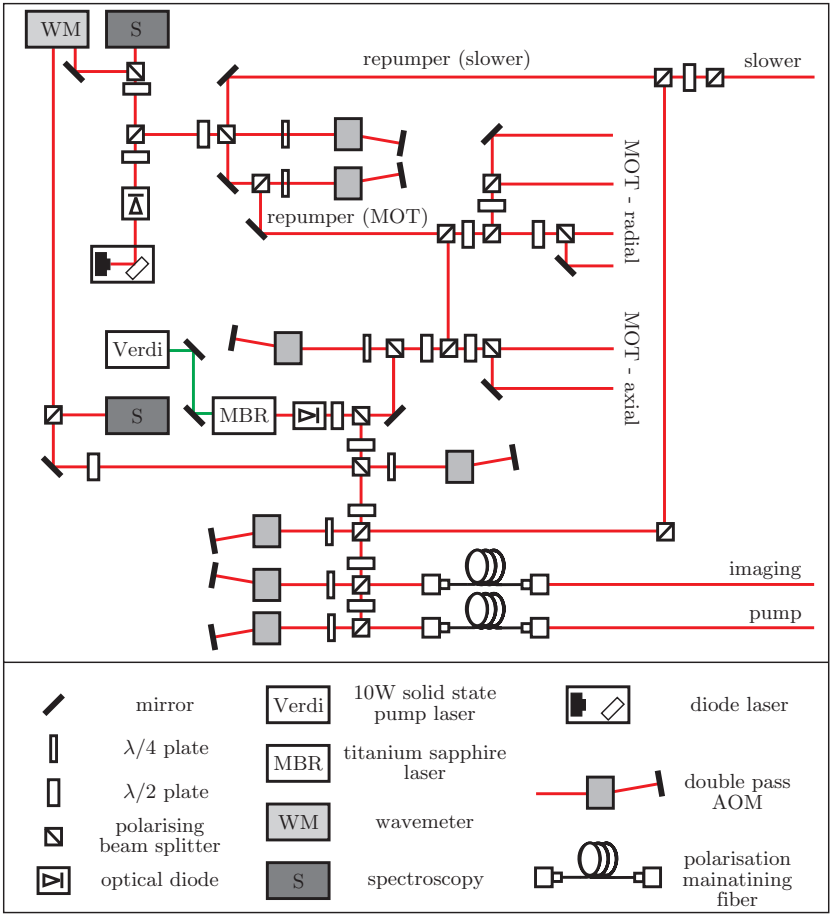

Figure 5.3.: Scheme of the laser setup. The main laser is a titanium sapphire (Ti:Sa, denoted MBR) laser pumped by a Nd:YAG laser (Verdi). The light from the Ti:Sa is used for trapping, cooling and imaging the atoms as well as pumping them into the magnetically trapped state. Additionally a diode laser system denoted as 'repumper' is used to pump the atoms from the lower hyperfine level of ^{87}Rb back into the cooling cycle.

5.3. The magnetic trap

The temperature limit for optical cooling, beside the special techniques mentioned in section 5.2, is given by the recoil energy of a photon $T_\mathrm{r} = {(\hbar k)^2}/{(2k_\mathrm{B}m)}$. In the case of ^{87}Rb cooling transition this corresponds to a temperature of 180 nK. Even so T_r is on the order of the temperature of the phase transition from a thermal cloud to a Bose-Einstein condensate (BEC) it is lacking a high atomic density, since the sub-Doppler cooling methods require a low atomic density to avoid multiple photon scattering. Hence, the phase space density $\mathbb{p} \sim n\,T^{-3/2}$ cannot be increased to the value of 2.6, where quantum degeneracy is reached [Foo05], using this methods.

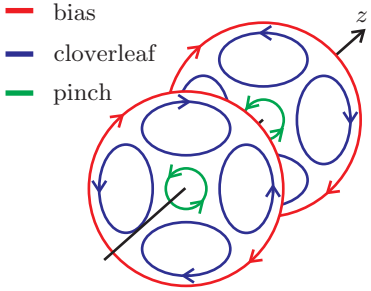

Figure 5.4.: A cloverleaf type magnetic trap consisting of two wheels each containing six coils. The cloverleaf coils generate, if they are connected as it is shown, a three dimensional quadrupole with zero magnetic field on the z-axis. The pinch coils generate a curvature along the z-axis. The bias coils subtract the magnetic field offset caused by the pinch coils.

High phase space densities can be achieved by the evaporative cooling technique. Two approaches have been successfully demonstrated over the last years. The first is the evaporative cooling of magnetically trapped atoms by transferring the hot atoms in magnetically untrapped states. The second approach is to store the atoms in an optical dipole trap discussed in section 5.4 and lower the intensity of the dipole trap beam.

5.3.1. The potential

In our setup we use a cloverleaf type magnetic trap [Str06] to trap the atoms after the MOT and molasses phase. This trap type produces magnetic field that is similar to that of a Ioffe-Pritchard trap, with the advantage of a better optical access and a finite radial height of the potential, which prevents the formation of an Oort cloud [Die01]. The magnetic field of a Ioffe-Pritchard or cloverleaf trap can be approximated by

$$\boldsymbol{B}(\boldsymbol{r}) = B_0 \begin{pmatrix} 0 \\ 0 \\ 1 \end{pmatrix} + B' \begin{pmatrix} x \\ -y \\ 0 \end{pmatrix} + \frac{B''}{2} \begin{pmatrix} -xz \\ -yz \\ z^2 - \frac{1}{2}(x^2+y^2) \end{pmatrix} . \quad (5.5)$$

The potential energy $U(\boldsymbol{r}) = \mu B$, with the magnetic moment $\mu = g_f m_f \mu_\mathrm{B}$, can be expanded around $\boldsymbol{r} = 0$. Neglecting all powers larger than two and using the cylinder coordinates $r = \sqrt{x^2 + y^2}$ and z results in the harmonic approximation for the trap potential

$$U(r,z) = \frac{1}{2} m\omega_r^2 r^2 + \frac{1}{2} m\omega_z^2 z^2 \,, \tag{5.6}$$

with

$$\begin{aligned} \omega_r &= \sqrt{\frac{g_f m_f \mu_\mathrm{B}}{m} \left(\frac{B'^2}{B_0} - \frac{B''}{2} \right)} \,, \\ \omega_z &= \sqrt{\frac{g_f m_f \mu_\mathrm{B}}{m} B''} \,. \end{aligned} \tag{5.7}$$

In a harmonic trap the density distribution for a thermal cloud is of Gaussian shape

$$n(r,z) = n_0 \, \mathrm{e}^{-U(r,z)/k_\mathrm{B}T} = n_0 \mathrm{e}^{-r^2/2\sigma_r^2 - z^2/2\sigma_z^2} = n_0 \tilde{n}(r,z) \quad , \tag{5.8}$$

with the width ($1/\sqrt{\mathrm{e}}$-radius) of the cloud

$$\sigma_i = \frac{1}{\omega_i} \sqrt{\frac{k_\mathrm{B}T}{m}} \,, \tag{5.9}$$

and the atomic peak density

$$n_0 = \frac{N_0}{(2\pi)^{3/2} \, \sigma_r^2 \, \sigma_z} \,. \tag{5.10}$$

The atomic sample is confined radially by the magnetic field gradient B' and the offset field $B_0 > 0$. A negative magnetic offset would result in an over compensation of the magnetic trap and a loss of atoms along a potential surface where the potential is zero. The confinement in axial direction is given by the curvature B'' of the magnetic field. Our trap parameters are $B' = 6 \times 10^{-3} \, I_\mathrm{CL} \, \mathrm{T/Am}$, $B'' = 0.6 \, I_\mathrm{PB} \, \mathrm{T/Am^2}$ and $B_0 \simeq 10^{-4} \, \mathrm{T}$, where I_CL and I_PB is the current through the cloverleaf and pinch-bias coils, respectively (see figures 5.4 and 5.5 for details). Typical values for different temperatures T and atom numbers N_0 of an atomic sample are shown in table 5.1. The temperature of the atomic cloud is obtained by a series of time of flight measurements (see section 7.1).

Since the experiments discussed in this thesis are conducted at very low temperatures (<10 µK) of the atomic sample the harmonic approximation is justified. For temperatures above ≃60 µK the atoms would reach regions of

	hot sample	cold sample	BEC
temperature	550 µK	4 µK	600 nK
axial size	2 mm	160 µm	40 µm
radial size	340 µm	10 µm	2 µm
atom number	3×10^9	1×10^7	1×10^5
atomic peak density	$8 \times 10^{17}\,\mathrm{m}^{-3}$	$4 \times 10^{19}\,\mathrm{m}^{-3}$	$2 \times 10^{20}\,\mathrm{m}^{-3}$
de Broglie wavelength	10 nm	110 nm	300 nm
phase space density	7×10^{-7}	0.05	5

Table 5.1.: Typical values of magnetically trapped atoms in our setup. The values for the 'hot sample' column take the linear behaviour of the trap potential into account (see reference [Kro04] for details). The trap potential for the 'cold sample' is harmonic. For comparison the corresponding values for a Bose-Einstein condensate (BEC) are shown (used relation can be found in [Pet02]).

the trapping potential that are rather linear than quadratic and the density distribution would change.
A typical sequence for producing ultracold atomic clouds starts with loading a MOT for 4 s after which a molasses cooling step follows. For this the cooling lasers are detuned by $2\pi \times 78$ MHz and the magnetic field gradient is switched off. The atom cloud is loaded into the magnetic trap by switching on the currents within 1 ms to the values $I_{\mathrm{CL}} = 200$ A, $I_{\mathrm{PB}} = 50$ A, $I_{\mathrm{P}} = 75$ A and $I_{\mathrm{o}} = 0$ A (see the figures 5.4 and 5.5 for details). This creates a very shallow potential matching the density distribution of the MOT as good as possible without loosing to much atoms. A σ^+ polarised laser resonant to the $5\mathrm{S}_{1/2}(f = 2)$ to $5\mathrm{P}_{3/2}(f = 3)$ transition pumps the atoms to the $5\mathrm{S}_{1/2}(f = 2, m_f = 2)$ state.

After the atoms are caught in the magnetic trap every light is switched off and the currents are ramped within 600 ms to their final values of $I_{\mathrm{CL}} = 400$ A, $I_{\mathrm{PB}} = 400$ A, $I_{\mathrm{P}} = 0$ A and $I_{\mathrm{o}} = 6.5$ A. The radial gradient of the magnetic trap is $B' = 2.4\,\mathrm{T/m}$ and the curvature in axial direction is $B' = 240\,\mathrm{T/m^2}$.

Due to the compression of the atomic cloud the atomic peak density increases roughly by a factor of 100, while the temperature increases from $\simeq$30 µK after the molasses to $\simeq$550 µK and the phase space density increases by a factor of $\mathrm{e} \simeq 2.7$ if the compression happens adiabatically and no atoms are lost [Pin97].

In order to increase the atomic density and the phase space density further the temperature must be lowered. In our experiment this is done via forced

evaporative cooling with radio frequency (rf) radiation applied on the Zeeman sublevels of the $5S_{1/2}(f = 2)$ state at a frequency of $0 \leq \nu_{\mathrm{rf}} \leq 42\,\mathrm{MHz}$. Atoms with an energy of $E_{\mathrm{rf}}(t) \geq \eta(t) k_{\mathrm{B}} T$, with $\eta \simeq 10$, cross the resonant region and are pumped to the untrapped $5S_{1/2}(f = 2, m_f = 0)$ state. This removes the velocity classes with the kinetic energy $E_{\mathrm{k}} \geq h\nu_{\mathrm{rf}}$ from the trap. In other words the initial Maxwell distributed velocity is truncated at $v \geq v_{\mathrm{rf}}$. Provided that the number of elastic collisions exceed the number of inelastic collisions, the atomic cloud thermalises after which the velocity is again Maxwell distributed, but now with a lower temperature.

The setup for the evaporative cooling consist of two coils in Helmholtz configuration opposing each other inside the main chamber (see figure 5.1) a 42 MHz homemade synthesiser and a 15 W[3] rf amplifier. We need $\simeq$ 35 s from beginning of the evaporative cooling until the atomic sample reaches quantum degeneracy (see figure 5.4 and 7.2).

5.3.2. Current control

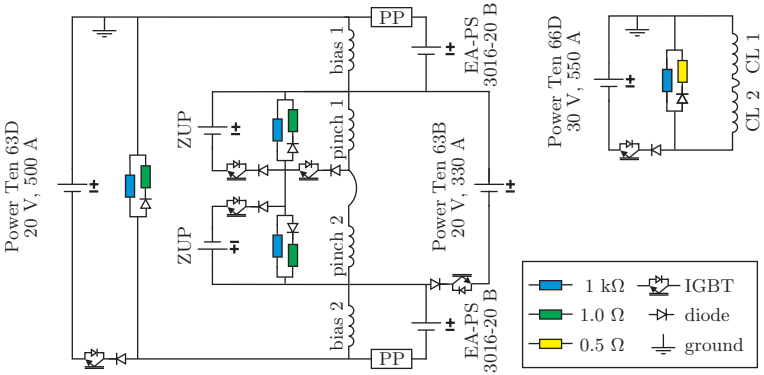

Figure 5.5.: Electric setup for the magnetic trap. CL denote the cloverleaf coils and bias the offset coils. Additional power supplies connected to the offset coils give the ability to fine tune the offset of the magnetic field over the atomic sample. The symbol PP denotes a push-pull switch for fast switching of small currents (see figure C.1). The power supplies denoted ZUP (ZUP6-33, Lambda Americas, Inc.) are solely connected to the pinch coils and used to produce the magnetic field gradient used for the MOT.

[3] AP001220-10, RFPA

Figure 5.5 shows the electric circuit for the currents used for the magnetic trapping. Since the magnetic moment of rubidium is μ_B in the ground state at maximum, rather high currents are needed in a cloverleaf magnetic trap to obtain sufficient trap depths. Fast switching of these currents require resilient switches and ring down circuits, which make sure that after the switch has been opened the energy in the magnetic field is dissipated as quick as possible. For the switching of the high currents we use insulated-gate bipolar transistors (IGBTs)[4]. Additionally we use diodes[5] to protect the power supplies and the IGBTs. The IGBTs and diodes for the currents through the pinch-bias circuits and the cloverleaf circuit are mounted on a commercial cooling board[6] to avoid damage of the devices due to insufficient cooling.

In order to fine tune the magnetic field offset we use two power supplies parallel to the bias coils. The rather low current I_o of these additional power supplies are switched using a push-pull circuit shown in figure C.1.

5.3.3. Landau-Zener sweep

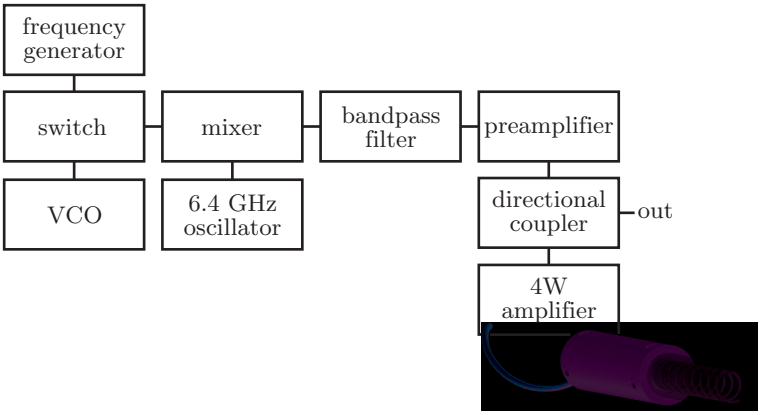

Figure 5.6.: Schematic of the setup to drive the $5S_{1/2}(f = 2, m_f = 2)$ to $5S_{1/2}(f = 1, m_f = 1)$ of ^{87}Rb via microwave radiation. This transition can for example be used to apply a Landau-Zener sweep to the atomic sample. A detailed description of the used devices can be found in [Löw06].

[4] e.g. FZ800R16KF4, Eupec for the switching of 400 A
[5] e.g. DD800S17K6C_B2, Eupec
[6] AKW/KS 137-535, DAU GmbH

In order to study interaction effects among the atoms one must be able to tune the interaction between the atoms. Since we are using Rydberg atoms, which interact through the van der Waals interaction $\mathcal{V}_{\mathrm{vdW}} \sim C_6 n_{\mathrm{g}}^2$ it is possible to tune the interaction strength by changing the atomic ground state density n_{g}. A particular useful tool to change the atomic density is the Landau-Zener sweep [Lan32, Zen32]. The theory behind is again a two-level system like the one introduced in section 1.1. Microwave radiation with a frequency of 6.834 GHz couples the two hyperfine states of ^{87}Rb on the $5\mathrm{S}_{1/2}(f = 2, m_f = 2)$ to $5\mathrm{S}_{1/2}(f = 1, m_f = 1)$ transition. Since the $5\mathrm{S}_{1/2}(f = 1, m_f = 1)$ state is not magnetically trapped the atoms can escape the trap volume.

The used setup is shown in figure 5.6. Since this transition is forbidden for electrical dipole radiation a magnetic dipole transition is used. The microwave radiation is circularly polarised due to the helical realisation of the antenna. The helical design of the antenna results in a forward gain of the radiation in the direction of propagation [Ben06]. The used devices for this setup are listed in reference [Löw06], which shows also the coherent coupling of two hyperfine manifolds using the microwave transition. Here I will focus on the usage of 6.8 GHz source to lower the density of magnetically trapped atoms, as this application will be essential in the experiments discussed in part IV.

The probability for a transition of the atom from the initial state $5\mathrm{S}_{1/2}(f = 2, m_f = 2)$ to $5\mathrm{S}_{1/2}(f = 1, m_f = 1)$ is given by [Rub81]

$$P_{21} = \exp\left(-\frac{2\pi}{\hbar} \cdot \frac{|\mathcal{V}_{12}|^2}{\mathrm{d}E/\mathrm{d}t}\right) . \tag{5.11}$$

The matrix element $\mathcal{V}_{12}$ connects the two states and is responsible for the lifting of the degeneracy. The energy derivation $\mathrm{d}E/\mathrm{d}t = (\mathrm{d}E/\mathrm{d}B)(\mathrm{d}B/\mathrm{d}t)$ is called slew rate and reflects the behaviour of the transition around the avoided crossing. The slope of the crossing $\mathrm{d}E/\mathrm{d}B$ and the rate $\mathrm{d}B/\mathrm{d}t$ at which the magnetic field of the microwave radiation is changed determines the efficiency of the Landau-Zener sweep.

Figure 5.7 shows exemplarily data taken for the density variation to measure the interaction dependence of the rotary echo experiment in a magnetic trap presented in section 9.1. The atomic peak density of ground state atoms is shown as a function of the time τ_{LZ} for which the Landau-Zener sweep was applied to the atomic sample. The rate $\mathrm{d}B/\mathrm{d}t$ is chosen such that the temperature of the atomic cloud is not changed by the Landau-Zener sweep. Hence, the spacial density distribution $\tilde{n}(r, z)$ (see equation (5.8)) is constant while its peak value n_0 is lowered for increasing Landau-Zener sweep times.

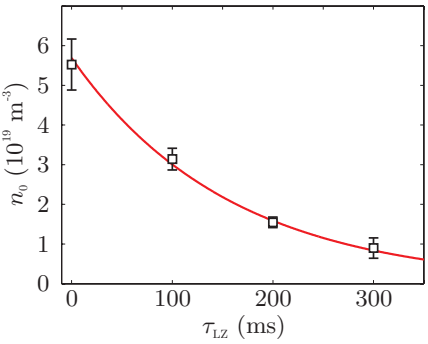

Figure 5.7.: Atomic ground state density n_g as a function of the Landau-Zener sweep pulse duration τ_{LZ}. The red curve is an exponential decay fitted to the data points.

5.4. The optical dipole trap

Optical dipole traps (ODTs) have a couple of advantages over the magnetic trap. With optical switches like AOMs, EOMs or liquid crystal cells it is possible to switch light on and off very fast. In comparison switching of electrical currents is technically challenging due to the finite inductance of wires and coils and perturbing eddy currents in copper gaskets used for the sealing of the vacuum chamber. Another advantage is the freedom to apply a homogenous magnetic field over the atomic cloud with an arbitrary direction. Furthermore, it is possible to shape the geometry of the cloud in a wide range using optical potentials.

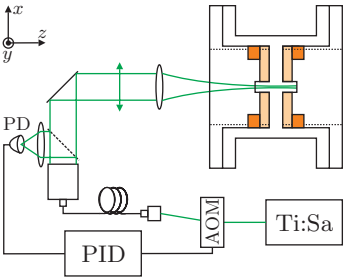

Figure 5.8.: Schematic of the intensity stabilisation of the dipole trap. A photo diode (PD) monitors the power of the fibre coupler from a polarisation maintaining fibre using a low reflective beam splitter. The signal is looped back via a PID controller to an acoustic-optical modulator in front of the fibre.

The simplest geometry forming an optical dipole trap is just a single beam superimposed to the atomic cloud. The major disadvantage of optical dipole traps is the, in comparison the the magnetic trap, shallow potential and, thus, a smaller trap volume. The trap potential is given by equation (1.23) with the

Rabi frequency from equation (1.24)

$$U_{\mathrm{d}} = \frac{\hbar\Omega^2}{4\delta} \sim \frac{I}{\delta}\,, \tag{5.12}$$

for large detunings $\delta \gg \Omega$ of the laser forming the ODT to the atomic transition. The scattering rate is given by equation (1.26)

$$\Gamma_{\mathrm{s}} = \frac{3\pi c^2}{2\hbar\omega^3}\left(\frac{\Gamma}{\delta}\right)^2 I \sim \frac{I}{\delta^2}\,. \tag{5.13}$$

Thus, it is preferable to use strong laser with a large detuning from the atomic transition.

A payoff for a sufficient deep potential between intensity and detuning must be found by calculating the potential of the ODT. Since real atoms have more than two states the potential of the ODT couples to all states with their respective detuning δ_{ba} and coupling strength Ω_{ba}. Figure 5.9 shows the strongest transitions of ^{87}Rb to which a far red detuned laser couples in first order. Usually, the detuning of an ODT from any atomic transition is large so that one can use equation (5.12) in good approximation.

For the calculation of the potential of the ODT in this thesis only the closest transitions to the wavelength of the ODT beam were used, namely the D1 and D2 line in ^{87}Rb as depicted in figure 5.9. All other transition would give corrections on the order of $< 10^{-3}$ to the calculated value. A MatLab program for calculating the ac-Stark shift is given in appendix A.2. Using the setup depicted in figure 5.8 we stabilise the power of the ODT to $P = 22\,\mathrm{mW}$. The beam is focused to a waist ($1/e^2$-radius) of $w_0 = 22\,\mu\mathrm{m}$ and has a wavelength of $\lambda = 826\,\mathrm{nm}$, provided by a titanium sapphire laser[7]. The polarisation of the beam is linear along the x-direction. Thus, regarding the quantisation axis of the atoms the beam couples either with π-light or with the decomposition of the π-light into σ^+- and σ^--light to the atoms (see figure 5.9 and chapter B). The transformation matrices from the coordinate system of the ODT beam to the atomic coordinate system is given in appendix B. Finally, the resulting potential depth is $U_0 = 3.3\times10^{-28}\,\mathrm{J} \mathrel{\widehat{=}} 24\,\mu\mathrm{K}$. This trapping potential is ramped up in 50 ms directly after evaporatively cooling the atoms in the magnetic trap. Afterwards, the magnetic trap is switched off within 20 ms and the atomic cloud is kept for another 100 ms for thermalisation.

The trapping potential can be approximated by a parabolic function, which leads to the density distribution in the trap analogue to equation (5.10)

$$n(r,z) = n_0\, \mathrm{e}^{-r^2/2\sigma_r^2 - z^2/2\sigma_z^2}\,, \tag{5.14}$$

[7] MBR E-110, Microlase Optical System

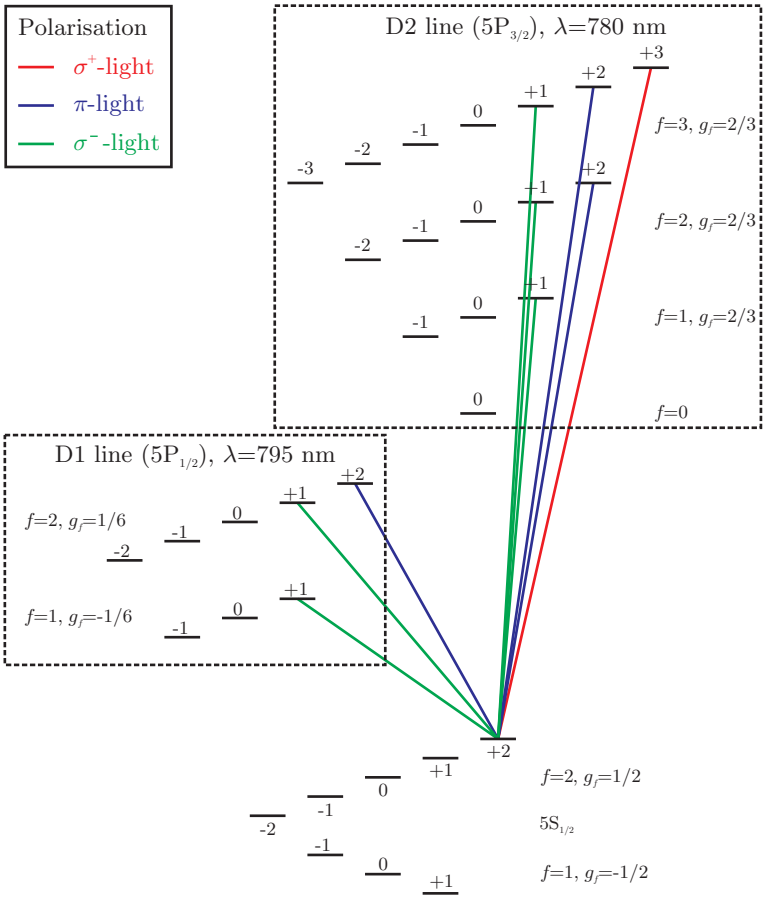

Figure 5.9.: D1 and D2 line of ^{87}Rb. The coloured lines indicate the transitions for different light polarisations used for the calculation of the trap potential of an optical dipole trap. The D1 line has a decay rate of $\Gamma_{D1} = 2\pi \times 5.75\,\mathrm{MHz}$ and the D2 has a decay rate of $\Gamma_{D2} = 2\pi \times 6.07\,\mathrm{MHz}$ [Ste01]. A MatLab program in appendix A.1 can be used to calculate the line strengths of the transitions. The program in appendix A.2 can be used to calculate the light shift due to the ODT.

with the Gaussian widths [Gri00]

$$\begin{aligned} \sigma_r &= \sqrt{\frac{k_\mathrm{B} T w_0^2}{4U_0}}\,, \\ \sigma_z &= \sqrt{\frac{k_\mathrm{B} T z_\mathrm{R}^2}{2U_0}}\,. \end{aligned} \tag{5.15}$$

The Rayleigh range z_R of the Gaussian beam is given by

$$z_\mathrm{R} = \frac{\pi w_0^2}{M^2 \lambda}\,, \tag{5.16}$$

with an propagation constant of $M^2 = 1.5$ in our setup. This rather large value for M^2 can be enhanced by the usage of better optics. Currently only one inch optics is used in the setup of the optical dipole trap. The collimated laser beam exiting the fibre coupler has a diameter of 13.2 mm. The usage of 1.5 inch optics should improve the beam quality, which would result in a waist of the dipole trap laser beam of 12 µm for $M^2 = 1$.

Another issue concerning experiments in the ODT is the variation of the atomic ground state density. Since all atomic states are trapped in the ODT a Landau-Zener sweep cannot be used to lower the number of atoms in the ODT. Thus, the atom number is lowered in the magnetic trap. Afterwards the remaining atoms are loaded into the dipole trap. This technique comprises an additional heating due to the changed number of atoms in the magnetic trap, which are loaded into the ODT. This means that the temperature increases slightly for increasing Landau-Zener sweep times. The lowered thermalisation rate in the axial direction might be an explanation for this effect. The atomic density distribution in the ODT is calculated by a series of time of flight images (see section 7.1) from which we take the radial temperature and the axial size, which does not increase on the time scale of the time of flight. The radial width σ_r of the density distribution is found by evaluating equation (5.15).

6. Rydberg excitation

One major task regarding experiments with ultracold Rydberg atoms is the excitation of Rydberg atoms. Although this seems to be apparent it is never the less connected to a high technical effort to selectively excite only one specific electronic state. Since the level spacing of Rydberg states become closer with higher principal quantum numbers, the excitation laser must have a linewidth much smaller than this level spacing. On the other hand the laser must produce a sufficient output power to compensate for the decreasing line strengths due to the decreasing transition dipole moments with increasing principal quantum number.
Section 6.1 introduces the details of the excitation scheme into the $43S_{1/2}$ state, which is the Rydberg state of choice throughout this thesis. Section 6.2 will introduce the corresponding laser system consisting of the optical setup as well as the control circuit setup to produce high power output with at a narrow linewidth.

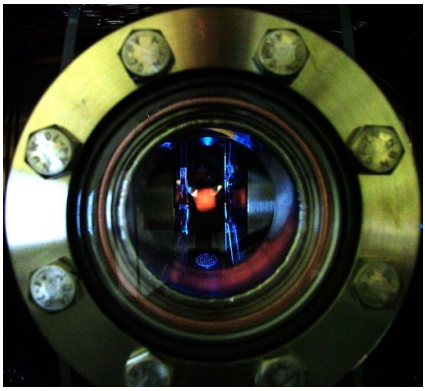

Figure 6.1.: Picture of the running experiment. A magneto-optical trap is visible in the centre of the chamber. The MOT is illuminated with the 480 nm light for the excitation into the Rydberg state seen as reflections on the recessed buckets.

6.1. Level structure and excitation path

The energy level structure of ^{87}Rb and the excitation into the $43S_{1/2}$ state are shown in figure 6.2. For the experiments discussed in this thesis the

$43S_{1/2}$ state is used. As discussed in section 2.2 it is particularly useful to choose an S-state as it has only a repulsive van der Waals interaction. States with higher angular momenta have repulsive and attractive branches of the Rydberg-Rydberg interaction, which leads to interaction induced collisions and, thus, drastically reduces the lifetime of the atomic sample in the Rydberg state. The electric field of the ions produced by a Rydberg-Rydberg collision additionally disturbs the other Rydberg atoms due to their sensitivity on electric fields.

We chose for the experiments in this thesis a Rydberg state with a principal quantum number of $n = 43$. Choosing a Rydberg state with a 'moderate' principal quantum number comes with the advantage of a reasonable high Rabi frequency as the dipole transition matrix element for a 5P to nS transition scales, according to [Hei08a], with the principal number to a power of -1.5. On the other hand a higher principal quantum number would result in a much higher interaction between the Rydberg atoms due to the scaling of the van der Waals interaction with n^{11}.

Since a transition from an S-state to an S-state is forbidden, we use a two-photon excitation depicted in 6.2 via the $5P_{3/2}$ intermediate state. The laser for the lower transition has a wavelength of 780 nm and is σ^+ polarised and, hence, couples to the stretched $5S_{1/2}(f = 2, m_f = 2)$ to $5P_{3/2}(f = 3, m_f = 3)$ transition. This maximises the Rabi frequency according to equation (1.24) and suppresses the excitation via unwanted paths, which would lead to a population of the wrong magnetic sublevel in the Rydberg state. We choose the $43S_{1/2}(j = 1/2, m_j = 1/2)$ state since its magnetic moment equals the magnetic moment of the ground state $5S_{1/2}(f = 2, m_f = 2)$. Hence, the transition is insensitive to the inhomogeneous magnetic potential of the magnetic trap (see section 5.3.1). The Rydberg state is described in terms of the j-basis as the total quantum number f including the angular momentum of the nucleus is not longer a useful quantum number since the coupling between the electron in the $43S_{1/2}$ state and the nucleus is very weak and the f-states are degenerated.

The description of the two-photon excitation in the three-level system can be, according to section 1.8, simplified if the detuning δ_p with respect to any intermediate state is chosen to be large. All experiments presented in part IV except the measurements of the electromagnetically induced transparency are done with a large detuning of $\delta_p \simeq 2\pi \times 500\,\mathrm{MHz}$. Large in this context means larger than all other frequencies in the system, especially the decay rate of the intermediate state, which is in ^{87}Rb $\Gamma_{eg} = 2\pi \times 6\,\mathrm{MHz}$ for a weak laser on the lower transition. If δ_p becomes comparable to Γ_{eg} the intermediate state is significantly populated and must be taken into account (see section 1.7).

A large detuning from the $5P_{3/2}(f = 3, m_f = 3)$ state is also necessary if the excitation into the Rydberg state is done on the long axis of a cigar shaped

atomic cloud as it will be the case in the magnetic trap since the optical density

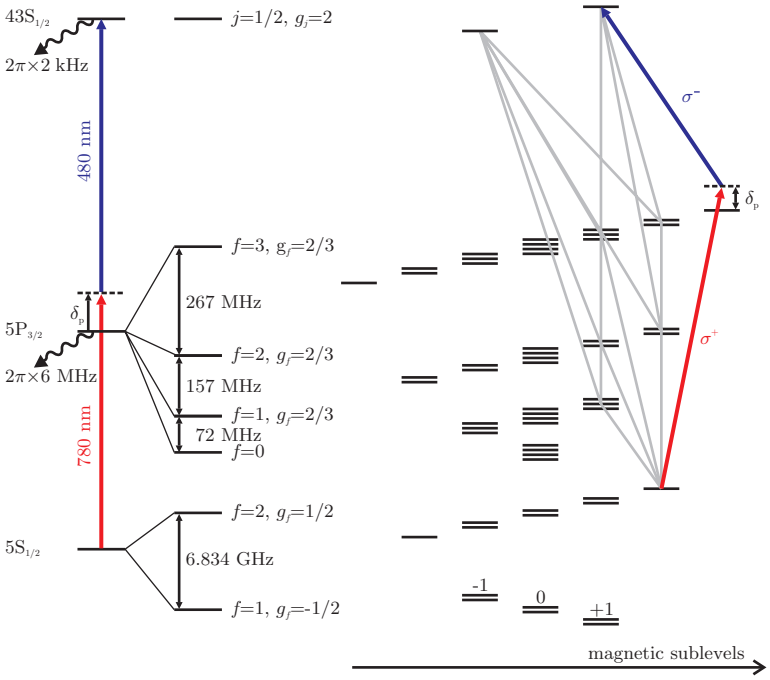

Figure 6.2.: Energy level diagram of ^{87}Rb involving the transitions into the $43S_{1/2}$ Rydberg state. The right diagram shows the energy levels in the j-basis and the coupling into the f-basis as well as the decay rates of the excited states. The number of lines in the right level scheme indicate the number of (j, m_j)-states contributing to the respective (f, m_f)-state. The horizontal splitting indicates the m_j sublevels in the j-basis for the $43S_{1/2}$ state and the m_f magnetic sublevels in the f-basis for the $5S_{1/2}$ and $5P_{3/2}$ states. The transition into the Rydberg level is done by means of a two-photon transition. The 780 nm laser for the lower transition is σ^+ polarised, the 480 nm laser σ^-. Using the stretched $5S_{1/2}(f = 2, m_f = 2)$ to $5P_{3/2}(f = 3, m_f = 3)$ transition for the lower excitation maximises the Rabi frequency and suppresses the excitation along unwanted paths shown in grey. If the 780 nm laser is far detuned from the intermediate state by a large detuning the system can, according to the discussion in section 1.8, be treated as an effective two-level system. The line strengths can be calculated using the MatLab program given in appendix A.1.

given by equation (7.7) is on the order of 5×10^3 for $\delta_\mathrm{p} = 0$. The optical density reduces to 0.2 for a large detuning $\delta_\mathrm{p} = 2\pi \times 500\,\mathrm{MHz}$. The inequality given by equation (1.41) restricts the Rabi frequency for the lower transition to $\Omega_\mathrm{p} < {}^{2\Omega_\mathrm{c}\delta_\mathrm{p}}/_{\Gamma_\mathrm{eg}}$ in order to fulfil the the requirements for coherent excitation in the effective two-level system.

6.2. The Rydberg laser system

6.2.1. Optical setup

The Rydberg laser system underlies two major constraints. The decrease of the Rabi frequency due the dipole transition matrix element with the $n^{-1.5}$-dependency (see equation (1.5) and section 2.1) can be compensated if the electric field amplitude $\mathcal{E}_0 \sim \sqrt{I}$ is large. Thus, a high output power of the laser system is required. The optical setup for the generation of the excitation light is shown in figure 6.4. The setup is mainly build on two tables to minimise disturbances. The light is connected to the main chamber by polarisation maintaining fibres[1].

The table denoted 'diode lasers' contains basically three homemade diode lasers and their stabilisations. A first diode laser in a Littrow setup produces the 780 nm light for the lower transition (see figure 6.2). This laser can be actively stabilised either by using a polarisation spectroscopy or a modulation transfer spectroscopy [Shi82].

The latter supports a very stable lock to the $5S_{1/2}(f = 2, m_f = 2)$ to $5P_{3/2}(f = 3, m_f = 3)$ transition by using an electro-optical modulator[2] adding frequency sidebands to the laser. Each frequency sideband experiences a different absorption and dispersion due to the presence of a strong pump laser. These differences can be monitored using phase sensitive measurements of the amplitude modulated probe beam. The polarisation spectroscopy is used when ever the laser shall be locked to an other transition, since the modulation transfer spectroscopy gives poor signals for all transition except the stretched transition.

Before the light is coupled into the fibre and brought to the experiment it passes an 200 MHz acoustic-optic modulator (AOM)[3] twice to shift the frequency of the light by up to 500 MHz. The AOM is mounted on a magnetic base plate and can be easily replaced by an 80 MHz AOM, which can be used to tune the laser on resonance with the $5S_{1/2}(f = 2, m_f = 2)$ to $5P_{3/2}(f = 3, m_f = 3)$ transition by locking the laser to the (1,3)-crossover resonance.

One approach to produce 480 nm light with sufficient power is to use pulsed lasers, which have the advantage of very high intensities, but the disadvantage of large linewidths. Large laser linewidths would constitute a contradiction to the result $\Omega_c > \sqrt{\Gamma_{eg}\,\gamma_d}$ from inequality (1.41) needed for a coherent evolution of the system. Another possibility would be to use dye jet lasers, which come

[1] PMC fibres, Schäfter + Kirchhoff
[2] EOM with modulation frequencies of either 2 MHz or 10 MHz from Nova Phase, Inc.
[3] typically TeO_2 modulators of the 3200 series from Crystal Technology, Inc.

with a much smaller linewidth and a high output power, but are difficult to handle.
In this setup the 480 nm light for the excitation into the Rydberg state is produced by means of frequency doubling a 960 nm laser. The setup for the creation of the 960 nm light consist of two homemade diode lasers, namely a master and a slave laser. The master laser is build in a Littrow setup, double passes a 400 MHz AOM and is seeding the slave laser. In order to make the slave laser follow the master, it is required that the frequency of the slave laser without seeding is almost equal to the frequency of the master laser. Since the slave laser has no diffraction grating to tune the frequency, this is achieved by cooling the diode in an evacuated housing to -35 °C. The 960 nm light is sent through a polarisation maintaining fibre into a commercial second harmonic generator[4] consisting of a tapered amplifier and a frequency doubling cavity. The doubling cavity, situated on the table 'doubling cavity' in figure 6.4, has typically an output of well above 200 mW. The light passes an AOM to switch the light and is coupled into a polarisation maintaining fibre after which $\simeq$ 70 mW of 480 nm light are available in front of the main chamber.

For the stabilisation of the 480 nm laser we choose a scheme, where we lock the 960 nm laser. Since there is no available spectroscopic line of rubidium in the vicinity of 960 nm a Invar transfer cavity is used. This cavity is stabilised on the already locked 780 nm laser. The 960 nm laser is than locked to the stabilised cavity. The details of the locking scheme will be discussed in the next section. The cavity can be evacuated as a change in the air pressure would result in a change of the refractive index inside the cavity. The refractive index in air is different for 780 nm and 960 nm and a change would lead to a drift of the frequency with respect to each other. With this setup and the electronics described in section 6.2.2 the 780 nm and 960 nm lasers can be stabilised with respect to each other to a linewidth smaller than $\simeq 2\pi \times 1.5$ MHz on the minute time scale.

6.2.2. Electronic setup

The second major constraint for the Rydberg laser system is that the high output power produced with the setup discussed in section 6.2.1 must have a narrow linewidth, e.g. in comparison to the Rabi frequency of the upper transition of the two-photon excitation in order to fullfil the condition $\Omega_c > \sqrt{\Gamma\gamma_d}$ for a coherent dynamics in an effective two-level atom (see section 1.8 for details). A laser linewidth on the order of the inverse lifetime of the Rydberg state would be desirable, but is technically challenging.

The electronic part of the locking scheme is depicted in figure 6.3. The

[4] TA-SHG 110, Toptica Photonics AG

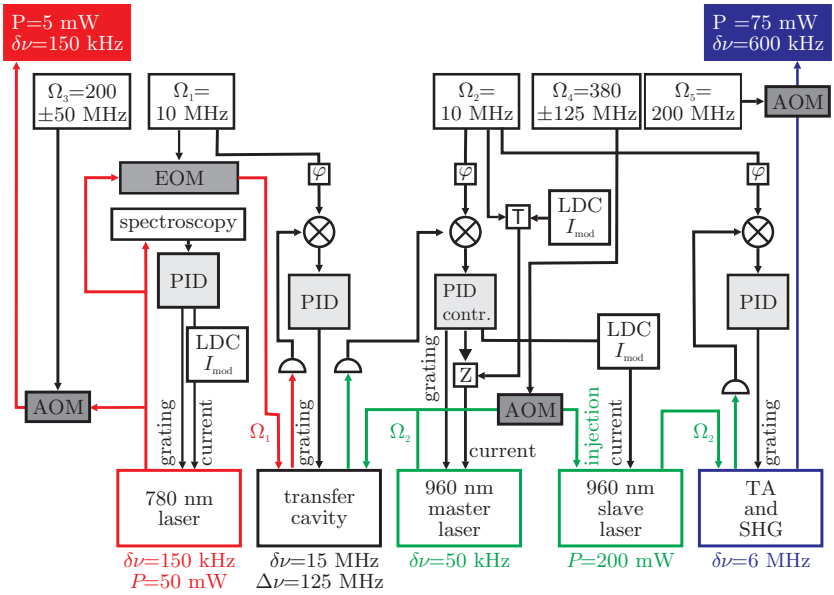

Figure 6.3.: Locking scheme for the Rydberg laser system. The coloured lines depict connections with light, while the black lines are electronic connections. The 780 nm laser is stabilised to a spectroscopy. The transfer cavity is stabilised to the 780 nm light. Finally, the 960 nm light is stabilised to the transfer cavity. The frequencies of both lasers are stable with respect to each other better than $\simeq 2\pi \times 1.5\,\mathrm{MHz}$.

780 nm and 960 nm master laser are stabilised by homemade PID controllers [Hei08a]. The controller is built such that it can stabilise the laser frequency on a slow time scale by modulating the grating of the laser using piezo ceramics and on a fast time scale by directly modulating the current of the laser diode.

In the case of the 780 nm laser the current modulation is achieved by using the modulation input of the diode laser controller[5]. The modulation input of these laser controllers are not fast enough to modulate the current of the 960 nm laser with 10 MHz (see below). We overcome this problem with a MOSFET circuit symbolised by Z in figure 6.3, which 'steals' current from the diode laser. The PID controller for the 960 nm master laser controls also the current for the 960 nm slave laser. This is the only possibility to fine-tune

[5]ITC 102, Thorlabs, Inc.

the frequency of the slave laser since it has no grating.

As pointed out in section 6.2.1 rubidium has no spectroscopic line available in the vicinity of 960 nm. The locking of the master laser is also depicted in figure 6.3. For this purpose the amplitude of the 780 nm light is modulated with 10 MHz using an EOM and sent through the transfer cavity. The resonator is locked using a photodiode imaging the 780 nm light, which is afterwards phase shifted (⍁ symbol) and demodulated (⊗ symbol) according to the frequency modulation spectroscopy scheme presented in [Bjo83]. The locking of the 960 nm master laser works the same way. The amplitude of this laser is modulated by modulating the current at a frequency 10 MHz. This results also in a modulation of the amplitude of the slave laser, which can be used to lock the doubling cavity to its resonance. Since the modulation of the amplitude comes with a frequency modulation and, thus, sidebands, the modulation frequency must be chose such, that the sidebands are not passing the doubling cavity: The modulation frequency of 10 MHz must be larger than the linewidth of the doubling cavity of the second harmonic generator, which is 6 MHz for our system.

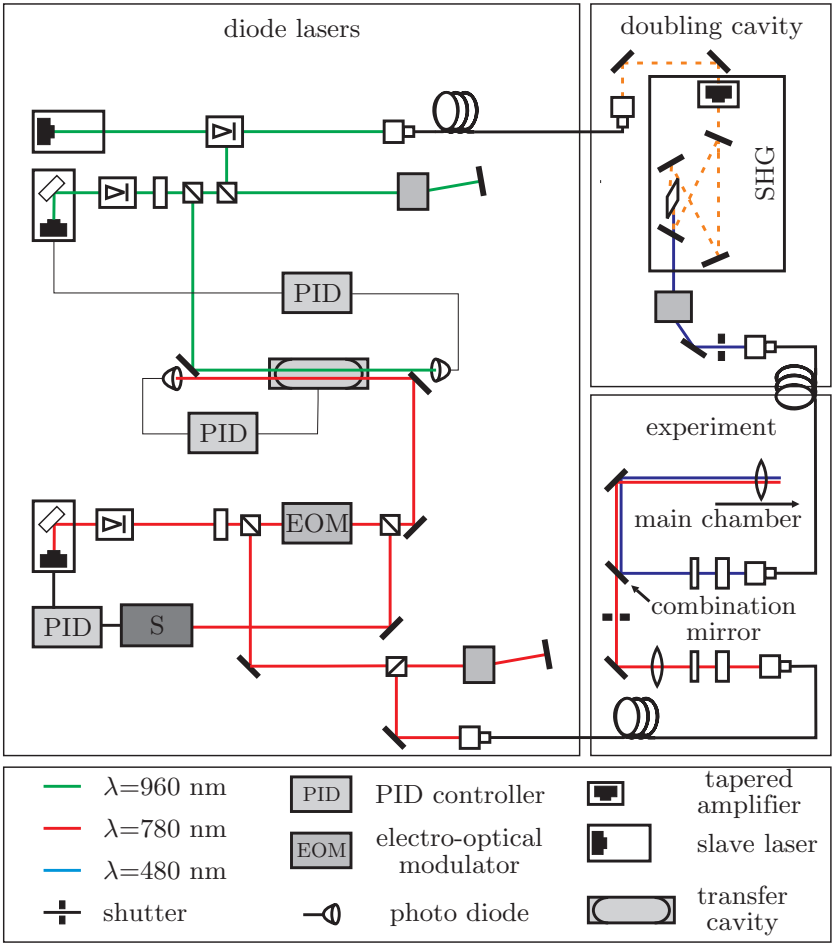

Figure 6.4.: Optical setup for the Rydberg excitation. The setup is distributed over three optical tables. The table denoted 'diode laser' contains three diode lasers producing the 780 nm (red lines) and 960 nm (green lines) light, which is frequency doubled on the 'doubling cavity' table for the two-photon transition. Additionally the diode laser table contains a rubidium saturation spectroscopy to lock the 780 nm laser and a transfer cavity, which is locked to the 780 nm laser, to stabilise the 960 nm laser in a Pound-Drever-Hall like locking scheme (see also figure 6.3). Both excitation lasers are brought to the 'experiment' table with polarisation maintaining fibres and are combined with a combination mirror. The scheme uses also symbols explained in figure 5.3.

7. Detection

The last chapter of this part as well as of every experimental sequence, depicted in figure 7.1, covers the detection of atoms. There is a rich diversity of different detection methods for atoms in the world of cold atom physics. The most commonly used detection methods for neutral atoms are the fluorescence imaging and the absorption imaging. Both methods have the big advantage of being simple and the disadvantage of being destructive, i.e. only one picture can be taken per atomic sample. The first section will discuss the absorption imaging as it is used for the detection of trapped ultracold atoms. Due to the high optical density the florescence imaging is not suitable for this purpose.
The second section deals with the detection of Rydberg atoms. Since the dipole matrix element of the transition into the Rydberg state is very small the Rydberg state has a relatively long lifetime. Hence, a fluorescence imaging is unsatisfying due to a very small signal. However, using EIT (see section 1.7 and section 9.2) one can detect Rydberg atoms optically. Another method is to detect the ions, which result from field ionisation of Rydberg atoms. Section 7.2 introduces this method.

7.1. Detection of ground state atoms

As pointed out in the introduction the absorption imaging is the commonly used method to detect dense atomic clouds. The name of this method already implies the setup used for detection. A resonant light beam passes the atomic sample and a shadow of the atomic cloud is afterwards detected by a charge-coupled device (CCD) camera to obtain spatially resolved pictures. Assuming a two-level atom, which is justified in the case of a reasonable narrow laser, the scattering rate of an atom with decay rate Γ in the steady state is according to equation (1.15)

$$\Gamma_\mathrm{s} = \Gamma\varsigma'_\mathrm{ee} = \frac{\Gamma\Omega^2}{4\delta^2 + \Gamma^2 + 2\Omega^2}\,. \tag{7.1}$$

The scattering of photons on a line, e.g. in y-direction, through an atomic cloud with $n(x, y, z)$ leads to a reduction of the incident intensity. In the case of small intentsities, i.e. $\Omega < \max(\Gamma, |\delta|)$ the reduction is given by

$$\frac{\mathrm{d}I}{\mathrm{d}y} = -\sigma\, I\, n(x, y, z)\,, \tag{7.2}$$

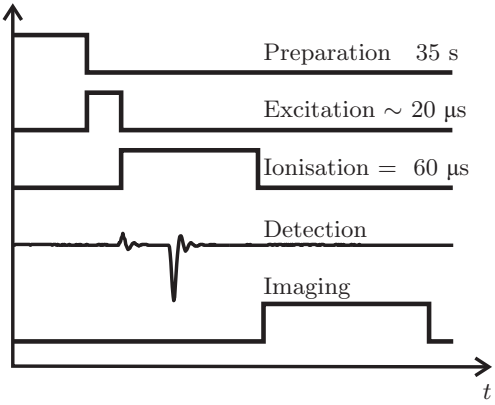

Figure 7.1.: Typical experimental sequence for a Rydberg excitation of a ultracold atomic sample. After the preparation, which includes all the cooling and trapping steps, the cloud is excited, field ionised and the remaining ground state atoms are imaged.

with the scattering cross section defined as the fraction between scattered power and incident intensity

$$\sigma \equiv \frac{P_{\text{atom}}}{I} = \frac{\hbar\omega_{\text{l}}\Gamma_{\text{s}}}{I} = \frac{\sigma_0}{1 + (2\delta/\Gamma)^2 + 2(\Omega/\Gamma)^2}\,, \tag{7.3}$$

with the on-resonance scattering cross section

$$\sigma_0 = \frac{\hbar\omega_{\text{l}}\Gamma}{2I_{\text{s}}}\,, \tag{7.4}$$

and the definition of the saturation intensity, with $I = c\epsilon_0 E_0^2/2$ and the definition of the Rabi frequency in equation(1.5)

$$I_{\text{s}} = \frac{c\epsilon_0(\hbar\Gamma)^2}{4|\boldsymbol{\epsilon}\cdot\boldsymbol{d}|^2} = \frac{\pi hc\Gamma}{3\lambda^3}\,. \tag{7.5}$$

Usually the absorption imaging is done on resonance, i.e. $\delta = 0$. If the Rabi frequency fulfils $\Omega \ll \Gamma$ equation (7.2) becomes independent of the intensity, which leads to the Lambert-Beer law

$$I(x,z) = I_0 \mathrm{e}^{-\text{ก}}\,, \tag{7.6}$$

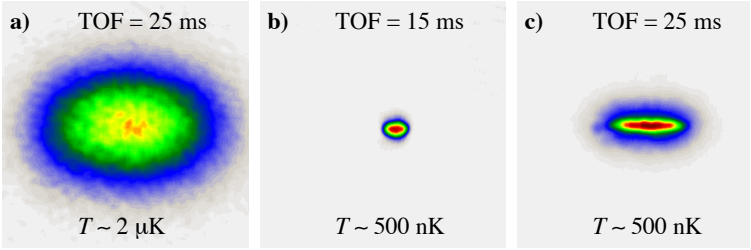

Figure 7.2.: Absorption imaging pictures for different temperatures and different time of flights. The dark red corresponds to an optical density of 3. Image **a)** shows a thermal cloud. The high densities at ultralow temperatures cause a Bose enhancement resulting in an anisotropy of the aspect ratio of the the cloud [Löw06]. The images **b)** and **c)** show an atomic sample with a temperature below the critical temperature for the phase transition to a Bose-Einstein condensate for different time of flights. The condensation is visible as an increase of the peak density and a different density profile of the cloud.

with the optical density

$$\text{ñ} = \sigma_0 \int_{-\infty}^{+\infty} n(x,y,z)\mathrm{d}y\,. \tag{7.7}$$

With the atomic density given by equation (5.8) and equation (5.10) the atom number in the trap can be calculated using the peak value ñ_0 of the optical density

$$N_0 = 2\pi\sigma_r\sigma_z \frac{\text{ñ}_0}{\sigma_0}\,. \tag{7.8}$$

The widths of the cloud are obtained from the absorption images of which three examples for different densities are shown in figure 7.2. The images b) and c) in this figure show an atomic sample, which temperature is below the critical temperature for the phase transition to a Bose-Einstein condensate. The experiments in this thesis will be done at temperatures of the atomic sample above this critical temperature and can be described by a thermal density distribution. The spatial resolution of the imaging system in the presented setup is 5.6 µm. The optical density in the trap along the radial direction of the cigar shaped cloud is on the order of 100 on resonance. The used CCD camera[1] has a intensity resolution of 12 bit, which corresponds, according to

[1] PixelFly QE, PCO Computer Optics GmbH

equation (7.6), to a optical density $\text{ñ}_{\max} = 8.3$ that can be detected at most. Hence, an ultracold atomic cloud cannot be detected in the trap. To obtain the density distribution the cloud is released from the trap and imaged after a time of flight. The temporal expansion of the cloud together with the trapping frequencies yields the spatial density distribution of the ground state atoms.

We image for a time 100 µs with an intensity $I \sim {}^{I_s}/_4$ with σ^+ polarised light on the $5S_{1/2}(f = 2, m_f = 2)$ to $5P_{3/2}(f = 3, m_f = 3)$ transition. A series of absorption images for different end frequencies for the evaporative cooling, thus, different temperatures, are shown in figure 7.2. The temperature is obtained using the function

$$\sigma_i(t) = \sqrt{\sigma_i(0)^2 + \frac{k_B T}{m} t^2}\,, \tag{7.9}$$

to fit the Gaussian widths of the atomic cloud in a series of time of flight pictures. The width of the cloud $\sigma_i(0)$ in the trap is obtained from the measured trapping frequencies and the equations (5.9).

7.2. Detection of Rydberg atoms

The second important detection scheme is the detection of Rydberg atoms. Due to the long lifetime of Rydberg atoms any detection process involving the spontaneous scattering of photons are not practicable since the signal would be $\simeq$4000 times smaller.

The Rydberg atoms can be detected optically with resonant ($\delta_p = 0$) light by means of electromagnetically induced transparency as it is discussed in section 9.2.

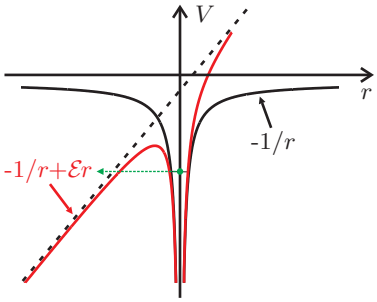

Figure 7.3.: Illustration of the field ionisation. Applying an electric field $\mathcal{E}$ (dashed line) perturbs the Coulomb potential of the core (black line) such that the electron can tunnel out.

A different approach for a non-optical detection of Rydberg atoms is to use their large polarisability. When applying a large electric field the electron tunnels out of the Coulomb potential of the core (see figure 7.3). For even

higher electric fields the potential barrier can be lowered further such that the electron is unbound from the core. The resulting electron and the ion can then be detected using e.g. multichannel plates (MCPs)[2]. MCPs are secondary electron multiplier and consist of at least one glass plate with millions of holes with a diameter on the order of 10 µm and an anode to detect the electrons.

A high voltage applied over the glass plate accelerates the charged particle, which subsequently hits a wall inside a channel and disengage secondary electrons, which in turn are accelerated again. The efficiency of this process can be optimised by arranging the channels under an angle with respect to the front surface of the MCP. In our experiment the MCP consists of two glass plates in such a chevron arrangement. The front of the MCP is set to a voltage of -2 kV. In order to shield the resulting high electric fields from the ions, the MCPs are covered by Faraday cages with a cone-shape (see the figures 5.1 and 7.4).

After amplification about 10^7 electrons reaching the anode of the MCP. The current caused by the electrons is measured as a voltage drop over a resistor. This voltage is amplified using a standard operation amplifier and detected by a digitiser card[3] with a time resolution of 50 ns.

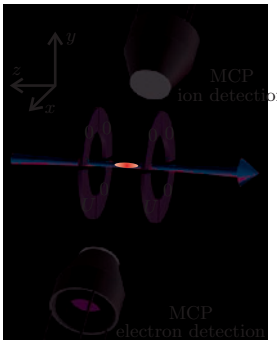

Figure 7.4.: Schematic of the inside of the chamber with the electric field plates, the MCPs and the excitation laser. Two of the eight field plates are set to a voltage U to drag ions out during excitation and to field ionise the Rydberg atoms after excitation.

Currently only one of two MCPs (see figure 5.1) are in use to detect rubidium ions. The second one could be used to simultaneously detect electrons. The detection of the electrons would yield a better time resolution due to their smaller mass but suffers from free electrons in the vacuum chamber e.g. produced by the ion pump. However, the time resolution for the ion detection is sufficient for the experiments discussed in this thesis and, hence, only the MCP for the detection of ions is used.

[2] B012VA, El-Mul Technologies, Ltd.
[3] NI 5102, National Instruments Corporation

A schematic view of the inside of the chamber with the field plates and the excitation laser are depicted in figure 7.4. The cloud is enclosed by eight capacitor plates which can independently be set to a voltage. We use them for two purposes. The first is to drag ions out of the excitation volume to prevent unwanted electric fields over the atomic sample during the excitation. The second purpose is the field ionisation. For that the field plates opposite to the MCP for ion detection are set to a voltage of $U \simeq 2\,\mathrm{kV}$, which ionises the Rydberg atoms and push the ions directly to the MCP. The switching of the voltages from 10 V during the excitation to 2 kV for field ionisation is done with a commercial fast high voltage transistor push-pull switch[4] within $\simeq 50\,\mathrm{ns}$.

[4] HTS 61-03-GSM, Behlke Electronic GmbH

Part IV.

Results

8. Universal scaling

This chapter will present the experimental results on the universal scaling behaviour of the Rydberg excitation dynamics. Rydberg excitation dynamics have been studied in some detail for magnetically trapped atoms in reference [Hei07]. It was shown that the initial slope and the saturation value of the excitation curves depend on the single atom Rabi frequency and the atomic peak density of ground state atoms according to simple power laws. Moreover, by investigating the exponents of the scaling laws the Rydberg excitation was shown to be collective and coherent.
As pointed out in reference [Wei08] and section 4.2 it is expected to find an algebraic scaling behaviour of the Rydberg fraction with the characteristic parameters, which appears from the renormalisation of the Hamilton operator describing the system. The appearance of such a power law is a strong evidence for a second order quantum phase transition of the Rydberg system.
The scaling behaviour of the Rydberg excitation is investigated for different atomic ground state peak densities, single atom Rabi frequencies and geometric shapes of the atomic sample. The dependence of the universal exponents on the dimensionality allows to draw conclusions on the spatial distribution of the Rydberg excitation. The dimensionality of the atomic sample is changed by loading the atoms from a magnetic trap into a tightly focused optical dipole trap. The theoretically expected exponents for the characteristics of the Rydberg excitation curves will be derived in section 8.1 based the generalised superatom model discussed in section 3.4.
The results of the measurement of the universal scaling behaviour of the Rydberg excitation are shown in section 8.2. The experimental data will be compared to theoretical predictions of a mean field model derived in reference [Wei08] and the generalised superatom model presented in section 3.4. Two different systems are used for the measurements of the universal scaling. The atomic samples, that are magnetically trapped, have a radial size that is larger than the blockade radius. Trapping the atomic sample in an optical dipole trap leads to confinements in which the radial size is equal or smaller as the blockade radius.

8.1. Scaling of the excitation

Section 4.2 introduced the ideas of the universal scaling to the driven Rydberg system, which is expected to exhibit a quantum phase transition in the parameter $\Delta = \hbar\delta/C_p\, n_g^\beta$, with the two-photon detuning δ (see figure 4.2 b)) and the interaction energy $C_p n_g^\beta$ given by the atomic ground state density n_g. The exponent $\beta = p/d$ is dependent on the exponent of the r-dependence of the interaction, i.e. $\mathcal{V} \sim r^{-p}$, and the dimensionality d of the atomic sample.

For a finite single atom Rabi frequency Ω_0 and $\Delta = 0$, i.e. the laser is on two-photon resonance, the system is located in the critical region of the phase diagram shown in figure 4.2 a).

The Rydberg excitation curves can be characterised by the initial slope R and saturation value N_{sat} as shown in figure 8.3. These characteristics can be written in terms of dimensionless parameters leading to the Rydberg fraction in the saturation $f_{\mathrm{sat}}$and the normalised initial slope f_R, which must not be mistaken with the general Rydberg fraction f.

The scaling laws for R and N_{sat} with the atomic ground state density and the Rabi frequency are derived in section 3.4. Using equation (3.20) and the scaling of R and N_{sat} with the collective Rabi freuquency Ω_N given in table 3.1 one finds for a volume V

$$\begin{aligned} R &\sim V\Omega_N^{\beta+1/\beta} \sim N_0 n_g^\beta\, \alpha^{2(\beta+1)/(2\beta+1)}\,, \\ N_{\mathrm{sat}} &\sim V\Omega_N^{1/\beta} \sim N_0 \alpha^{2/(2\beta+1)}\,, \end{aligned} \tag{8.1}$$

with the atomic density of atoms in the ground state n_g and the atom number in the ground state $N_0 = n_g V$. The parameter

$$\alpha \equiv \frac{\hbar\Omega_0}{C_p n_g^\beta}\,, \tag{8.2}$$

compares the coupling energy $\hbar\Omega_0$ with the interaction energy $C_p n_g^\beta$, which was also introduced in section 4.2.

Rescaling the quantities in equation (8.1) leads to the dimensionless parameter for the initial rate

$$f_R \equiv \frac{R}{N_0 n_g^\beta} \sim \alpha^{2(\beta+1)/(2\beta+1)} \sim \alpha^{\nu_R}\,, \tag{8.3}$$

and for the saturation level

$$f_{\mathrm{sat}} \equiv \frac{N_{\mathrm{sat}}}{N_0} \sim \alpha^{2/(2\beta+1)} \sim \alpha^{\nu_{\mathrm{sat}}}\,. \tag{8.4}$$

Both f_R and f_{sat} exhibit a power law dependence on α. The critical exponents are $\nu_R = 2(\beta+1)/(2\beta+1)$ and $\nu_{\mathrm{sat}} = 2/(2\beta+1)$ for f_R and f_{sat}, respectively. In the

case of van der Waals interaction between the Rydberg atoms a scaling of f_R and f_{sat} with the exponents $\nu_R = {}^6/_5$ and $\nu_{\mathrm{sat}} = {}^2/_5$ is expected in an atomic sample with a three dimensional shape. For a one dimensional geometry of the atomic cloud the exponents are $\nu_R = {}^{14}/_{13}$ and $\nu_{\mathrm{sat}} = {}^2/_{13}$.

8.2. Measurement of the universal scaling

For the systematic study of Rydberg excitation the following experimental sequence has been used. After evaporative cooling of the ^{87}Rb atoms in the $5\mathrm{S}_{1/2}(f = 2, m_f = 2)$ state (see section 5.3.1), the atoms are excited by a two-photon transition via the intermediate $5\mathrm{P}_{3/2}(f = 3, m_f = 3)$ state into the $43\mathrm{S}_{1/2}(j = {}^1/_2, m_j = {}^1/_2)$ Rydberg state. The 780 nm laser for the lower transition is σ^+ polarised and has a detuning with respect to the $5\mathrm{S}_{1/2}(f = 2, m_f = 2)$ to $5\mathrm{P}_{3/2}(f = 3, m_f = 3)$ transition of $2\pi \times 470$ MHz. According to section 1.8 the system can be treated as an effective two-level atom driven by an effective two-level Rabi frequency Ω_0.

The ultracold atomic sample is excited for pulse durations between 100 ns and 20 µs, which is much smaller than the lifetime of the $43\mathrm{S}_{1/2}$ Rydberg state of $\simeq$100 µs. After the excitation the Rydberg atoms are field ionised and detected by a multi-channel plate (MCP) resulting in strongly blocked excitation curves (see figure 8.3 and [Hei07]). The atomic density of the remaining ground state atoms are monitored by means of absorption images described in section 7.1.

The parameter α on which the characteristics f_R and f_{sat} depend with power laws is varied by either changing the power of the 780 nm laser and, thus, the effective Rabi frequency Ω_0 or by changing the atomic peak density of ground state atoms n_0 by means of a Landau-Zener sweep described in section 5.3.3. The parameter α can be written in terms of the peak density as $\alpha = {}^{\hbar\Omega}/_{C_p n_0^\beta}$ if the spatial part $\tilde{n}_{\mathrm{g}}(r)$ of the density distribution $n_{\mathrm{g}}(r) = n_0\tilde{n}_{\mathrm{g}}(r)$ is fixed for all experiments.

Two different experimental setups as shown in figure 8.1 are used for the experimental investigation of the universal scaling and its dependence on the dimensionality of the system. The experimental setup allows the shape of the atomic sample to be tailored from a three dimensional geometry to a quasi one dimensional geometry. In a one dimensional geometry, i.e. if the radial size of the cloud is much smaller than the blockade radius defined by equation (3.2) the universal exponents would change their values according to section 8.1. Thus, the values of these exponents give an indication of the distribution of the Rydberg excitation in the atomic cloud. Many properties of the local dynamics of the Rydberg excitation can be obtained by the investigation of the global characteristics of the Rydberg excitation.

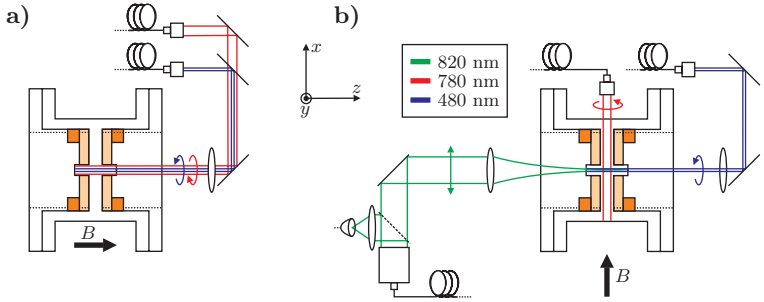

Figure 8.1.: Schematic of the setup used for the universal scaling measurements. **a)** Measurements in the magnetic trap: Both excitation beams enter the the main chamber colinear and copropagating. The 780 nm laser beam is σ^+ polarised, the 480 nm laser beam is σ^- polarised with respect to the quantisation axis in the z-direction. **b)** Measurements in the optical dipole trap. The ODT is linearly polarised along the x-direction. The atomic sample is illuminated radially to avoid inhomogeneities in the Rabi frequency due to the high optical density along the long axis of the cigar shaped atomic cloud in the ODT. The quantisation axis and polarisation is chosen such that the 780 nm laser beam is σ^+ polarised. The 480 nm laser beam is right handed circular polarised.

The first experiment was done with magnetically trapped ^{87}Rb atoms and the data are published in [Hei07], where the coherent collective behaviour of the excitation was shown. The atomic cloud has a temperature of 3.4 µK, which is kept constant for all experiments. The size of the cloud is $\sigma_r = 8.7\,\mu\text{m}$ and $\sigma_r = 150\,\mu\text{m}$ in radial and axial direction, respectively. The sizes of the excitation laser beams are $\simeq$600 µm for the 780 nm laser and 42 µm for the 480 nm laser. Therefore, the Rabi frequency is constant over the atomic sample.

With the given sizes of the atomic cloud and a maximal atom number of $N_0 = 1.5 \times 10^7$ in the ground state the atomic ground state peak density in three dimensions is given according to equation (5.10) $n_0 = n_{3\text{d}} = 8.0 \times 10^{19}\,\text{m}^{-3}$. The peak density of atoms in the ground state is varied between this value and a minimal value of $n_{3\text{d}} = 2.8 \times 10^{18}\,\text{m}^{-3}$ for a maximal Landau-Zener sweep time of 0.8 s. Assuming that the density distribution is purely one dimensional, thus $n_{1\text{d}} = {}^{N_0}/_{(\sqrt{2\pi}\sigma_z)}$, the peak density varies between $n_{1\text{d}} = 1.3 \times 10^9\,\text{m}^{-1}$ and $n_{1\text{d}} = 3.8 \times 10^{10}\,\text{m}^{-1}$. Figure 8.2 shows the parameter space which is scanned to investigate the scaling behaviour of the Rydberg excitation.

The effective single atom Rabi frequency Ω_0 is calculated using equation (1.36) with a detuning of $\delta_p = 2\pi \times 470\,\mathrm{MHz}$ from the intermediate $5P_{3/2}$ state. The value of Ω_0 is varied between $2\pi \times 31\,\mathrm{kHz}$ and $2\pi \times 154\,\mathrm{kHz}$.

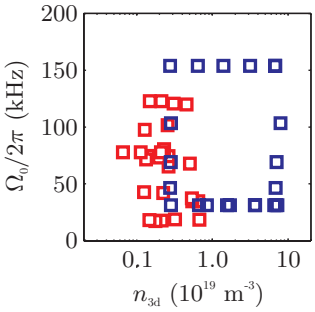

Figure 8.2.: Scanned parameter space for the experiments to investigate the scaling behaviour of the Rydberg excitation. The experiments are done with magnetically trapped atoms (□) and with atomic samples trapped in an optical dipole trap (□).

In order to reduce the dimensionality of the system the atomic cloud is transferred into an optical dipole trap (ODT) as described in section 5.4. We wait for 100 ms after the transfer in the ODT to let the atomic sample thermalise. Thus, any effect of remaining untrapped atoms, which are lost during the loading process into the ODT and would change the spatial distriubtion to a rather three dimensional cloud can be neglected. Figure 8.1 b) shows the setup for the experimental investigation of the scaling behaviour of the Rydberg excitation in the ODT. The atomic sample is illuminated along the radial direction to avoid inhomogeneous Rabi frequencies due to the high optical density along the long axis of the cigar shaped atomic cloud in the ODT (see also sections 7.1 and 9.1.2). The temperature of the atomic sample is varied between 2.2 µK and 6.3 µK resulting in sizes of the atomic sample between 3.2 µm and 5.4 µm in radial direction and between 460 µm and 540 µm in axial direction. Due to the resolution of the imaging system being 5.6 µm the radial size has to be calculated from the trapping potential of the ODT and the temperature of the atomic sample using equation (5.15). The size in the axial direction can be measured directly by means of absorption images. The 3d peak density n_{3d} is varies between $6.6 \times 10^{17}\,\mathrm{m}^{-3}$ and $6.7 \times 10^{18}\,\mathrm{m}^{-3}$ or, assuming a one dimensional density distribution with the peak density n_{1d}, between $1.2 \times 10^{8}\,\mathrm{m}^{-1}$ and $4.2 \times 10^{8}\,\mathrm{m}^{-1}$. The detuning from the intermediate $5P_{3/2}$ state is $\delta_p = 2\pi \times 490\,\mathrm{MHz}$ resulting in effective single atom Rabi frequencies Ω_0 between $2\pi \times 17\,\mathrm{kHz}$ and $2\pi \times 122\,\mathrm{kHz}$.

Figure 8.3 shows as an example one of the Rydberg excitation curves from which the universal scaling is obtained. The solid line shows a fit according to section 3.4 with an exponential saturation function of the form $N_R(\tau) = N_{sat}(1 - \exp(-R/N_{sat}\,\tau))$. Although this function does not reproduce

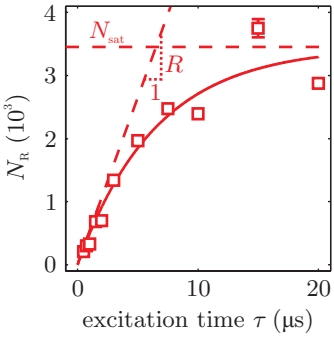

Figure 8.3.: Typical excitation curves for atoms trapped in the ODT with $n_{3d} = 6.7 \times 10^{18}\,\mathrm{m}^{-3}$ and $\Omega_0 = 2\pi \times 19\,\mathrm{kHz}$. The dashed lines indicate the characteristics of the excitation curves, namely the initial slope R and the saturation value N_{sat}. The error bar represent the statistical error for an average over ten independent measurements.

the complete excitation dynamics, especially not the quadratic rise for very short times when the Rydberg excitation shows a single atom behaviour, it reproduces the important properties R and N_{sat}. From these quantities, together with the atom numbers and atomic densities in the ground state the dimensionless parameters f_R and f_{sat} can be calculated.

The dependence on the single atom Rabi frequency Ω_0 and the atomic ground state peak density n_0 is according to equation (8.3) and (8.4) for the Rydberg fraction during the initial slope

$$f_R \sim n_0^{a_R} \Omega_0^{b_R}\,, \tag{8.5}$$

with

$$\begin{aligned} a_R &= {}^{-2\beta(\beta+1)}/_{(2\beta+1)}\,, \\ b_R &= {}^{2(\beta+1)}/_{(2\beta+1)}\,, \end{aligned} \tag{8.6}$$

and for the Rydberg fraction in the saturation regime

$$f_{sat} \sim n_0^{a_{sat}} \Omega_0^{b_{sat}}\,, \tag{8.7}$$

with

$$\begin{aligned} a_{sat} &= {}^{-2\beta}/_{(2\beta+1)}\,, \\ b_{sat} &= {}^{2}/_{(2\beta+1)}\,. \end{aligned} \tag{8.8}$$

Since a power law is expected to reproduce $f_R$and f_{sat}it is useful to evaluate the data in double logarithmic space and fit simple flat planes in this space to the measurements. Hence, the obtained values for R and N_{sat} are fitted with two dimensional fits of the form $\lg(f_{X,Y}) = a_{X,Y} \lg(n_Y) + b_{X,Y} \lg(\Omega_0) + c$ with $X \in \{R, \mathrm{sat}\}$ and $Y \in \{1\mathrm{d}, 3\mathrm{d}\}$. The obtained values for the coefficients $a_{X,Y}$

and $b_{X,Y}$ are listed in table 8.1 for magnetically trapped atoms and in table 8.2 for atoms trapped in the ODT.

According to equations (8.3) and (8.4) it is also expected to find a power law dependence for the dimensionless parameters of the form $f_{X,Y} \sim \alpha_Y^{\nu_{X,Y}}$ with $\nu_{R,Y} = {}^{2(\beta+1)}/_{(2\beta+1)}$ and $\nu_{\mathrm{sat},Y} = {}^{2}/_{(2\beta+1)}$. An evaluation of the data shown in figure 8.4 with a fit function of the form $\lg(f_{X,Y}) = \nu_{X,Y} \lg(\alpha_Y) + c$ yields the critical exponents $\nu_{X,Y}$ of α, as shown in the third column in table 8.1 and 8.2 for a one and three dimensional geometry of the atomic sample. Both the critical exponent as well as the offset c are free fit parameters. The data sets for the measurements in the magnetic trap show a different offset in comparison to those taken with atoms trapped in an ODT. The origin of this difference might reflect a deviation of the detector efficiency, e.g. to different positions of the atomic sample with respect to the detector in the magnetic and optical dipole trap. This 'misalignment' of the optical dipole trap with respect to the magnetic trap is on the order of 100 µm. A specific experiment in which the position of the atomic sample is varied might clarify this point.

The comparison between the measured and the theoretically expected exponents is given in units of the error σ obtained from the power law fits corresponding to the 68 % confidence interval, and as the relative deviation of the experimental to the theoretical value. The next section 8.3 covers the interpretation of the measurements on the scaling behaviour of the Rydberg excitation.

	$a_{R,Y}$	$b_{R,Y}$	$\nu_{R,Y}$
theory (1d)	$-{}^{84}/_{13} \simeq -6.46$	${}^{14}/_{13} \simeq 1.08$	${}^{14}/_{13} \simeq 1.08$
experiment (1d)	-6.50 ± 0.07	1.15 ± 0.12	1.08 ± 0.01
deviation (1d)	$0.5\,\sigma$ (0.6 %)	$0.6\,\sigma$ (6.8 %)	$0.3\,\sigma$ (0.3 %)
theory (3d)	$-{}^{12}/_{5} = -2.4$	${}^{6}/_{5} = 1.2$	${}^{6}/_{5} = 1.2$
experiment (3d)	-2.51 ± 0.08	1.20 ± 0.13	1.25 ± 0.03
deviation (3d)	$1.4\,\sigma$ (4.6 %)	$0\,\sigma$ (0 %)	$1.7\,\sigma$ (4.2 %)

	$a_{\mathrm{sat},Y}$	$b_{\mathrm{sat},Y}$	$\nu_{\mathrm{sat},Y}$
theory (1d)	$-{}^{12}/_{13} \simeq -0.92$	${}^{2}/_{13} \simeq 0.15$	${}^{2}/_{13} \simeq 0.15$
experiment (1d)	-0.92 ± 0.02	0.38 ± 0.03	0.16 ± 0.01
deviation (1d)	$0.2\,\sigma$ (0.3 %)	$7.5\,\sigma$ (150 %)	$0.6\,\sigma$ (4.0 %)
theory (3d)	$-{}^{4}/_{5} = -0.8$	${}^{2}/_{5} = 0.4$	${}^{2}/_{5} = 0.4$
experiment (3d)	-0.92 ± 0.02	0.38 ± 0.03	0.45 ± 0.01
deviation (3d)	$6.0\,\sigma$ (15 %)	$0.7\,\sigma$ (5.0 %)	$5.0\,\sigma$ (13 %)

Table 8.1.: Scaling exponents for the power law dependence of the Rydberg fraction during the linear increase $f_{R,Y} \sim n_Y^{a_{R,Y}} \Omega_0^{b_{R,Y}} \sim \alpha^{\nu_{R,Y}}$ of the excitation and in the saturation regime $f_{\mathrm{sat},Y} \sim n_Y^{a_{\mathrm{sat},Y}} \Omega_0^{b_{\mathrm{sat},Y}} \sim \alpha^{\nu_{\mathrm{sat},Y}}$ for magnetically trapped atoms. The dimensionless parameters are defined in equations (8.3) and (8.4) with $Y \in \{1\mathrm{d}, 3\mathrm{d}\}$ and represent the characteristics R and N_{sat} of the excitation curve shown in figure 8.3. The theoretical predictions of the scaling exponents can be obtained from equations (8.3) for $\nu_{R,Y}$ and (8.4) for $\nu_{\mathrm{sat},Y}$. The expected exponents a_Y and b_Y can be derived from table 3.1. The uncertainty (68 % confidence interval) of the measured exponent is given by σ. The relative deviations of the measured exponents to the theoretically expected exponents are given in brackets.

	$a_{R,Y}$	$b_{R,Y}$	$\nu_{R,Y}$
theory (1d)	$-{}^{84}/_{13} \simeq -6.46$	${}^{14}/_{13} \simeq 1.08$	${}^{14}/_{13} \simeq 1.08$
experiment (1d)	-6.43 ± 0.21	1.02 ± 0.13	1.06 ± 0.03
deviation (1d)	$0.2\,\sigma$ (0.5 %)	$0.4\,\sigma$ (5.3 %)	$0.6\,\sigma$ (1.6 %)
theory (3d)	$-{}^{12}/_{5} = -2.4$	${}^{6}/_{5} = 1.2$	${}^{6}/_{5} = 1.2$
experiment (3d)	-2.30 ± 0.11	1.02 ± 0.11	1.11 ± 0.04
deviation (3d)	$0.9\,\sigma$ (4.2 %)	$1.6\,\sigma$ (15 %)	$2.3\,\sigma$ (7.5 %)

	$a_{\mathrm{sat},Y}$	$b_{\mathrm{sat},Y}$	$\nu_{\mathrm{sat},Y}$
theory (1d)	$-{}^{12}/_{13} \simeq -0.92$	${}^{2}/_{13} \simeq 0.15$	${}^{2}/_{13} \simeq 0.15$
experiment (1d)	-1.01 ± 0.11	0.39 ± 0.07	0.20 ± 0.01
deviation (1d)	$0.8\,\sigma$ (9.4 %)	$3.4\,\sigma$ (150 %)	$4.6\,\sigma$ (30 %)
theory (3d)	$-{}^{4}/_{5} = -0.8$	${}^{2}/_{5} = 0.4$	${}^{2}/_{5} = 0.4$
experiment (3d)	-0.60 ± 0.04	0.42 ± 0.05	0.32 ± 0.02
deviation (3d)	$5.0\,\sigma$ (25 %)	$0.4\,\sigma$ (5.0 %)	$4.0\,\sigma$ (20 %)

Table 8.2.: Scaling exponents for the power law dependence of the Rydberg fraction during the linear increase $f_{R,Y} \sim n_Y^{a_{R,Y}} \Omega_0^{b_{R,Y}} \sim \alpha^{\nu_{R,Y}}$ of the excitation and in the saturation regime $f_{\mathrm{sat},Y} \sim n_Y^{a_{\mathrm{sat},Y}} \Omega_0^{b_{\mathrm{sat},Y}} \sim \alpha^{\nu_{\mathrm{sat},Y}}$ for atoms trapped in the ODT. The dimensionless parameters are defined in equations (8.3) and (8.4) with $Y \in \{1\mathrm{d}, 3\mathrm{d}\}$ and represent the characteristics R and N_{sat} of the excitation curve shown in figure 8.3. The theoretical predictions of the scaling exponents can be obtained from equations (8.3) for $\nu_{R,Y}$ and (8.4) for $\nu_{\mathrm{sat},Y}$. The expected exponents a_Y and b_Y can be derived from table 3.1. The uncertainty (68 % confidence interval) of the measured exponent is given by σ. The relative deviations of the measured exponents to the theoretically expected exponents are given in brackets.

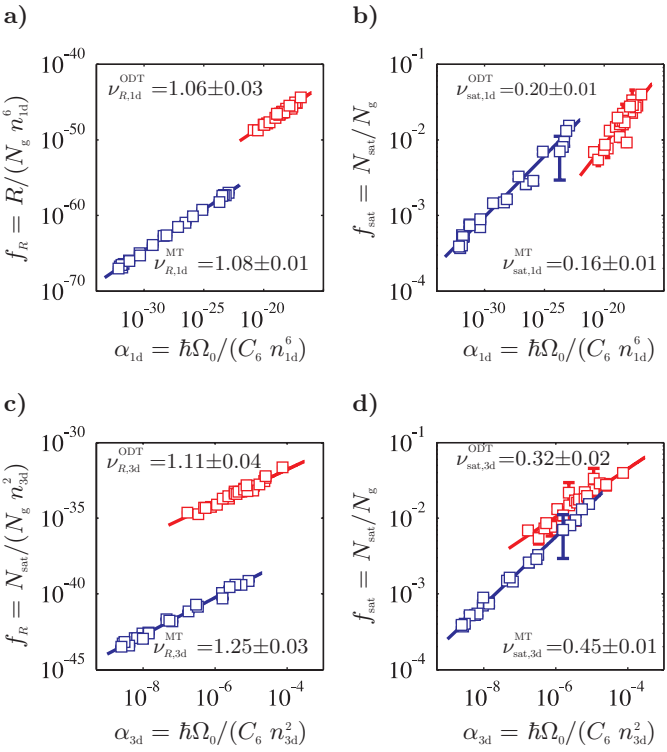

Figure 8.4.: Universal scaling of the two dimensionless parameters of the Rydberg fraction during the linear increase $f_{R,Y} \sim \alpha_Y^{\nu_{R,Y}}$ and in the saturation regime $f_{\mathrm{sat},Y} \sim \alpha_Y^{\nu_{\mathrm{sat},Y}}$ with $Y \in \{1\mathrm{d}, 3\mathrm{d}\}$ for atomic samples trapped magnetically (□) and in the ODT (□). The data are fitted with linear function in the logarithmic space.

8.3. Discussion and conclusion

The scaling of the initial slope R and the saturation value N_{sat} for magnetically trapped atoms is already investigated in [Hei08a]. The scaling drawn from this evaluation leads to the conclusion that the atomic sample in the magnetic trap has, under the given circumstances, a density distribution which is in between one and three dimensions. The evaluation of the scaling behaviour from this data are given in the first two columns of table 8.1 with the new dimensionless parameters. The scaling indicates, except for the scaling of $f_{\mathrm{sat}}(\Omega_0)$, a one dimensional rather than a three dimensional geometry of the atomic cloud.

For the measurements of the universal scaling of the normalised initial slope $f_R(\alpha)$ and in the saturation regime $f_{\mathrm{sat}}(\alpha)$ the parameter α is varied by 15 orders of magnitude. This assumes a one dimensional density distribution and four orders of magnitude assuming a three dimensional density distribution.

The evaluation of the data for f_R and f_{sat} presented in figure 8.4 shows an excellent agreement with a power law dependence on α, visible as a linear function in the double logarithmic depiction. The data for f_R especially shows a nearly perfect linear behaviour for the scaling with α in the double logarithmic space. Time dependent effects, e.g. linewidth of the laser and lifetime of the Rydberg state, become more prominent in the measurement of the scaling of f_{sat}. The scaling of the Rydberg fraction in the saturation regime shows a clear power law dependence for the scaling with α suggesting a universal scaling.

The exponents of the power law for this dependence are summarised and compared to the theoretically expected values in table 8.1 for magnetically trapped atoms and in table 8.2 for atoms trapped in an ODT for an assumed one or three dimensional density distribution.

The scaling behaviour of f_R and f_{sat} indicates again a one dimensional geometry for the magnetically trapped atomic sample since the deviation from the expected exponent in the one dimensional case is considerably smaller than in the three dimensional case.

The obersvation of the scaling behaviour of f_R and f_{sat} for atoms trapped in the ODT shows a deviation from the theoretically expected exponent for the α dependence of f_R that is smaller for a one dimensional density distribution. For the scaling behaviour of f_{sat} with α, however, the deviation with respect to the theoretical exponent is slightly smaller for a three dimension geometry of the atomic sample. A definite conclusion whether the scaling behaviour shows one or three dimensional exponents is not possible since both exponents show a rather large deviation from the theoretical expected value. Thus, the scaling behaviour of f_{sat} is still in between one and three dimensional.

This result is astonishing since the radial width of the atomic cloud has been decreased by roughly a factor of two going from the magnetic to the optical dipole trap. The stronger radial confinement of the atoms in the optical dipole trap is supposed to create a geometry which comes closer to the one dimensional situation than in the magnetic trap, but the contrary seems to be the case. Although the data shows a scaling in f_R, which suggests rather a one dimensional geometry, the difference in the scaling between the one and three dimensional case of this variable is not as significant as the difference in f_{sat}, namely only 10 %.

At this point it should be noted that the conclusion on the dimensionality includes only the observed critical exponent ν. Effects which also might disturb the observation of the true dimensionality are not included into this discussion because it would require a deeper theoretical and experimental understanding of the system, which will be the subject of further studies in the future.

The size of the blockade radius, with which the radial expansion of the atomic cloud has to be compared to determine the dimensionality of the density distribution is given by equation (3.19). According to this equation the blockade radius is on the order of 5 µm. The Gaussian width σ_r of the atomic cloud in the ODT calculated with equation (5.15) is 5.6 µm for a temperature of $T = 6.3\,\mu\mathrm{K}$ and a given potential depth $U_0 = 3.3 \times 10^{-28}\,\mathrm{J}$. The ratio $\sigma_\mathrm{r}/r_\mathrm{b}$ of the radial width of the atomic sample in comparison to the blockade radius could be used as a measure for the dimensionality, where a value smaller than one corresponds to a one dimensional distribution of superatoms. This ratio is $\simeq 1.7$ for the experiments shown with magnetically trapped atoms and between $\simeq 0.6$ and $\simeq 1.1$ for the experiments conducted in the optical dipole trap. From these considerations one expects to find a three dimensional distribution of Rydberg excitations in the magnetic trap and a rather one dimensional distriubtion of superatoms in the the ODT.

However, the density distribution is not sharply truncated at σ_r, which leads to an excitation of the atoms in the wings of the density distribution resulting in a three dimensional geometry. A better, though conservative, estimation of the cloud size takes the Gaussian shape of the combined optical potential and the potential due to the gravity into account. Adding both potentials results in an effective potential with a finite height at a radial distance r_f from the trap centre. For the given parameter of the ODT the atomic cloud could have a maximal radial extension of $r_\mathrm{f} = 30\,\mu\mathrm{m}$, which is much larger than the blockade radius and, thus, leads to the observation of three dimensional density distribution instead of the expected one dimensional shape of the atomic cloud.

Two approaches could in future experiments lead to a realisation of a purely one dimensional Rydberg system. Firstly, a focus of 3 µm with the given trap depth U_0 would result in a maximal radial extension of the atomic cloud of

r_f =5.3 µm leading to a purely one dimensional chain of superatoms. The numerical aperture of the main chamber in the direction of the ODT is 0.28 [Löw06], which allows foci down to a waist of ≃1.5 µm. The realisation of such small foci, however, requires special optics to maintain the optical quality of the Gaussian beam. The transfer of the atoms from the magnetic trap into such an ODT is constrained due to the mismatch of the potentials. This would result in a heating of the atomic sample and an increased atom loss during the transfer.

The second approach to tailor the dimensionality if the system is to use the posibility of changing the blockade radius by altering the principal quantum number of the Rydberg state. According to table 2.1 the C_6 coefficient scales with principal quantum number as n^{11}, while the transition dipole matrix element for the $5\mathrm{P}_{3/2}$to nS transition scales with $n^{-1.5}$. Hence, the blockade radius $r_\mathrm{b} = (C_6/\hbar\Omega)^{1/6}$ scales roughly like n^2. Going from the current Rydberg state with $n = 43$ to $n = 104$ would result in a blockade radius on the order of 30 µm and, thus, the realisation of a purely one dimensional system of Rydberg atoms using the currently implemented optical dipole trap.

To conclude, it is shown that the characteristics of the Rydberg excitation, namely the normalised initial slope f_R and in the saturation regime f_sat, shows an algebraic behaviour with the dimensionless parameter α. This scaling behaviour is direct evidence of universality of the scaling in the critical region depicted in figure 4.2 a) of the Rydberg excitation. The appearance of a universal scaling is evidence that the driven Rydberg system exhibits a second order quantum phase transition due to the interaction and the formation of collective states.

Furthermore, the dependence of the Rydberg excitation on the dimensionality was investigated. The critical exponents for the scaling of f_R and f_sat with α for magnetically trapped atoms showed a good agreement with the predictions for the theoretical expected exponents assuming a one dimensional density distribution. The critical exponent measured with atoms trapped in the ODT has been inconclusive since the scaling of f_R with α indicates a one dimensional geometry and the scaling of f_sat indicates a rather three dimensional density distribution. The observation of the scaling of f_R and f_sat with the atomic ground state peak density and the single atoms Rabi frequency showed in both cases a rather one dimensional scaling behaviour. In future experiments it might be possible to systematically investigate the dependence of the Rydberg excitation with the radial confinement of the cloud by either using a smaller focus for the optical dipole trap or by choosing a higher principal quantum number of the Rydberg state.

9. Coherence properties

In chapter 3 the coherent collective excitation of a dense sample of Rydberg atoms was discussed. Several proposals [Jak00, Luk01] have been made to use the blockade of the Rydberg excitation for the realisation of quantum gates. A fundamental requirement for such a quantum gate is the coherence of the qbits during the time needed to perform the gate operation. The Rydberg excitation in a strong interacting atomic sample was shown to be collective and coherent in [Hei07, Hei08a]. However, the proof of the coherent evolution established in these references is rather indirect by using the scaling laws of the excitation dynamics into the Rydberg states. The initial slope and the saturation value of the the Rydberg excitation curves follow simple power laws in the atomic ground state density and the single atom Rabi frequency.
The aim of this chapter is to produce a direct proof of the coherence in a strong interacting sample of Rydberg atoms. For this we use two different methods, namely a rotary echo sequence [Sol59, Rai08a] known from the research field of nuclear magnetic resonance in section 9.1 and the electromagnetically induced transparency in section 9.2.
The strong interactions between Rydberg atoms lead to a dephasing of the atomic states with respect to each other. The dephasing rates are investigated by studying the time dependence of the rotary echo signals and the line shape of electromagnetically induced transparency signals [Rai08b].

9.1. Rotary Echo

The results shown in chapter 8 and in [Hei07, Hei08a] state the coherent character of the Rydberg excitation: The initial rate R of the excitation curves scales with the single atom Rabi frequency Ω_0 or, in the collective regime, with $\Omega_0^{2(\beta+1)/(2\beta+1)}$ (see table 3.1).

A direct proof of the coherence can be given by a reversal of the excitation into the Rydberg state. Such echo sequences are widely used in the research field of nuclear magnetic resonance in various schemes. We chose the rotary echo sequence [Sol59, Rai08a], which was invented to overcome problems with inhomogeneous Rabi frequencies over the sample. This reflects exactly the situation in our experiments, where the collective Rabi frequency varies over the atomic cloud due to its dependence on the ground state density n_g.

The N-particle Hamilton operator describing the dynamics of the Rydberg excitation is given by equation (4.1)

$$\mathcal{H} = -\frac{\hbar\delta}{2}\sum_{i=1}^{N}\boldsymbol{\sigma}_z^{(i)} + \frac{\hbar\Omega}{2}\sum_{i=1}^{N}\boldsymbol{\sigma}_x^{(i)} + C_6\sum_{j<i}\frac{\mathcal{P}_{\mathrm{rr}}^{(i)}\mathcal{P}_{\mathrm{rr}}^{(j)}}{|\boldsymbol{r}_i - \boldsymbol{r}_j|^6}\,, \tag{9.1}$$

with the Pauli matrices $\boldsymbol{\sigma}^{(i)}$, the positions of the atoms $\boldsymbol{r}_i$ and the projector onto the Rydberg state $\mathcal{P}_{\mathrm{rr}}^{(i)}$.

This description of the system assumes an effective two-level atom with a two-photon detuning δ and a coupling Ω between the ground and the Rydberg state. A description as an effective two-level atom is accurate as long as the detuning δ_p of the two excitation lasers from the intermediate state $5\mathrm{S}_{1/2}(f = 2, m_f = 2)$ is large as discussed in section 1.8. In the experiment the detuning was $\delta_\mathrm{p} \simeq 2\pi \times 500\,\mathrm{MHz}$ from the intermediate state (see figure 1.4). Furthermore it is assumed that the Rydberg gas is frozen, i.e. the centre of mass motion of the atoms can be neglected. The problem simplifies even further if the two lasers for the two-photon transition are on two-photon resonance, i.e. the first term vanishes for $\delta = 0$. A dephasing due to a finite frequency linewidth of the excitation laser can be included by a time dependent detuning $\delta(t)$. Without van der Waals interaction the Hamilton operator simplifies to $\mathcal{H} = {}^1\!/_2\, N\hbar\Omega_0\boldsymbol{\sigma}_x$. The solution of the Schrödinger equation is then a system of independent atoms undergoing single atom Rabi oscillations. If the van der Waals interaction becomes large compared to $\hbar\Omega$ the system will show the collective behaviour described in chapter 3.

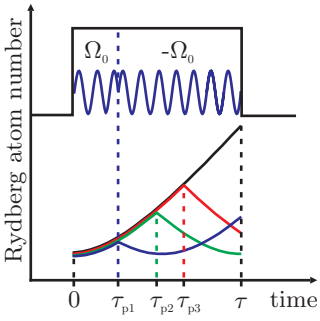

Figure 9.1.: Scheme of the rotary echo sequence. The atoms are excited for a time τ. After a time τ_p the phase of the excitation amplitude is reversed and the population is brought back to the ground state at $2\tau_\mathrm{p}$ if no dephasing occurred.

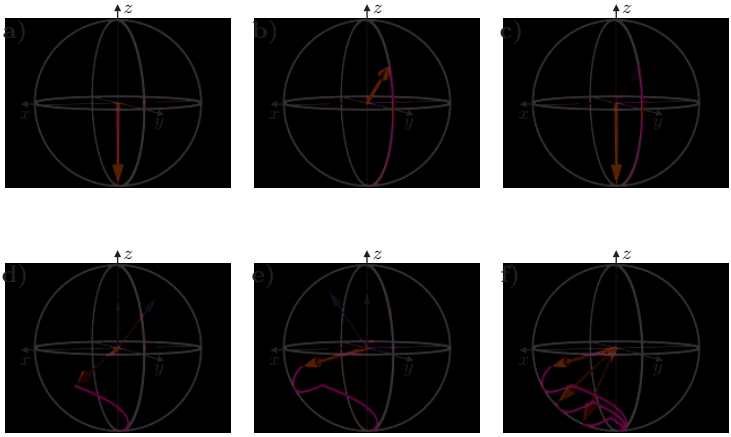

Figure 9.2.: Simple picture of the rotary echo experiment involving the Bloch sphere introduced in section 1.3. The top of the Bloch sphere refers to the state were all atoms inside the superatom are in the Rydberg state, while the bottom indicates their ground state. The Bloch vector (red) depicts the population difference (vertical direction) and the coherences between ground and Rydberg state (horizontal plane). Figures **a)** to **c)** show the noninteracting case, while figures **d)** to **f)** show the interacting case. **a)** At $t = 0$ all atoms are in the ground state. The orange arrow indicates the Rabi frequency Ω_0. **b)** At time $t = \tau/2$ the sign of the Rabi-frequency is changed. **c)** At time $t = \tau$ all atoms are back in the ground state. The faint arrows refer to the respective values before the phase flip. **d)** The interaction (grey arrow) is represented as a detuning and tilts the precession axis out of the vertical plane. **e)** After the phase flip the sign of Ω_0 is again reversed, while the interaction is constant. The population is not brought back to the ground state after $t = \tau$. **f)** Different superatoms contribute with different signals depending to their experienced interaction.

Figure 9.1 shows a schematic of the rotary echo sequence in which an atom is excited for a time τ using a square pulse with a rise time of $\leq 20\,\mathrm{ns}$. After a certain time $\tau_\mathrm{p} \leq \tau$ the sign of the excitation amplitude is changed from Ω_0 to $-\Omega_0$. The reversal of the sign of Ω_0 is done by a $180\,^\circ$ phase flip of the light field using the single pass AOM in the 480 nm beam (see figure 6.4). The corresponding circuit to flip the phase of the acoustic wave in the AOM is shown in figure C.2.

If no dephasing, e.g. due to the interaction between the Rydberg atoms or a finite linewidth of the laser, or decoherence, e.g. due to spontaneous decay of the Rydberg state, occurs during the time τ the complete population is completely reversed to the electronic ground state after a time $2\tau_\mathrm{p}$. The time evolution for the noninteracting case is shown in figures 9.2 a) to c) using the Bloch sphere, which was introduced in section 1.3. The figures 9.2 d) to f) give an intuitive picture for the time evolution of the Rydberg population during a rotary echo sequence in a strongly interacting Rydberg gas.

The coloured curves in figure 9.1 indicate the onset of the Rydberg excitation curve for which an expample is shown in figure 9.3 a) for magnetically trapped atoms at an atomic ground state peak density of $n_0 = 5.2 \times 10^{19}\,\mathrm{m}^{-3}$ and $\Omega_0 = 2\pi \times 91\,\mathrm{kHz}$. The size of the sample depends according to equation (5.9) only on the temperature and the trapping frequency. Since the temperature is constant when changing the atom number in the magnetic trap the sample is fully characterised by either the atomic ground state peak density or the number of atoms N_g in the ground state.

It is important to note that the rotary echo signal is expected to vanish for long excitation times in an atomic cloud with an inhomogeneous density distribution since every superatom accumulates a phase dependent on the position in the cloud due to the position dependent interaction between the Rydberg atoms (see figure 9.2 f)). The gathered phase due to the superatom-superatom interaction cannot be reversed, as the sign of the interaction between the Rydberg atoms cannot be reversed. Thus, the rotary echo cannot be observed in the saturation regime, i.e. for long excitation times, as every superatom will have accumulated a different phase. The understanding of these interactions requires a model beyond the simple superatom model, which does not account for any interaction between the superatoms. Such a beyond mean field approach for the description of the Rydberg excitation dynamics is under current theoretical investigation [Wei08].

Although the excitation times for the rotary echo were only several hundred nanoseconds, figure 9.3 b) shows that the van der Waals interaction strongly suppresses the excitation of Rydberg atoms. In the non-interacting case, i.e. the van der Waals interaction term in equation (9.1) is negligible, the number N_R of atoms in the Rydberg state would oscillate as depicted in figure 3.2 with

a Rydberg atom number given by

$$N_{\mathrm{R}} = N_{\mathrm{g}} \sin^2\left(\frac{1}{2}\Omega_0\tau\right) . \tag{9.2}$$

Hence, the expected exponent for the scaling of N_{R} with N_{g} is one. The upper black line in figure 9.3 b) shows the result of equation (9.2) $N_{\mathrm{R}} = 0.02N_{\mathrm{g}}$ for an excitation time $\tau = 478\,\mathrm{ns}$. In comparison, the data shows a dependence $N_{\mathrm{R}} \sim N_{\mathrm{g}}^{0.43\pm0.03}$ obtained from a fit to the data points in figure 9.3 b). Thus, a clear suppression of the Rydberg excitation is evident.

The lower black line in figure 9.3 b) takes a finite linewidth of the excitation laser into account. This frequency uncertainty can be included into equation (9.2) via a detuning δ. This results in an effective Rabi frequency $\Omega_{\mathrm{eff}} = \sqrt{\Omega_0^2 + \delta^2}$ and the Rydberg atom number is given by [Met99]

$$N_{\mathrm{R}} = N_{\mathrm{g}} \cdot \left(\frac{\Omega_0}{\Omega_{\mathrm{eff}}}\right)^2 \sin^2\left(\frac{1}{2}\Omega_{\mathrm{eff}}\,\tau\right) . \tag{9.3}$$

Since the laser is not detuned by a fixed δ, but drifting with a certain linewidth between the experiments it is necessary to average over all possible detunings. Assuming a weight function for the detuning of the form

$$f(\delta) = \frac{1}{\sqrt{2\pi}\delta_{\mathrm{lw}}}\,\mathrm{e}^{-\delta^2/2\delta_{\mathrm{lw}}^2} , \tag{9.4}$$

with a linewidth $\delta_{\mathrm{lw}} = 2\pi \times 1.5\,\mathrm{MHz}$ results in a dependence $N_{\mathrm{R}} = 0.01N_{\mathrm{g}}$ for $\tau = 478\,\mathrm{ns}$.

The reduction of the measured N_{R} with respect to the lower estimate for the single atom dynamics and the exponent of 0.43 ± 0.03 of the scaling with the atom number N_{g} in the ground state show that the experiments are done in the strong blockade regime. According to section 3.2 the strong interaction between the Rydberg atoms leads to the formation of collective states. In a first approximation the dynamics of the Rydberg excitation in a rotary echo sequence can be covered by a mean field model such as the superatom model described in section 3.3.

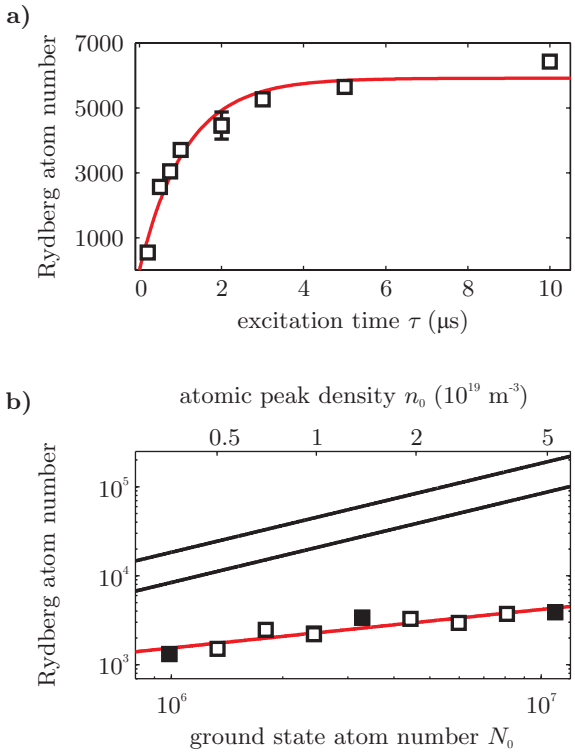

Figure 9.3.: **a)** Typical Rydberg atom numbers for different excitation times τ. The atomic ground state density is $n_g = 5.2 \times 10^{19}\,\mathrm{m}^{-3}$, i.e. $N_g = 1.1 \times 10^7$ atoms and $\Omega_0 = 2\pi \times 91\,\mathrm{kHz}$. The error bar indicates the statistical error due to the average over ten independent measurements. **b)** Rydberg atom number (□) as a function of the atom number in the ground state and the atomic ground state peak density n_0 (upper scale), respectively, for an excitation time of $\tau = 478\,\mathrm{ns}$. The red line is a fit to the data giving the dependence $N_R \sim N_g^{0.43\pm0.03}$. For the non-interacting case an exponent of one is expected. The non-interacting case is depicted by the black lines without a laser linewidth (upper line) and with a finite laser linewidth (lower line). The filled data points (■) indicate the atom numbers for which the rotary echo signals are shown in figure 9.5.

9.1.1. Rotary echo in the magnetic trap

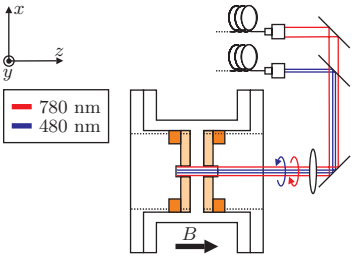

Figure 9.4.: Configuration used for the rotary echo measurements in the magnetic trap. Both excitation beams are colinear and copropagating. The 780 nm laser has a waist at the position of the atoms of 600 µm and is σ^+-polarised with respect to the quantisation axis pointing in the z-direction. The 480 nm laser has a waist of 42 µm and is σ^--polarised.

Figure 9.4 shows the configuration for the excitation light used for the measurements of the rotary echo with magnetically trapped atoms. A schematic setup to flip the phase of the 480 nm light by 180 ° and, thus, the excitation amplitude from Ω_0 to $-\Omega_0$ can be found in figure C.2.

Both excitation beams enter the main chamber colinear and copropagating. The 780 nm beam is collimated with a waist of 600 µm at the position of the atoms. The 480 nm beam is focused using an achromat in front of the chamber to a waist of 42 µm. The polarisation of both beams are chosen such that the Rabi frequency according to equation (1.24) is maximised. Hence, the 780 nm beam is σ^+ and the 480 nm is σ^--polarised with respect to the quantisation axis point in the z-direction. Using this stretched transition also minimises the unwanted population of the $43S_{1/2}(j = 1/2, m_j = -1/2)$ state through other transitions as depicted in figure 6.2.

In order to investigate the dependence of the rotary echo signal on the interaction $\mathcal{V}_{\mathrm{vdW}} \sim C_6 n_{\mathrm{g}}^2$ between the Rydberg atoms the atomic ground state density is varied by means of a Landau-Zener sweep to the state $5S_{1/2}(f = 1)$ (see section 5.3.3) which is unaffected by the excitation light. Using this technique the atomic peak density n_0 in the state $5S_{1/2}(f = 2, m_f = 2)$ is varied between $5.2 \times 10^{19}\ \mathrm{m}^{-3}$ without sweep and $0.4 \times 10^{19}\ \mathrm{m}^{-3}$ for a Landau-Zener sweep time of 400 ms. The temperature T=3.8 µK for the measurements in the magnetic trap is constant.

A useful measure to investigate the interaction effect on the evolution of the rotary echo signal is the visibility defined as [Mic91]

$$V = \frac{N_{\mathrm{R}}(\tau_{\mathrm{p}} = 0) - N_{\mathrm{R}}(\tau_{\mathrm{p}} = \tau/2)}{N_{\mathrm{R}}(\tau_{\mathrm{p}} = 0) + N_{\mathrm{R}}(\tau_{\mathrm{p}} = \tau/2)}\,. \tag{9.5}$$

Three typical rotary echo signals for different atomic ground state densities measured for a magnetically trapped atomic sample are shown in figure 9.5 for an excitation time of $\tau = 478$ ns. The effective single atom Rabi frequency Ω_0

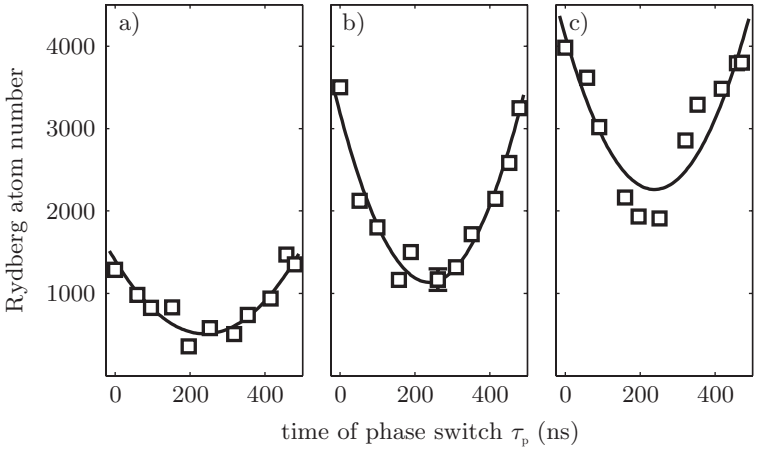

Figure 9.5.: Three typical rotary echo signals for different atomic ground state densities (see figure 9.3 b)) for an excitation time of $\tau = 478\,\mathrm{ns}$. The Rydberg atom number is according to the rotary echo scheme depicted in figure 9.1 a function of the time τ_p at which the sign of the excitation amplitude is flipped from Ω_0 to $-\Omega_0$. A fit with a parabolic function yields the visibility in figure **a)** $(47 \pm 8)\,\%$ with $n_0 = 0.4 \times 10^{19}\,\mathrm{m}^{-3}$, in figure **b)** $(48 \pm 5)\,\%$ with $n_0 = 1.5 \times 10^{19}\,\mathrm{m}^{-3}$ and in figure **c)** $(29 \pm 6)\,\%$ $n_0 = 5.2 \times 10^{19}\,\mathrm{m}^{-3}$. The effective single atom Rabi frequency was for all measurements $\Omega_0 = 2\pi \times 91\,\mathrm{MHz}$.

of $2\pi \times 91\,\mathrm{kHz}$ is calculated using equation (1.24) and (1.25) with a value for the Einstein-A coefficient of $A_{ba} = 5535\,\mathrm{s}^{-1}$, obtained by numerically calculating the overlap integral between the $5\mathrm{P}_{3/2}$ and $43\mathrm{S}_{1/2}$ state [Gra06]. A parabolic function is fitted to the data to obtain the visibility and to guide the eye. The correct functional dependence of the Rydberg atom number on τ_p is unknown and currently under theoretical investigation [Her08].

However, it is obvious that with increasing density (figure 9.5 a) to c)) the number of excited Rydberg atoms increases while the visibility decreases. Figure 9.6 shows the dependence of many of such visibility curves taken in the magnetic trap for two additional excitation times $\tau = 534\,\mathrm{ns}$ and $\tau = 659\,\mathrm{ns}$ for various densities of ground state atoms. Since the exact dependence on n_0 and τ is unknown the data points are again fitted with the most simple guess, here an exponential decay.

In section 9.3 the assumption of an exponential decay for the dependence of the visibility on the excitation time will be used to investigate the dephasing

of the atomic sample due to Rydberg-Rydberg interaction.

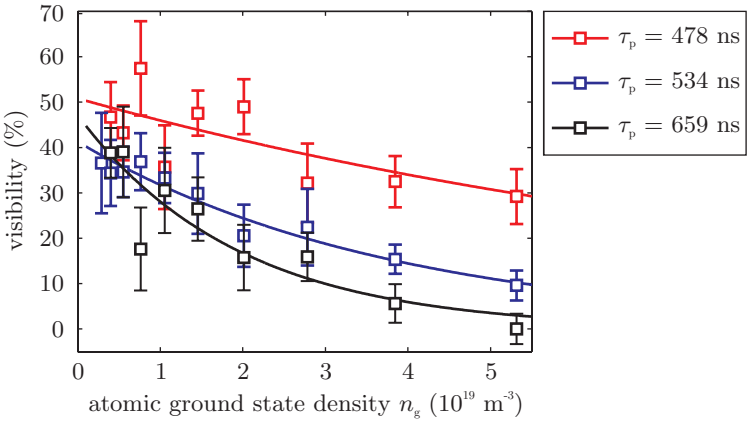

Figure 9.6.: Visibility as a function of the peak density of ground state atoms n_0 for three different excitation times. All three data sets were fitted with a simple exponential decay to guide the eye. The error bars are obtained from the parabolic fits to the data similar to those in figure 9.5.

9.1.2. Rotary echo in the optical dipole trap

Additionally to the rotary echo measurements in the magnetic trap the same sequence is performed with atoms in an optical dipole trap described in section 5.4. A strong confinement in radial direction leads to a one dimensional distriubtion of superatoms as discussed in chapter 8. The reduced number of next neighbours in a one dimensional arrangement reduces the dephasing due to the interaction between the superatoms and, hence, the visibility for a given pulse duration is higher.

According to equation (7.7) the optical density on the long axis of the ODT on resonance can be on the order of a thousand or even higher at atom numbers of $N_g \simeq 10^5$. Illuminating the atomic cloud along this axis would lead to an inhomogeneous distributed Rabi frequency over the sample as the 780 nm light would be absorbed. This problem is circumvented by the setup shown in figure 9.7. Since the radial width of the atomic cloud in the ODT is $\simeq$6 µm the optical density is $\simeq$5 on resonance along the radial direction of the atomic sample. For the rotary echo experiments the detuning from the intermediate $5P_{3/2}$ state is again $2\pi\times470$ MHz and the Rabi frequency can be assumed to be homogenous

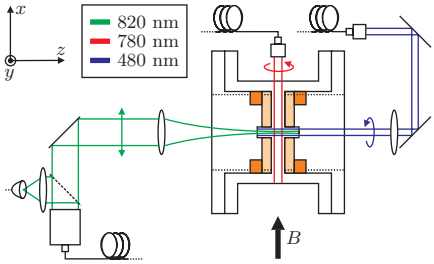

Figure 9.7.: Configuration used for the rotary echo measurements in the ODT. The 780 nm laser propagates along the -x-axis to overcome inhomogeneities in the Rabi frequency due to the high optical density on the long axis of the ODT. The 780 nm laser has a waist at the position of the atoms of $\simeq 1$ mm and is σ^+ polarised with respect to the quantisation axis pointing in the x-direction. The 480 nm laser has is focused to a waist of 42 µm and is σ^ℓ polarised.

over the atomic sample.

In order to use the stretched transition $5S_{1/2}(f = 2, m_f = 2)$ via $5P_{3/2}(f = 3, m_f = 3)$ a small magnetic offset field is applied along the x-axis. The 780 nm laser is σ^+-polarised with respect to B and has a waist of $\simeq$1 mm. The 480 nm laser is also circularly polarised, which leads, according to appendix B, to a reduction of the Rabi frequency for the transition from $5P_{3/2}(f = 3, m_f = 3)$ to $43S_{1/2}(j = 1/2, m_j = 1/2)$ by a factor of 1/2. The effective single atom Rabi frequency for the measurements of the rotary echo in the ODT is $\Omega_0 = 2\pi \times 71$ kHz.

The rotary echo experiment in the ODT is performed at temperatures between 5 µK and 8 µK. The widths of the atomic cloud in the ODT are $\sigma_r = 5.5$ µm and $\sigma_z = 500$ µm in radial and axial direction, respectively. The resulting atomic ground state densities are 3×10^{17} m^{-3} to 2×10^{18} m^{-3}. Figure 9.8 shows, similar to figure 9.6, the visibility as a function of the atomic ground state density for six different pulse durations. The data are again fit with an exponential decay to guide the eye.

For short excitation times ($\tau_p = 207$ ns) the visibility has a maximum value of 75 % and is not decreasing significantly if the atomic density of ground state atoms is varied. The dependence of the visibility on the atomic density shows for longer pulse durations roughly the same behaviour as in the magnetic trap. A clear signature of a reduced dimensionality due to the stronger confinement in radial direction is not visible. This result is in accordance with the observation of the dimensionality dependence of the scaling behaviour discussed in section 8.3 of the previous chapter.

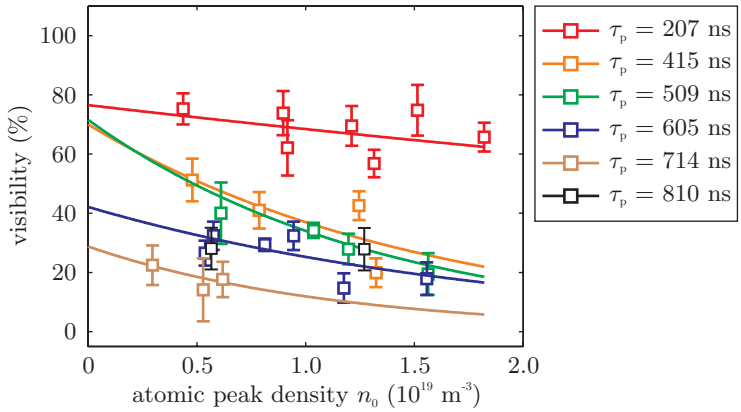

Figure 9.8.: Visibility of the rotary echo signal for atoms trapped in an ODT as a function of the peak density of ground state atoms n_0 for six different excitation times. All data sets were fitted with a simple exponential decay to guide the eye. The error bars are obtained from the parabolic fits to the data similar to those in figure 9.5.

The dephasing rates of the Rydberg state obtained from the dependence of the visbility on the pulse duration assuming an exponential decay (see figure 9.12) is investigated in section 9.3. The rotary echo experiment is simulated using the the Hamiltonian described in [Wei08]. A simpler mean field approach for the basic understanding of the rotary echo is given in the next section.

9.2. Electromagnetically induced transparency

The principles of electromagnetically induced transparency (EIT) were introduced in section 1.7. In this section the line shape of the EIT signal is used to investigate the dephasing of the Rydberg state due to the van der Waals interaction between the Rydberg atoms. The Liouville operator given by equation (1.31) takes additional dephasings of $|e\rangle$ and $|r\rangle$ into account. These dephasing do not change the population of the states, but affect the coherence between the states. The effect of the dephasing rates becomes important if their value is similar to the corresponding decay rate of the state as depicted in figure 1.6. Due to temperatures of $<10\,\mu K$ the motional degree of freedom of the atomic sample is frozen out on the timescale of $\leq 100\,\mu s$ of the experiments shown in this thesis. Hence, the dephasing due to collisions can be neglected. This

leads to the approximation of $\gamma_{\mathrm{ed}} = 0$. The dephasing rate γ_{rd}, however, is dominated by the Rydberg-Rydberg interaction and exceeds easily the decay rate of the Rydberg state, which is $\Gamma_{\mathrm{re}} \simeq 10\,\mathrm{kHz}$.

9.2.1. EIT of ultracold atoms

The susceptibility χ describes the response of an atom to an incident light field. The imaginary part of χ is connected to the absorption of the light and shows in the case of a three level atom the EIT features presented in figure 1.6.

Since it is experimentally difficult to directly measure χ a formula for obtaining the coherence properties from measurable quantities must be found. In our experiment we detect the atom number in the ground state using the absorption imaging scheme described in section 7.1. Thus, the coherence properties must be evaluated from these pictures.

The polarisation of the atomic sample is for a weak probe laser the linear response to the probe field and given by

$$P = \epsilon_0 \chi \mathcal{E}_0 = n p_{\mathrm{a}} \,, \tag{9.6}$$

with the particle density n and the polarisation per atom

$$p_{\mathrm{a}} = |d_{\mathrm{ge}}|\, \varsigma_{\mathrm{ge}} \,, \tag{9.7}$$

where $|d_{\mathrm{ge}}|$ is the dipole matrix element on the probe transition and ς_{ge} the coherence between the states $|\mathrm{g}\rangle$ and $|\mathrm{e}\rangle$. Hence, using equation (1.5) the susceptibility can be written as

$$\chi = \frac{n_{\mathrm{g}} |d_{\mathrm{ge}}|^2}{\epsilon_0 \hbar \Omega_{\mathrm{p}}} \varsigma_{\mathrm{ge}} \,, \tag{9.8}$$

with the atomic density of ground state atoms n_{g} and the dipole matrix element d_{ge}. The coherence ς_{ge} is a function of the two-photon detuning δ with an on-resonance value of $\varsigma_{\mathrm{eg},0}$. Measuring the fraction χ/χ_0 is equivalent to measuring $\varsigma_{\mathrm{ge}}/\varsigma_{\mathrm{eg},0}$.

The latter fraction can be obtained from the absorption images in the following way. For the sake of simplicity it is assumed without loss of generality that the coupling laser is off. The validity of the derived results if the coupling laser is on was tested by numerical calculations of the Lindblad master equation for the three-level atom (see MatLab program in appendix A.3). In the off-resonant case equation (7.7) must be modified by replacing σ_0 with $\sigma(\delta)$ from equation (7.3). The optical density $\mathbb{n}$ becomes

$$\mathbb{n}(\delta) = \frac{N_0}{2\pi\sigma_r\sigma_z} \cdot \sigma(\delta) \,. \tag{9.9}$$

On the other hand one obtains from an off-resonant absorption image according to equation (7.8) an atom number

$$N(\delta) = 2\pi\sigma_r\sigma_z \frac{\mathbb{n}(\delta)}{\sigma_0} \,. \tag{9.10}$$

Combining equations (9.9) and (9.10) leads to

$$\frac{N(\delta)}{N_0} = \frac{\sigma(\delta)}{\sigma_0} \,. \tag{9.11}$$

The definition of the scattering cross section given by equation (7.3) can be rewritten with the steady state solution of the two-level atom in equation (1.15)

$$\sigma(\delta) = \sigma_0 \frac{\Gamma_{\mathrm{eg}}}{\Omega_{\mathrm{p}}} \cdot \mathrm{Im}(\varsigma'_{\mathrm{ge}}(\delta)) \,. \tag{9.12}$$

Finally, inserting equation (9.12) into (9.11) leads to

$$\mathrm{Im}(\varsigma'_{\mathrm{ge}}) = \frac{\Omega_{\mathrm{p}}}{\Gamma_{\mathrm{eg}}} \cdot \frac{N(\delta)}{N_0} \,. \tag{9.13}$$

Hence, the absorptive part of the χ, namely the imaginary part $\mathrm{Im}(\chi) \sim \mathrm{Im}(\varsigma_{\mathrm{ge}})$ can be obtained in the steady state from the absorption images by dividing the off-resonant 'atom number' by the on-resonant atom number. In the case of electromagnetically induced transparency a certain number of the ground state atoms are excited to the Rydberg state and do not contribute to the coherhence ς_{eg}. Equation (9.13) must be corrected by this atom number and reads

$$\mathrm{Im}(\varsigma'_{\mathrm{ge}}) = \frac{\Omega_{\mathrm{p}}}{\Gamma_{\mathrm{eg}}} \cdot \frac{N(\delta)}{N_0 - N_{\mathrm{R}}^{\mathrm{max}}} \,, \tag{9.14}$$

with $N_{\mathrm{R}}^{\mathrm{max}}$ being the Rydberg atom number on two-photon resonance.

9.2.2. Experimental realisation

Figure 9.9 shows the details of the configuration used for the EIT measurements of optically trapped ultracold Rydberg atoms. The ODT to trap the atoms is described in section 5.4. The laser beam, which is usually used for the absorption imaging of the atomic sample is replaced by the 780 nm excitation laser for the Rydberg transition that is specially frequency stabilised with respect to the 480 nm laser (see section 6.2). The 780 nm excitation laser beam has a waist of 13 mm and is σ^+ polarised with respect to the quantisation axis pointing along the y-direction. A CCD camera in this direction detects the

780 nm light. The 480 nm laser beam for the upper transition has again a waist of 42 µm and is linearly polarised along the x-direction in order to optimise the Rabi frequency on the $5P_{3/2}(f = 3, m_f = 3)$ to $43S_{1/2}(j = 1/2, m_j = 1/2)$ transition.

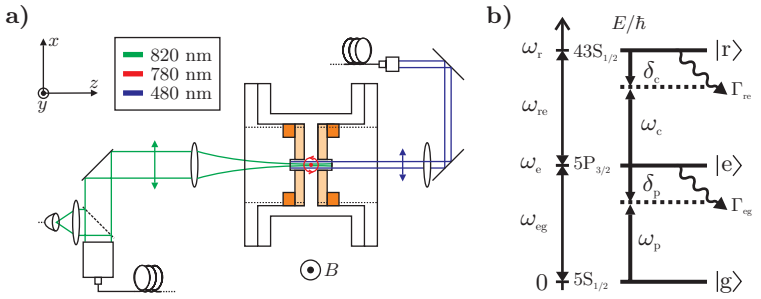

Figure 9.9.: **a)** Configuration used for the EIT measurements in the ODT. The 780 nm laser propagates along the y-axis and is detected using a CCD camera. The 780 nm laser has a waist at the position of the atoms of $\simeq 13$ mm and is σ^+ polarised with respect to the quantisation axis pointing in the y-direction. The 480 nm laser has a waist of 42 µm and is linearly polarised along x. **b)** Level scheme involving the ground state $5S_{1/2}(f = 2, m_f = 2)$, the intermediate state $5P_{3/2}(f = 3, m_f = 3)$ and the Rydberg state $43S_{1/2}(j = 1/2, m_j = 1/2)$ coupled by the probe (780 nm) and coupling laser (480 nm), respectively.

To measure the EIT signal with a high contrast $\simeq$50 % of the incident light should be absorbed by the atomic sample when the probe laser is on resonance. In order to decrease the atomic peak density of ground state atoms such that the optical density is on the order of 0.6 the atom number in the magnetic trap is lowered by means of a Landau-Zener sweep (see section 5.3.3) before loading the atoms into the ODT. Afterwards the atomic cloud is released from the ODT and freely expands for 100 µs. The loading into the ODT is only done to circumvent inhomogeneous magnetic fields during the switching of the currents of the magnetic trap due to eddy currents.

The temperature of the sample in the ODT is $T = 6.2\,\mu\mathrm{K}$ resulting in atomic peak densities of $n_0^{\max} = 5 \times 10^{17}\,\mathrm{m}^{-3}$ for 1 s Landau-Zener sweep time and a minimal value of $n_0^{\min} = 2 \times 10^{17}\,\mathrm{m}^{-3}$ for 4 s sweep time. After this preparation the cloud is excited for 100 µs during which the atomic density decreases further due to the free expansion to a value of $\simeq$50 % of the initial value.

The Rabi frequency for the 480 nm laser has a value of $\Omega_c = 2\pi \times 8\,\mathrm{MHz}$,

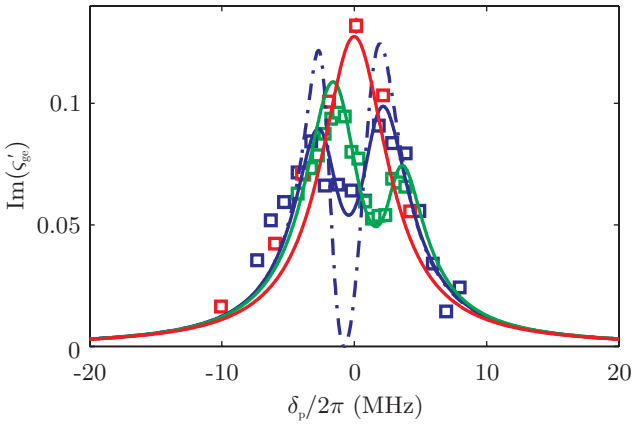

Figure 9.10.: Imaginary part of ς'_{ge} as a function of the detuning δ_p of the probe laser. The red curve is taken without the presence of a coupling laser, i.e. $\Omega_c = 0$. The absorption and, thus, $\mathrm{Im}(\varsigma'_{ge})$ decreases for $\delta_p \to 0$ if the coupling laser is on. $\mathrm{Im}(\varsigma'_{ge}) = 0$ is reached if no damping or dephasing occurs, i.e. $\gamma_{rd} = 0$ (dashed blue line). With a finite dephasing due to interaction between Rydberg atoms the depth of the dip decreases. The solid lines were calculated by numerically diagonalising equation (9.15) with $\Omega_p = 2\pi \times 800\,\mathrm{kHz}$, $\Omega_c = 2\pi \times 4.5\,\mathrm{MHz}$, $\gamma_{ed} = 0$ and $\gamma_{rd} = 2\pi \times 2.5\,\mathrm{MHz}$. The natural linewidth of $|e\rangle$ is $\Gamma_{eg} = 2\pi \times 6\,\mathrm{MHz}$ and the $43S_{1/2}$ Rydberg state $|r\rangle$ has a decay rate of $\Gamma_{re} = 2\pi \times 1.6\,\mathrm{kHz}$. Both blue lines are calculated with a detuning $\delta_c = 2\pi \times 0.75\,\mathrm{MHz}$ and the green line is calculated with $\delta_c = -2\pi \times 2.0\,\mathrm{MHz}$. The atomic density of ground state atoms is $n_0 = 2.4 \times 10^{17}\,\mathrm{m}^{-3}$.

which is again calculated using equation (1.24) and (1.25) and the Einstein-A coefficient calculated with the program described in [Gra06].

Figure 9.10 shows the observation of $\mathrm{Im}(\varsigma'_{eg})$ as a function of the probe detuning δ_p. The red data set is a reference scan of δ_p in the case of a blocked coupling laser, i.e. $\Omega_c = 0$. The result is the expected Lorentzian shaped absorption line of the atomic transition with a natural linewidth of $2\pi \times 6\,\mathrm{MHz}$ as described in section 1.7. The value for $\mathrm{Im}(\varsigma_{ge})$ can be calculated by solving the the Lindblad master equation

$$\dot{\varsigma} = -\frac{i}{\hbar}[\mathcal{H}, \varsigma] + \mathcal{L}_d(\varsigma)\,, \tag{9.15}$$

with the Hamilton operator from equation (1.30) and the dissipative Lindblad operator from equation (1.31). The theory curves in figure 9.10 are calculated

by diagonalising equation (9.15) using the MatLab program in appendix A.3. The Rabi frequency for the probe laser is $\Omega_\mathrm{p} = 2\pi \times 800\,\mathrm{kHz}$ for all theory curves.
Switching the coupling laser on results in a reduction of the coherence between the ground state $|\mathrm{g}\rangle$ and the intermediate state $|\mathrm{e}\rangle$ (see figure 1.6). Without dephasing and a Rabi frequency of the coupling laser of $\Omega_\mathrm{c} = 2\pi \times 4.5\,\mathrm{MHz}$ one would expect the dashed blue line with zero coherence between the ground and the intermediate state, i.e. $\mathrm{Im}(\varsigma'_\mathrm{ge}) = 0$, for $\delta_\mathrm{p} = 0$ corresponding to a maximal coherence of the states $|\mathrm{g}\rangle$ and $|\mathrm{r}\rangle$. With dephasing the coherence between $|\mathrm{g}\rangle$ and $|\mathrm{r}\rangle$ is smaller, i.e. $\mathrm{Im}(\varsigma'_\mathrm{ge}) \neq 0$ for $\delta_\mathrm{p} = 0$.

The calculation for the two data sets shown in blue and green in figure 9.10 includes a dephasing rate of the Rydberg state γ_rd accordinging to equation (1.31). The dephasing rate of the intermediate state γ_ed is $\simeq 0$ since dephasings due to collisions can be neglected. Furthermore the decay rates of the Rydberg state are $\Gamma_\mathrm{re} \simeq 0$ and $\Gamma_\mathrm{rg} = 0$. Additionally, the detuning of the coupling laser is taken into account by δ_c.

The Rabi frequency found for the coupling laser deviates from the calculated value by a factor of ~ 2. The considerations in [Hei08a] appendix B result in a prediction that the splitting Ω' in figure 1.5 increases with the coupling Rabi frequency according to $\sqrt{k}\Omega_\mathrm{c}$, where k is the number of atoms in the intermediate state $|\mathrm{e}\rangle$. The differential energy shift in the dressed atom picture, which is probed with the 780 nm light, reduces with $1/\sqrt{k}$. A simple picture is again given by the superatom model: The coupling to a state, which can only populated by one atom, cannot render all $N-1$ remaining members of the superatom transparent. As a result of the decreasing differential energy shift between the dressed states the transparency window of the EIT feature narrows, resulting in the observation of a smaller coupling Rabi frequency Ω_c.

For the investigation of the dephasing rates γ_rd it is useful to scan the detuning of the coupling laser through the two-photon resonance and keep the detuning of the probe laser fixed. With this method the Lorentzian absorption profile is removed from the data accentuating the EIT feature.

Figure 9.11 shows the corresponding measurements of the EIT feature that depends on the atomic ground state density and coupling Rabi frequencies. In order to obtain the dephasing rate the data are first fitted with the analytical function

$$\mathrm{Im}(\varsigma_\mathrm{eg}) = \frac{4\delta^2\Gamma_\mathrm{e} + \Gamma_\mathrm{r}\left(|\Omega_\mathrm{c}|^2 + \Gamma_\mathrm{e}\Gamma_\mathrm{r}\right)}{\left||\Omega_\mathrm{c}|^2 + \left(\Gamma_\mathrm{e} - 2i\delta_\mathrm{p}\right)\left(\Gamma_\mathrm{r} - 2i\delta\right)\right|^2} \cdot \Omega_\mathrm{p}\,, \tag{9.16}$$

which is the first order expansion in the probe Rabi frequency of the solution of equation (9.15). Thus, this equation is only valid in the regime where the probe laser is in comparison to the coupling laser a small perturbation. The

only free fit parameters in this function are the two-photon detuning δ and the rate $\Gamma_r = \Gamma_{re} + \gamma_{rd} \simeq \gamma_{rd}$. The value for the maximal coupling Rabi frequency is $\Omega_c = 2\pi \times 6.5\,\mathrm{MHz}$ and the rate $\Gamma_e = \Gamma_{re} + \gamma_{ed} \simeq \Gamma_{re}$. The probe Rabi

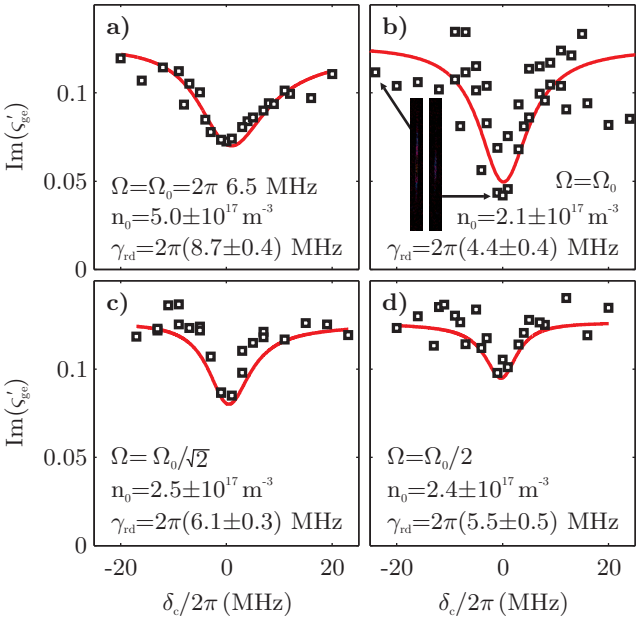

Figure 9.11.: Imaginary part of ς'_{ge} as a function of the detuning of the coupling laser δ_c. The data are normalised for $|\delta_c| \gg 0$ to the value of $\mathrm{Im}(\varsigma'_{eg})$ for $\Omega_c = 0$. The red lines show the numerically obtained solution of equation (9.15) with a probe Rabi frequency $\Omega_p = 2\pi \times 800\,\mathrm{MHz}$. The value of the coupling Rabi frequency is in figures **a)** and **b)** $\Omega_c^{max} = 2\pi \times 6.5\,\mathrm{MHz}$, in figure **c)** $\Omega_c^{max}/\sqrt{2}$ and in figure **d)** $\Omega_c^{max}/2$. The values for the calculation were obtained by prefitting the data with the function given in equation (9.16). The insets in figure **b)** show two typical absorption pictures of the atomic cloud for $\delta_c \neq 0$ (left) and $\delta_c = 0$ (right). The red and grey colour in these pictures corresponds to an optical density of 0.4 and 0, respectively.

frequency is held constant with respect to the measurement shown in figure 9.10 and has a value of $\Omega_p = 2\pi \times 800\,\mathrm{kHz}$.

The data in figure 9.11 shows a trend of the dephasing rate with the interaction between the Rydberg atoms. For the highest atomic ground state

peak density of $n_0 = 5.0 \times 10^{17}\,\mathrm{m}^{-3}$ the dephasing rate is about a factor of two larger than in the measurement with the lowest density. The dephasing rate is decreasing if the Rabi frequency decreases (see figures 9.11 e) and f)). Although the coupling Rabi frequcency is lower in these measurements the density was higher in comparison to the data shown in figure 9.11 b) and, thus, the interaction induced dephasing rates are higher. The values for the obtained dephasing rates are shown in figure 9.13 in the next section together with the results from section 9.1 and in comparison to the expected trend from a numerical simulation of the rotary echo.

9.3. Dephasing

This section aims to gather the dephasing rates of the Rydberg state from the measurements presented in section 9.1 on the rotary echo experiments and the EIT measurements in section 9.2. In the latter the dephasing rate $\gamma_\mathrm{d} = \gamma_\mathrm{rd}$ is obtained by investigating the imaginary part of the coherence between ground and intermediate state. Since $\mathrm{Im}(\varsigma'_\mathrm{ge})$ is a function of the dephasing rate the values could easily be found by fitting the data with the function given in equation (9.16).

In the case of the rotary echo, however, the dephasing rate is not obviously defined. This has two major reasons. The first is that the system in which the rotary echo is measured is not in the steady state. The Rydberg atom number increases linearly with the excitation time for the typical pulse lengths of $0 \leq \tau \leq 800\,\mathrm{ns}$ (see figure 9.3 a)) . The second reason for the lack of an obvious dephasing rate is nescience of the exact dependence of the visibility on the excitation time, which is currently a subject of theoretical investigation.

However, in order to find a measure for a dephasing rate one can assume in a zeroth order approximation that the visibility depends on the excitation time according to an exponential decay. Thus, the dephasing rate can be obtained by fits to the data with an exponential decay and using

$$\gamma_\mathrm{d} = -\frac{1}{\tau}\,\ln V \tag{9.17}$$

This function has been fitted to the data shown in figures 9.6 and 9.8. As an example the data from the measurements in the optical dipole trap are shown in figure 9.12 with two of the exponential fits.

The dephasing rates from the rotary echo measurements and those obtained from the EIT data are shown in figure 9.13 a) and b) as a function of the maximal Rydberg atom number N_R. The atom number $\max(N_\mathrm{R})$ is for the rotary echo measurements the Rydberg atom number without phase flip $N_\mathrm{R}(\tau_\mathrm{p} = 0)$ and for the EIT measurements the Rydberg atom number on two-photon resonance $N_\mathrm{R}(\delta = 0)$.

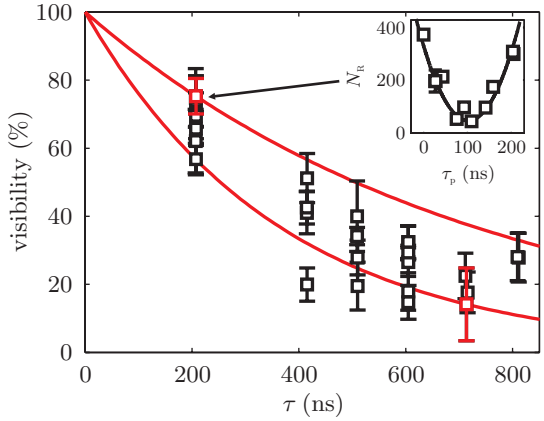

Figure 9.12.: Visibility of the rotary echo signal for an atomic sample trapped in the ODT as a function of the excitation time. One finds a measure for the dephasing rate assuming an exponential decay for the dependence of the visibility on the pulse duration. Two fits of an exponential decay are shown as examples in red. The inset shows a typical rotary echo signal for $\tau = 200\,\mathrm{ns}$ and $n_{\mathrm{g}} = 4.4 \times 10^{17}\,\mathrm{m}^{-3}$. A visibility of 75 % is obtained from a parabolic fit.

Additionally to the experimental data the rotary echo experiment is simulated by H. Weimer. The simulation takes the Hamilton operator from equation (4.1) on two-photon resonance, i.e. $\delta = 0$

$$\mathcal{H} = \frac{\hbar\Omega}{2} \sum_i \boldsymbol{\sigma}_x^{(i)} + C_6 \sum_{j<i} \frac{\mathcal{P}_{rr}^{(i)} \mathcal{P}_{rr}^{(j)}}{|\boldsymbol{r}_i - \boldsymbol{r}_j|^6}\,, \tag{9.18}$$

and numerically calculates the time evolution of N particles in a box with volume V_{b}. Since the size of the Hilbert space grows exponentially with the number of particles in the box the dipole blockade due to the van der Waals interaction between the Rydberg atoms is used to reduce the number of dimensions drastically. A detailed description of the simulation can be found in [Wei08]. The calculations are performed for $N = 44 \ldots 54$, $C_6/V_{\mathrm{b}}^2 = 0.01$ and $\Omega\tau_{\mathrm{p}} = 0.32 \ldots 0.74$. The sign of the excitation amplitude is again flipped from Ω to $-\Omega$ at the time τ_{p}. The treatment of the resulting rotary echo curves are the same as with the experimental data, i.e. the visibility is obtained by fitting a parabolic curve to the rotary echo signal. From the evolution of the visibility with the excitation time τ the dephasing rate is obtained from $\gamma_{\mathrm{d}} = -\ln(V)/\tau$. Figure 9.13 c) shows the results of the simulation.

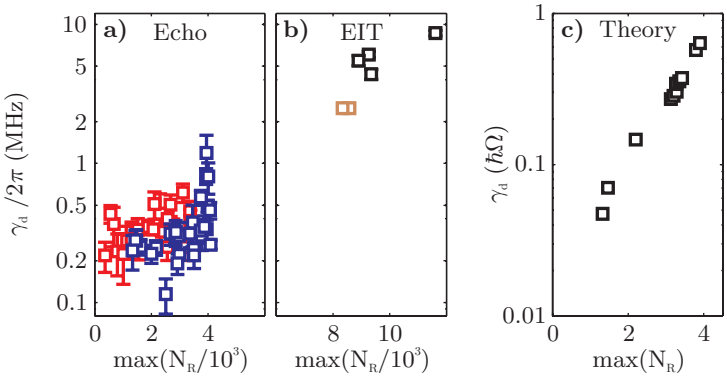

Figure 9.13.: Collection of the dephasing rates γ_d as a function of the maximal Rydberg atom number N_R. Figure **a)** shows the results from the rotary echo measurements in the magnetic trap (□) and in the optical dipole trap (□). Figure **b)** shows the dephasing rates $\gamma_d = \gamma_{rd}$ obtained from the EIT measurements presented in figure 9.10 (□) and figure 9.11 (□). Data from a simulation of the rotary echo sequence are shown in figure **c)**.

In section 6.2 it is pointed out that the two excitation laser have a frequency uncertainty on the minute timescale of $\simeq 2\pi \times 1.5\,\mathrm{MHz}$ with respect to each other. From the measurement shown in the inset of figure 9.12 an upper bound for the laser linewidth on the 100 ns timescale of $\simeq 2\pi \times 200\,\mathrm{kHz}$ can be found. The laser linewidth causes the same effect on the data as the dephasing due to the interaction does, namely it decreases the visibility of the signal. However, the 'dephasing' caused by instrumentation is much smaller than the observed additional dephasing due to the interaction between the Rydberg atoms. Both sets of data show the same trend of an increasing dephasing if the Rydberg atom number is increased. This observation is strengthened by the numerical simulation of the rotary echo experiment since these do not take any laser linewidth into account: Both, the experimental data sets and the calculation, reflect the same overall behaviour of the dephasing rate.

In order to study the dephasing of the sample of ultracold Rydberg atoms more quantitavely in future experiments the interaction could be tailored, e.g., by increasing the confinement of the atomic sample in radial direction. If the radial width becomes smaller than the blockade radius, i.e. the situation becomes purely one dimensional, the reduced number of next neighbours reduces the dephasing due to the reduced interaction. Conducting the experiments in an ODT with a tight radial confinement of the atomic cloud comes with the

advantage that the dimensionality is reduced in comparison to the confinement in the magnetic trap. Section 8.3 discusses the dimensionality issue on the example of the universal scaling. Since the numerical apertures of the vacuum chamber allow in principle much smaller foci than the currently implemented 21 µm waist of the optical dipole trap measurements of the coherence properties in a real one dimensional situation should be feasible in the future.

Part V.

Summary and Outlook

Summary

In summary, during the course of this work an existing experimental setup was modified in order to conduct measurements on the universal scaling behaviour as well as the coherence properties of ultracold Rydberg atoms.
Universal scalings can be found in the vicinity of a second order phase transition. Here the scaling behaviour of the Rydberg excitation of ultracold atoms was investigated dependent on the interaction and the dimensionality of the density distribution of the atomic sample. The data used for the investigation of the three dimensional scaling behaviour are published in reference [Hei07]. In order to change the density distribution from a three dimensional to a one dimensional geometry an optical dipole trap was set up.
The coherence properties of strongly interacting ultracold Rydberg atoms have been investigated by using two different methods. For the measurements involving the rotary echo sequence a control over the phase of the excitation light was implemented to the experiment. This led to the observation of rotary echo signals, which were studied dependent on the interaction between the Rydberg atoms [Rai08a].
The second experiment to investigate the coherence properties of a sample of ultracold atoms that are excited into a Rydberg state involves electromagnetically induced transparency. This coherent effect in a three-level system was again studied dependent on the interaction by changing the atomic density of ground state atoms and the Rabi frequency that couples the ground state and the Rydberg state. The resulting dephasing rates of the atomic sample in the Rydberg state were investigated for the rotary echo experiments as well as for the experiments involving electromagnetically induced transparency [Rai08b].

Universal scaling

Based on the work previously done by R. Heidemann [Hei08a] and the theory group of H. P. Büchler [Wei08] the first set of experiments presented in this thesis investigated the universal scaling behaviour in the driven Rydberg system. A second order quantum phase transition is predicted theoretically to be found in the Rydberg system. A second order phase transition manifests itself in the appearance of a universal scaling behaviour in a region around the critical point at which the phase transition happens. The usual experimental sequence that is used to excite ultracold Rydberg atoms takes place in this critical region. Hence, a universal scaling behaviour is reported in these experiments. The results presented in this work aimed at two goals, namely identifying a universal scaling behaviour and to investigate the dimensional dependence of the critical exponents ν. The critical exponents describe the system around the critical point of the phase transition as any important vari-

able of the system can be expressed in terms of a power law of the form α^{ν} with an dimensionless parameter α and the critical exponent ν. Moreover, the critical exponents are of special interest because they are universal. That means in every system that falls into the same universality class the same behaviour with the same exponents will be found.

In this thesis the characteristic dimensionless parameter α was the fraction $\mathcal{V}_{\mathrm{e}}/\mathcal{V}_{\mathrm{i}}$ comparing the excitation energy $\mathcal{V}_{\mathrm{e}} = \hbar\Omega$ with the van der Waals interaction energy $\mathcal{V}_{\mathrm{i}} = {}^{C_6}/_{r^6}$. The strong van der Waals interaction between the Rydberg atoms leads to a blockade of the Rydberg excitation. The excitation curves can therefore be described to some extent by an initial slope R and a saturation value N_{sat} to which the Rydberg atom number saturated for long excitation times. The variables of interest are the variables f_R and f_{sat} obtained from these characteristics of the Rydberg excitation curves. Both variables are dimensionless and show a scaling behaviour according to α^{ν_R} and $\alpha^{\nu_{\mathrm{sat}}}$ for f_R and f_{sat}, respectively.

In order to find a prediction for the expected values of the critical exponent ν the superatom model introduced in [Hei07, Hei08a] was used. The superatom model describes the atomic sample, that is exited to a Rydberg state in terms of collective states. These collective states are a result of the strong blockade due to the van der Waals interaction between the Rydberg atoms. The Rydberg energy levels of neighbouring atoms around one Rydberg atom are shifted out of resonance to the excitation lasers and a further excitation of atoms is blocked up to a interatomic distance r_{b}. For interatomic distances larger than the blockade radius r_{b} the power broadening exceeds the energy shift due to the interaction and further Rydberg excitation is possible. Due to symmetry reasons the atoms inside a sphere defined by the blockade radius collectively share the Rydberg excitation. This collective state is called superatom as it can be described like a simple two-level atom. The appearance of the collective state can be found by observing the scaling behaviour of the initial slope R of the Rydberg excitation dynamics.

The critical exponents ν in the vicinity of the second order quantum phase transition in the Rydberg system have been predicted by using the superatom model. Generally the critical exponent of the Rydberg system can be expressed in terms of the dimensionality d of the system and the power p of the r-dependence of the interaction. Thus, by investigating the critical exponent it is possible to unveil the dimensionality of the Rydberg excitation distribution inside the atomic sample and the type of the interaction between the Rydberg atoms. In the experiments presented in this thesis the dimensionality of the atomic sample was varied by confining the atoms either in a magnetic trap, resulting in a rather three dimensional density distribution, or in an optical dipole trap, in which the ratio between the blockade radius and the radial

size of the atomic sample was lowered by a factor of two in comparison to the magnetic trap. Both measurements showed a clear evidence for a universal scaling and the existence of second order quantum phase transition in the Rydberg system as the data depend on the parameter α with a power law. For these measurements α was varied up to 15 orders of magnitude by changing the atom number of the samples using a Landau-Zener sweep and by changing the laser power resulting in a change of the Rabi frequency of the coupling of the ground and the Rydberg state.

The investigation of the dependence of the critical exponent on the dimension of the density distribution of the atomic sample indicate that both, the magnetically trapped atoms as well as the atoms trapped in the optical dipole trap, behave rather as it is expected for a one dimensional density distribution. However, the data calls in some points for a further theoretical and experimental investigation as the scaling behaviour was not clearly reproduced by the superatom theory. In future experiments the dimensionality of the atomic sample can be further reduced using the experimental setup described in this thesis. This gives the ability to precisely characterise the physics in the critical region and the quantum phase transition of the Rydberg system in the future.

Coherence properties

The second part of the experimental results presented in this thesis dealt with the investigation of coherence properties of the interacting Rydberg system. For this observation basically two different methods were introduced. First, the rotary echo sequence, which is well known from the research field of nuclear magnetic resonance. It was used to investigate the dephasing of the atomic sample that is excited to the Rydberg state. In the rotary echo sequence the atomic sample was excited into the Rydberg state for a certain time τ_p after which the sign of the excitation was reversed. If no decoherence or dephasing occurs the complete population is reversed from the Rydberg state into the ground state at the time $2\tau_\mathrm{p}$. However, the investigated Rydberg systems in this thesis were shown to be strongly interacting. This leads to a dephasing of the atomic sample, which is measurable by observing the visibility of the rotary echo signal.

In this thesis the first systematic measurement of the dephasing of a sample of Rydberg atoms is presented by using the rotary echo sequence. The visibility of the rotary echo signal was investigated for magnetically trapped atoms as well as for atoms trapped in an optical dipole trap. Visibilities of 75 % were observed for atomic samples in an optical dipole trap. The excitation times were varied between 200 ns and 800 ns. In addition, the atomic density of ground state atoms was changed by means of a Landau-Zener sweep resulting in a change of the interaction between the Rydberg atom and, thus,

a systematic change of the dephasing of the atomic sample. Although the exact dependence of the visibility on the atomic density and the excitation time is unknown and under current theoretical investigation [Her08], a measure of the dephasing can be found by assuming an exponential decay of the visibility with an increasing excitation time. As naively expected the dephasing increases with an increasing number of Rydberg atoms. The results from the measurements of the dephasing using the rotary echo sequence were compared to a numerical calculation done by H. Weimer [Wei08]. This numerical simulations show the same overall behaviour of the dephasing with increasing Rydberg atoms number and, thus, confirm the conclusion drawn from the experimental data.

Another type of experiments that can be used to investigate the dephasing due to the interaction was introduced to the research field of Rydberg atoms in reference [Moh07]: The electromagnetically induced transparency. Electromagnetically induced transparency renders a medium transparent under certain conditions, namely at least two lasers must drive the transition between three levels of which one has a short lifetime in comparison to the other two. If one of the two lasers is weak, i.e. its Rabi frequency is small in comparison to the linewidth of the fast decaying state, and both lasers are on resonance the medium becomes transparent for this weak laser.

The degree of the transparency of the medium depends on the decoherence and the dephasing of the long-lived states. Hence, the observation of the electromagnetically induced transparency constitutes an excellent tool for the investigation of the dephasing of an atomic sample that has been excited to a Rydberg state.

For the experiments on electromagnetically induced transparency presented in this thesis a sample of ultracold ground state atoms was released from an optical dipole trap. After the release from the trap the atomic sample expanded freely for 100 µs and was than excited to the Rydberg state involving an fast decaying intermediate state. The detection of the weak probe beam on the lower transition led to the observation of a clear signal of electromagnetically induced transparency. This signal was systematically studied for different atomic densities and Rabi frequencies. The evaluation of the data showed again the same overall behaviour as in the rotary echo measurements, namely that an increasing number of Rydberg atoms led to an increasing dephasing of the atomic sample due to the interaction between the Rydberg atoms. These results are published in reference [Rai08b].

Outlook

From the technical point of view the experiment needs only minor changes to increase the stability and reliability of the setup. With the technical effort in the last years the experiment can be run on a everyday basis. However, a bigger issue which will be addressed in the near future is the stability of the Rydberg excitation laser system. Especially the linewidth on the long timescale, which is currently $\sim 1.5\,\mathrm{MHz}$ needs to be reduced in further experiments. For this purpose a ultrastable cavity will be used. This cavity is made of Zerodur, a glass ceramic with a thermal expansion coefficient of $\sim 10^{-8}\,\mathrm{K}^{-1}$. Additionally the cavity will be place in a ultrahigh vacuum chamber removing all disturbances of the environment. The long term stability is then expected to be on the order of 100 Hz.

The current experimental investigations successfully demonstrated the creation of molecules between a Rydberg atom and a ground state atom for the first time [Ben08]. These weakly bound molecules have been predicted in the references [Gre00, Gre06] to appear in samples of ultracold atomic sample that are excited to a Rydberg state. The ultralong range binding of the ground state atom to the Rydberg atom constitutes a novel type of binding and adds a fifth type to the well known covalent, ionic, hydrogen like and van der Waals bonds of molecules.

The fast evolving research field of ultracold Rydberg atoms makes it nearly impossible to predict the direction into which future experiments will go. The experimental setup presented in this thesis is specifically designed for investigation of ultracold Rydberg samples. Further studies of the coherence properties of the Rydberg system will be one of the first points on the agenda. Based on the experiences with the rotary echo experiment more elaborate sequences known from the research field of nuclear magnetic resonance can be implemented into the experimental setup. A sequence of two short pulses with a 180° phase flip of the excitation amplitude and a variable time between the two pulses would result in a direct observation of the dephasing of the atomic sample without the perturbing effects of the laser linewidth. Pulse sequences in which the detuning is changed during the second pulse such that the detuning caused by the interaction is compensated could lead to a higher visibility, i.e. to longer coherence times of the Rydberg sample.

Experiments in which the detuning is changed are also interesting from the theoretical point of view. Given the phase diagram presented in reference [Wei08] it is possible to adiabatically move from the ‘paramagnetic phase’ into the ‘crystalline phase’. With the current experimental sequence, where the light pulse is suddenly switched on, the system is projected to excited Rydberg state and, thus, the system is no longer in the ground state of the

corresponding Hamiltonian. By adiabatically changing the detuning and the laser power, i.e. the Rabi frequency, it is possible to keep the system in the ground state of the Hamiltonian and move the system to the desired point in the phase diagram. Using this method the phase diagram itself can be mapped.
Another fascinating idea is to use the coherence properties of Bose-Einstein condensates to study the distribution of Rydberg atoms in the atomic sample. This could for example be achieved by interferometric measurements. In a first approach the atoms from a BEC initially trapped in the $5S_{1/2}(f = 2, m_f = 2)$ state could be brought into a superposition of this state and the $5S_{1/2}(f = 1, m_f = 1)$ state. Afterwards the part of the atoms in the $5S_{1/2}(f = 2, m_f = 2)$ state are excited by the usual sequence discussed in this thesis into the Rydberg state. The Rydberg atom will gather a phase due to the interaction with other Rydberg atoms, which can be detected if the population is coherently reversed back to ground state using for example a pulse sequence analog to the rotary echo experiment. Interfering the matter waves will create a Mach-Zender interferometer and result in an spatial interference pattern, which structure is dependent on the accumulated phase. If the blockade radius is made much smaller than the spatial size of the atomic sample it should be feasible to obtain information about the spatial correlation function, i.e. the arrangement of the superatoms, in the atomic sample from these interference patterns.

A last idea for an experiment that might be realised in the future is the addressability of single sites in an optical lattice. The experimental setup discussed in this thesis is not only designed for the excitation of Rydberg atoms, but has also enough optical access to implement an optical lattice in up to three dimension. For a first experiment of the single site addressability the optical dipole trap that had been setup during my work on the experiment can be extended to a one dimensional optical lattice. Applying an electric field gradient using the eight capacitor plates over the atomic sample will create a position dependent energy shift of the Rydberg state. Given that this energy shift is large enough between to adjacent lattice sites a specific cite can be addressed by a laser with a reasonable small linewidth. This experiment would demonstrate a key ingredient for a quantum computer with neutral atoms, namely that a qbit can be separately addressed.

Part VI.

Appendix

A. MatLab programs

A.1. Calculation of the Rabi frequency

```
function [Omega,aPart]=RabiFreq(gs,es,I,Gamma,Int,omega,q)
% MatLab program for calculating the Rabi frequency
% ATTENTION: es MUST be the state with the higher energy!

if( nargin < 7 )
    disp('usage: [Omega,aPart] = ...
         RabiFreqETC(gs,es,I,Gamma,Int,omega,q');
    disp(sprintf('\n state = [l s j f mf] \n I: nuclear spin...
         \n Gamma: radiative life time \n Int: intensity \n ...
         omega: transition freuqency \n q: polarisation'));
    return;
end

% Constants
hbar = 1.05457e-34;
eps0 = 8.854e-12;
c = 299792458;

l = gs(1); s = gs(2); j = gs(3); f = gs(4); mf = gs(5);
lp = es(1); sp = es(2); jp = es(3); fp = es(4); mfp = es(5);

% Calculating the angular part and the Rabi-frequency
% according to eq. 1.24. This might be modified if one
% prefers to use the dipole matrix element in stead of Gamma
aPart = (-1)^(lp+s+I-mfp+1)*...
    sqrt((2*j+1)*(2*jp+1)*(2*f+1)*(2*fp+1))*...
    sqrt(2*lp+1)*...
    Wigner6j(lp,jp,s,j,l,1)*...
    Wigner6j(jp,fp,I,f,j,1)*...
    Wigner3j(f,1,fp,mf,q,-mfp);

Omega = aPart*sqrt(6*pi*c^2*Gamma*Int/(omega^3*hbar));

%% Used functions
%============================================================%
% Calculating the Wigner3j-Symbols
% Author: David Terr, Raytheon, 6-17-04
function wigner = Wigner3j(j1,j2,j3,m1,m2,m3)

% error checking
```

```
if ( 2*j1 ~= floor(2*j1) || 2*j2 ~= floor(2*j2) || ...
     2*j3 ~= floor(2*j3) || 2*m1 ~= floor(2*m1) || ...
     2*m2 ~= floor(2*m2) || 2*m3 ~= floor(2*m3) )
    error('All arguments must be integers or half-integers.');
end

% Additional check if the sum of the second row equals zero
if ( m1+m2+m3 ~= 0 ),
    disp('3j-Symbol unphysical');
    wigner = 0;
    return;
end

if ( j1 - m1 ~= floor ( j1 - m1 ) )
    disp('2*j1 and 2*m1 must have the same parity');
    wigner = 0;
    return;
end

if ( j2 - m2 ~= floor ( j2 - m2 ) )
    disp('2*j2 and 2*m2 must have the same parity');
    wigner = 0;
    return;
end

if ( j3 - m3 ~= floor ( j3 - m3 ) )
    disp('2*j3 and 2*m3 must have the same parity');
    wigner = 0;
    return;
end

if j3 > j1 + j2 || j3 < abs(j1 - j2)
    disp('j3 is out of bounds.');
    wigner = 0;
    return;
end

if abs(m1) > j1
    disp('m1 is out of bounds.');
    wigner = 0;
    return;
end

if abs(m2) > j2
    disp('m2 is out of bounds.');
    wigner = 0;
    return;
end

if abs(m3) > j3
```

```
    disp('m3 is out of bounds.');
    wigner = 0;
    return;
end

t1 = j2 - m1 - j3;
t2 = j1 + m2 - j3;
t3 = j1 + j2 - j3;
t4 = j1 - m1;
t5 = j2 + m2;

tmin = max(0, max( t1, t2 ));
tmax = min(t3, min( t4, t5 ));

wigner = 0;

for t = tmin:tmax
    wigner = wigner+(-1)^t/(factorial(t)*factorial(t-t1)*...
         factorial(t-t2)*factorial(t3-t)*factorial(t4-t)*...
         factorial(t5-t));
end

wigner = wigner*(-1)^(j1-j2-m3)*sqrt(factorial(j1+j2-j3)*...
     factorial(j1-j2+j3)*factorial(-j1+j2+j3)/...
     factorial(j1+j2+j3+1)*factorial(j1+m1)*...
     factorial(j1-m1)*factorial(j2+m2)*factorial(j2-m2)*...
     factorial(j3+m3)*factorial(j3-m3));
%============================================================%

%============================================================%
% Calculating the Wigner6j-Symbols using the Racah-Formula
function WignerReturn = Wigner6j(j1,j2,j3,J1,J2,J3)

% Check that the js and Js are only integer or half integer
if (2*j1 ~= round(2*j1) || 2*j2 ~= round(2*j2) || ...
    2*j2 ~= round(2*j2) || 2*J1 ~= round(2*J1) || ...
    2*J2 ~= round(2*J2) || 2*J3 ~= round(2*J3))
    error('All arguments must be integers or half-ints.');
end;

% Check if the four triads ((j1 j2 j3),(j1 J2 J3),...
% (J1 j2 J3),(J1 J2 j3)) satisfy the triangular inequalities
if (abs(j1-j2) > j3 || j1+j2 < j3 || abs(j1-J2) > J3 || ...
         j1+J2 < J3 || abs(J1-j2) > J3 || J1+j2 < J3 || ...
    abs(J1-J2) > j3 || J1+J2 < j3 )
    disp('6j-Symbol is not triangular!');
    WignerReturn = 0;
    return;
end;
```

```
% Check if the sum of the elements of each traid is an integer
if (2*(j1+j2+j3)~=round(2*(j1+j2+j3)) || 2*(j1+J2+J3)~=...
        round(2*(j1+J2+J3)) || 2*(J1+j2+J3) ~= ...
        round(2*(J1+j2+J3)) || 2*(J1+J2+j3) ~= ...
        round(2*(J1+J2+j3)))
    disp('6j-Symbol is not triangular!');
    WignerReturn = 0;
    return;
end;

% Arguments for the factorials
t1 = j1+j2+j3;
t2 = j1+J2+J3;
t3 = J1+j2+J3;
t4 = J1+J2+j3;
t5 = j1+j2+J1+J2;
t6 = j2+j3+J2+J3;
t7 = j1+j3+J1+J3;

% Finding summation borders
tvec = [ t1 t2 t3 t4 t5 t6 t7 ];
tmin = max(0, max(t1, max(t2, max(t3,t4))));
tmax = min(t5, min(t6,t7));

% Calculation the sum part of the 6j-Symbol
WignerReturn = 0;
for t = tmin:1:tmax,
    WignerReturn = WignerReturn+(-1)^t*factorial(t+1)/( ...
        factorial(t-t1)*factorial(t-t2)*factorial(t-t3)* ...
        factorial(t-t4)*factorial(t5-t)*factorial(t6-t)* ...
        factorial(t7-t));
end

% Calculation of the 6j-Symbol
WignerReturn = WignerReturn*sqrt(TriaCoeff(j1,j2,j3)* ...
           TriaCoeff(j1,J2,J3)*TriaCoeff(J1,j2,J3)* ...
           TriaCoeff(J1,J2,j3));
%============================================================%

%============================================================%
% Calculating the triangle coefficient
function tc = TriaCoeff(a,b,c)

tc = factorial(a+b-c)*factorial(a-b+c)*factorial(-a+b+c)/...
     (factorial(a+b+c+1));
%============================================================%
```

A.2. Calculation of the ac-Stark shift

```
% MatLab program for caluclating the Stark shift in 87Rb

% Constants
c = 299792458;
hbar = 1.05457e-34;
kb = 1.38065e-23;

% 87Rb properties
omegaD1 = 2*pi*377.107463e12;
GammaD1 = 2*pi*5.747e6;
omegaD2 = 2*pi*384.230484e12;
GammaD2 = 2*pi*6.066e6;
omegaL = 2*pi*c/lambda;
mass=1.443e-25;

% Dipole trap properties
lambda = 825.7e-9;  % laser wavelength
w0=20.8e-6; % waist of the dipole trap beam
M2 = 1.54;  % propagation constant
zR = pi*w0^2/lambda/M2; % Rayleigh range
T = 6.2e-6; % Temperature
P = 22.4e-3; % Power

% Ground state
gstate = [0 0.5 0.5 2 2];
I = 3/2;

% Polarisation (see Appendix B for details)
%qS=[-1 1]; % sigmaMinus sigmaPlus
 qS=0;      % linear

% Intensity
Int = 2*P/(pi*w0^2);

% Excited states of the D1 line
estateD1A = [];
lp = 1;
sp = 0.5;
jp = lp-sp;
for fpc = I-jp:1:I+jp
    for mfpc = -fpc:1:fpc
        estateD1A = [estateD1A; lp sp jp fpc mfpc];
    end
end;

% Excited states of the D2 line
estateD2A = [];
lp = 1;
```

```
sp = 0.5;
jp = lp+sp;
for fpc = I-jp:1:I+jp
    for mfpc = -fpc:1:fpc
        estateD2A = [estateD2A; lp sp jp fpc mfpc];
    end
end;

% If the light is sigmaMinus/sigmaPlus polarised the
% intensity of each component must be according to equation
% (B.8) multiplied by a factor 1/2
if qS~=0
    fInt = 0.5;
else
    fInt = 1;
end

% Stark shift
EStark = 0;
estateTD1 = [];
for k = 1:size(estateD1A,1)
    estate = estateD1A(k,:);
    for q=qS
        [Omega,aPart] = RabiFreq(gstate,estate,I,GammaD1,...
                                 fInt*Int,omegaD1,q);
        if aPart ~= 0
            estateTD1 = [estateTD1; estate];
        end
        EStark = EStark+hbar*Omega^2/(4*(omegaL - omegaD1));
    end
end

estateTD2 = [];
for k = 1:size(estateD2A,1)
    estate = estateD2A(k,:);
    for q=qS
        [Omega,aPart] = RabiFreq(gstate,estate,I,GammaD2,...
                                 fInt*Int,omegaD2,q);
        if aPart ~= 0
            estateTD2 = [estateTD2; estate];
        end
        EStark = EStark + hbar*Omega^2/(4*(omegaL-omegaD2));
    end
end

sigma0x = sqrt(kb*T*w0^2/(4*(-EStark)));
sigma0z = sqrt(kb*T*zR^2/(2*(-EStark)));
```

A.3. Calculation of the three-level atom

```
function ergOut = ThreeLevelAtom(D,par)
% MatLab program for the calculation of the 3-level atom
% (|1> - |2> - |3>) using the Lindblad master equation
% given in (1.11)
%
% Usage (input parameters):
% D = [D1; D2]
%  D1: detuning first transition; row vector
%  D2: detuning second transition; row vector
%
% par = [O1 G2 O2 G3 Gd2 Gd3 time]
%  O1: Rabi frequency first transition
%  G2: lifetime |2>
%  O2: Rabi frequency second transition
%  G3: lifetime |3> ( G3 << G2 )
%  Gd2: additional dephasing only on the (12) offdiagonal
%       elements of the Liouville operator
%  Gd3: additional dephasing on the (23) and (13) offdiag.
%       elements of the Liouville operator
%  time: excitation time
%
% Output: ergOut = [D1 D2 rho[11 12 ... 33]]

D1 = D(1,:);
D2 = D(2,:);

if sum(D1-D1(1)*ones(1,size(D1,2))) == 0
    D1 = D1(1);
end
if sum(D2-D2(1)*ones(1,size(D2,2))) == 0
    D2 = D2(1);
end

O1 = par(1); G2 = par(2);
O2 = par(3); G3 = par(4);
Gd2 = par(5);
Gd3 = par(6);
time = par(7);

% Preparation of all atoms in the ground state
C0=[1; zeros(8,1)];

ergOut = zeros(size(D1,2)*size(D2,2),11);
j=1;
for D1C = D1
    for D2C = D2

        % Hamilton operator
```

```
        H = [
            0       O1/2    0;
            O1/2    D1C     O2/2;
            0       O2/2    (D1C+D2C);
            ];

        % Representation of the Hamiltonian as a 9x9 matrix
        % for diagonalisation
        Hrho = kron(H,eye(3));
        rhoH = kron(eye(3),H');

        % Linblad operator (also 9x9 matrix)
        L = zeros(9,9);
        L(1,5) = G2;
        L(2,2) = -1/2*(G2 + Gd2);
        L(3,3) = -1/2*(G3 + Gd3);
        L(4,4) = -1/2*(G2 + Gd2);
        L(5,5) = -G2;
        L(5,9) = G3;
        L(6,6) = -1/2*(G2 + G3 + Gd2 + Gd3);
        L(7,7) = -1/2*(G3 + Gd3);
        L(8,8) = -1/2*(G2 + G3 + Gd2 + Gd3);
        L(9,9) = -G3;

        [HV,HD] = eig(-i*(Hrho-rhoH)+L);

        Z=diag(HD,0);

        % Calculation of the time evolution
        % Result is a 9x9 matrix, which rows contain the
        % density matrix entries: [D1 D1 rho_gg rho_ge ...]
        ergOut(j,:)=[D1C D2C (HV*diag(exp(Z*time))*...
                     inv(HV)*C0)'];
        j=j+1;
    end
end
```

B. Polarisation and light

The knowledge of the polarisation of the light with respect to the quantisation axis is crucial for the calculation of the electric dipole matrix elements and the resulting Rabi frequency given by equations (1.5) and (1.24). This chapter aims at lifting the confusion of the terms used to describe the polarisation with and without respect to the atom.

The electric field of the light is given by

$$\boldsymbol{E}(z',t) = \Re\left\{ \begin{pmatrix} E_{0x'} \\ E_{0y'}\,\mathrm{e}^{i\phi} \\ 0 \end{pmatrix} \mathrm{e}^{i(kz'-\omega t)} \right\} \tag{B.1}$$

where it is assumed that the plain wave is propagating along the z' direction with a frequency ω. The prime denotes the coordinate system of the light.

The phase ϕ determines the polarisation of the light:

1. $\phi = 2\pi \cdot m\,(m \in \mathbb{Z})$ results in linearly polarised light

2. $\phi = \pi/2 + 2\pi \cdot m\,(m \in \mathbb{Z})$ and $E_{0x'} = E_{0y'} = E_0/\sqrt{2}$ results in σ^{ℓ} circularly polarised light that describes a right handed screw when looking towards the light source. Hence, it rotates counterclockwise to the *left* and has a positive helicity.

3. $\phi = -\pi/2 + 2\pi \cdot m\,(m \in \mathbb{Z})$ and $E_{0x'} = E_{0y'} = E_0/\sqrt{2}$ results in σ^{r} circularly polarised light that describes a left handed screw when looking towards the light source. Hence, it rotates clockwise to the *right* and has a negative helicity.

It is important to note that unless a quantisation axis is chosen the polarisation of the light has no distinctive significance for the transitions in the atom driven by the electric field. The quantisation axis of the atom is given by a magnetic field $\boldsymbol{B} = B\hat{\boldsymbol{e}}_z$ along the z axis in the coordinate system of the atom (without prime). Modeling the atom according to the Lorentz-Lorenz atom model as harmonic oscillators as it is describes in the references [Lor80a, Lor80b] the differential equation for the motion of the electron reads

$$m\ddot{\boldsymbol{r}} + m\omega_0^2\boldsymbol{r} + e \cdot \boldsymbol{E} = 0\,, \tag{B.2}$$

with the atomic resonance frequency ω_0. Assuming a σ^{r} polarised electric field

$$\boldsymbol{E}(z,t) = \frac{E_0}{\sqrt{2}} \begin{pmatrix} \cos(kz - \omega t) \\ \sin(kz - \omega t) \\ 0 \end{pmatrix} , \tag{B.3}$$

propagating along the z-axis, e.g. $\boldsymbol{k} \parallel \hat{\boldsymbol{e}}_z$, one finds the solution

$$\boldsymbol{r} = \frac{eE_0}{\sqrt{2}m} \cdot \frac{1}{\omega^2 - \omega_0^2} \begin{pmatrix} \cos(kz - \omega t) \\ \sin(kz - \omega t) \\ 0 \end{pmatrix} . \tag{B.4}$$

Hence, the electron follows the electric field vector. In other words, if a right circularly polarised light wave propagates colinear with the magnetic field defining the quantisation axis the electron describes a screw in time and position with negative helicity: The light is σ^- polarised with respect to the atom. If the light is σ^ℓ polarised the light is called σ^+ polarised as the screw would have a positive helicity. Swapping the magnetic field would mean that σ^ℓ becomes σ^- with respect to the atom.

Light with σ^+ polarisation drives transitions in the atom with $\Delta m = +1$, where σ^- light drives transitions with $\Delta m = -1$, where m is the projection of the orbital momentum onto the quantisation axis. Such an assertion cannot be assigned in the case of σ^ℓ and σ^{r}! If the light is linearly polarised and this polarisation is *along* the quantisation the light is called π polarised and drives transitions with $\Delta m = 0$.

It is convenient to introduce a transformation matrix to transform from the (x, y, z)-system into the $(\sigma^-, \pi, \sigma^+)$-system, since this is the only system which has a meaning with respect to the atom. The transformation is given by

$$\begin{pmatrix} E^- \\ E^\pi \\ E^+ \end{pmatrix} = \boldsymbol{U} \begin{pmatrix} E_x \\ E_y \\ E_z \end{pmatrix} , \tag{B.5}$$

with the transformation matrix

$$\boldsymbol{U} = \frac{1}{\sqrt{2}} \begin{pmatrix} 1 & i & 0 \\ 0 & 0 & \sqrt{2} \\ -1 & i & 0 \end{pmatrix} , \tag{B.6}$$

and its inverse transformation

$$\boldsymbol{U}^{-1} = \frac{1}{\sqrt{2}} \begin{pmatrix} 1 & 0 & -1 \\ -i & 0 & -i \\ 0 & \sqrt{2} & 0 \end{pmatrix} , \tag{B.7}$$

If the light does not penetrate the atom colinear to the quantisation axis equation (B.5) becomes

$$\begin{pmatrix} E^- \\ E^\pi \\ E^+ \end{pmatrix} = \boldsymbol{U} \cdot \boldsymbol{D} \begin{pmatrix} E_x \\ E_y \\ E_z \end{pmatrix} , \tag{B.8}$$

with the coordinate transformation

$$\boldsymbol{D} = \begin{pmatrix} \hat{\boldsymbol{e}}_x \hat{\boldsymbol{e}}'_x & \hat{\boldsymbol{e}}_x \hat{\boldsymbol{e}}'_y & \hat{\boldsymbol{e}}_x \hat{\boldsymbol{e}}'_z \\ \hat{\boldsymbol{e}}_y \hat{\boldsymbol{e}}'_x & \hat{\boldsymbol{e}}_y \hat{\boldsymbol{e}}'_y & \hat{\boldsymbol{e}}_y \hat{\boldsymbol{e}}'_z \\ \hat{\boldsymbol{e}}_z \hat{\boldsymbol{e}}'_x & \hat{\boldsymbol{e}}_z \hat{\boldsymbol{e}}'_y & \hat{\boldsymbol{e}}_z \hat{\boldsymbol{e}}'_z \end{pmatrix} . \tag{B.9}$$

Example

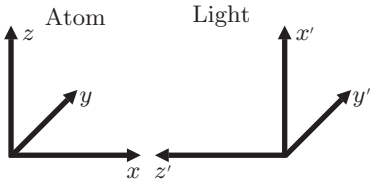

Figure B.1.: Illustration of the coordinate systems with respect to the atom and the light.

Assuming a left circular polarised light

$$\boldsymbol{E} = \frac{E_0}{\sqrt{2}} \Re \left\{ \begin{pmatrix} 1 \\ i \\ 0 \end{pmatrix} \right\} , \tag{B.10}$$

in the primed coordinate system shown in figure B.1 becomes with the coordinate transformation

$$\boldsymbol{D} = \begin{pmatrix} 0 & 0 & -1 \\ 0 & 1 & 0 \\ 1 & 0 & 0 \end{pmatrix} , \tag{B.11}$$

according to equation (B.8) a superposition of σ^+, σ^- and π light

$$\begin{pmatrix} E^- \\ E^\pi \\ E^+ \end{pmatrix} = \frac{E_0}{2} \begin{pmatrix} -1 \\ \sqrt{2} \\ -1 \end{pmatrix} \tag{B.12}$$

C. Electronics

C.1. Push-pull switch

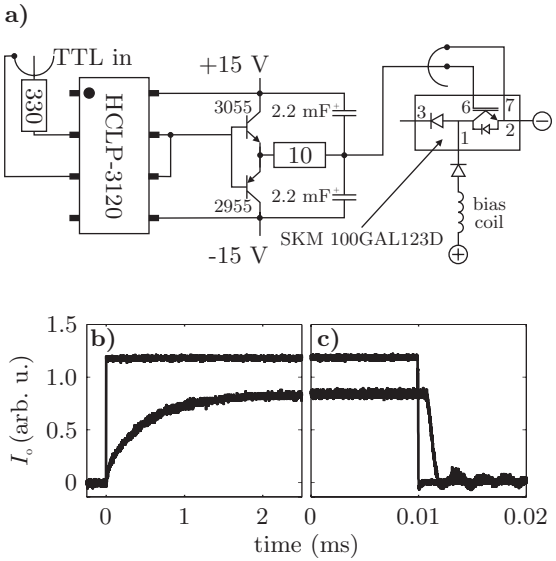

Figure C.1.: **a)** Circuit of the push-pull switch for switching small currents. This switch is used in the electrical setup of the magnetic trap (see figure 5.5). The ±15 V are provided by DC-DC converter (Traco Power TEL 3-1223), such that the computer control (TTL in) is separated from the experiment. The figure **b)** and **c)** show typical switching times for the current I_o through the bias coils to compensate the offset. The time of $\simeq 1.5$ ms for switching on the current might be limited by the power supply. The switching TTL is indicated by the upper signals.

C.2. Phase switch for AOMs

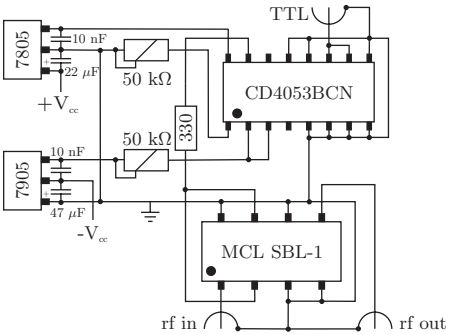

Figure C.2.: Schematic of the circuit used to flip the phase of the 480 nm laser by π using the single pass AOM depicted in figure 6.4.

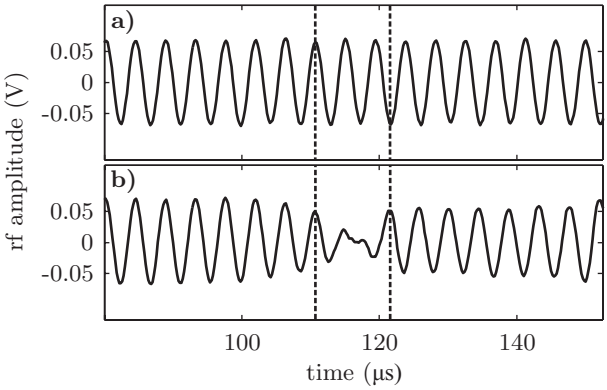

Figure C.3.: RF amplitude in figure **a)** without and in figure **b)** with π-phase flip. The frequency is 230 MHz.

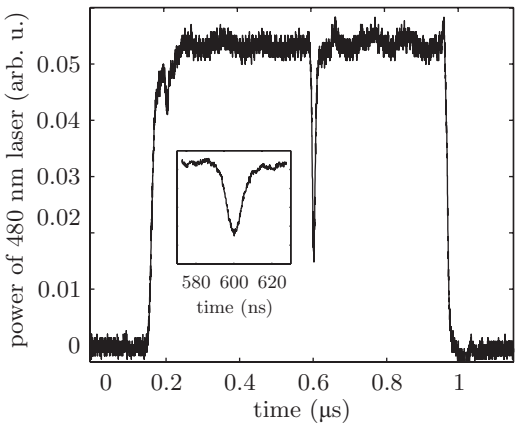

Figure C.4.: Example of a light pulse used in the rotary echo experiments. The inset shows a zoom to the break-in of the light pulse during the phase flip. The intensity breaks down for 20 ns.

Bibliography

The references are sorted by the name of the first author in alphabetical order. The last numbers of each reference denote the numbers of the pages on which the references are used.

[Alz76] Alzetta, G.; Gozzini, A.; Moi, L.; and Orriols, G.: An Experimental Method for the Observation of R. F. Transitions of Laser Beat Resonances in Oriented Na Vapour. *Nuovo Cimento*, 36 B(1):5 (1976). DOI: 10.1007/BF02749417. 39

[And98] Anderson, W. R.; Veale, J. R.; and Gallagher, T. F.: Resonant Dipole-Dipole Energy Transfer in a Nearly Frozen Rydberg Gas. *Phys. Rev. Lett.*, 80:249–252 (1998). DOI: 10.1103/PhysRevLett.80.249. 20

[Ari76] Arimondo, E. and Orriols, G.: Nonabsorbing Atomic Coherences by Coherent Two-Photon Transitions in a Three-Level Optical Pumping. *Lettere Al Nuovo Cimento*, 17(10):333 (1976). DOI: 10.1007/BF02746514. 39

[Ate07] Ates, C.; Pohl, T.; Pattard, T.; and Rost, J. M.: Many-body theory of excitation dynamics in an ultracold Rydberg gas. *Phys. Rev. A*, 76(1):013413 (2007). DOI: 10.1103/PhysRevA.76.013413. 55

[Aut55] Autler, S.; Townes, C.; Autler, S. H.; and Townes, C. H.: Stark Effect in Rapidly Varying Fields. *Phys. Rev.*, 100(2):703 (1955). DOI: 10.1103/PhysRev.100.703. 37

[Ben06] Bender, H.: *Mikrowellenanregung von ultrakalten Atomen*. Diploma thesis, Universität Stuttgart (2006). URL `http://www.pi5.uni-stuttgart.de/lehre/diplomarbeiten/bender.pdf`. 80

[Ben08] Bendkowsky, V.; Butscher, B.; Nipper, J.; Shaffer, J. P.; Löw, R.; and Pfau, T.: Novel binding mechanism for ultra-long range molecules. *In preparation* (2008). URL `http://arXiv.org/abs/0809.2961`. 145

[Ber98] Berthoud, P.; Joyet, A.; Dudle, G.; Sagna, N.; and Thomann, P.: A continuous beam of slow, cold cesium atoms magnetically extracted from a 2D magneto-optical trap. *Europhysics Letters*, 41(2):141–146 (1998). DOI: 10.1209/epl/i1998-00122-9. 69

[Bjo83] Bjorklund, G. C.; Levenson, M. D.; Lenth, W.; and Ortiz, C.: Frequency modulation (FM) spectroscopy. *Appl. Phys. B*, 32:145–152 (1983). DOI: 10.1007/BF00688820. 93

[Bol91] Boller, K.-J.; Imamoğlu, A.; and Harris, S. E.: Observation of electromagnetically induced transparency. *Phys. Rev. Lett.*, 66(20):2593–2596 (1991). DOI: 10.1103/PhysRevLett.66.2593. 39

[Bos24] Bose, S. N.: Plancks Gesetz und Lichtquantenhypothese. *Zeitschrift für Physik*, 26:178 (1924). URL `http://www.springerlink.com/content/j30330n763017620/fulltext.pdf`. 6, 17

[Bri07] Brion, E.; Pedersen, L. H.; and Mølmer, K.: Adiabatic elimination in a lambda system. *Journal of Physics A: Mathematical and Theoretical*, 40(5):1033–1043 (2007). DOI: 10.1088/1751-8113/40/5/011. 42

[But07] Butscher, B.: *Kollektive kohärente Anregung von ultrakalten Rydberg-Atomen*. Diplomarbeit, Universität Stuttgart (2007). URL `http://www.pi5.uni-stuttgart.de/diplomarbeiten/butscher.pdf`. 24

[Chi04] Chin, C.; Bartenstein, M.; Altmeyer, A.; Riedl, S.; Jochim, S.; Hecker Denschlag, J.; and Grimm, R.: Observation of the Pairing Gap in a Strongly Interacting Fermi Gas. *Science*, 305:1128 (2004). DOI: 10.1126/science.1100818. 20

[Chu98] Chu, S.: Nobel Lecture: The manipulation of neutral particles. *Rev. Mod. Phys.*, 70(3):685–706 (1998). DOI: 10.1103/RevModPhys.70.685. 6, 17

[Col07] Colombe, Y.; Steinmetz, T.; Dubois, G.; Linke, F.; Hunger, D.; and Reichel, J.: Strong atom-field coupling for Bose-Einstein condensates in an optical cavity on a chip. *Nature*, 450:272–276 (2007). DOI: 10.1038/nature06331. 21

[Cor02] Cornell, E. A. and Wieman, C. E.: Nobel Lecture: Bose-Einstein condensation in a dilute gas, the first 70 years and some recent experiments. *Rev. Mod. Phys.*, 74:875 (2002). URL `10.1103/RevModPhys.74.875`. 6, 17

[CT98] Cohen-Tannoudji, C. N.: Nobel Lecture: Manipulating atoms with photons. *Rev. Mod. Phys.*, 70(3):707–719 (1998). DOI: 10.1103/RevModPhys.70.707. 6, 17

[Cub05a] Cubel, T.; Teo, B. K.; Malinovsky, V. S.; Guest, J. R.; Reinhard, A.; Knuffman, B.; Berman, P. R.; and Raithel, G.: Coherent population transfer of ground-state atoms into Rydberg states. *Phys. Rev. A*, 72(2):023405 (2005). DOI: 10.1103/PhysRevA.72.023405. 21

[Cub05b] Cubel Liebisch, T.; Reinhard, A.; Berman, P. R.; and Raithel, G.: Atom Counting Statistics in Ensembles of Interacting Rydberg Atoms. *Phys. Rev. Lett.*, 95(25):253002 (2005). DOI: 10.1103/PhysRevLett.95.253002. 20

[Dal66] Dalgarno, A. and Davison, W. D.: The calculation of van der waals interactions. *Advances in ATOMIC, MOLECULAR, and OPTICAL PHYSICS*, 2:1 (1966). 7

[Dal83] Dalgarno, A.: Rydberg atoms in astrophysics. In R. F. Stebbins and F. B. Dunning (Editors), *Rydberg states of atoms and molecules*. Cambridge University Press (1983). 19

[Dal85] Dalibard, J. and Cohen-Tannoudji, C.: Dressed-atom approach to atomic motion in laser light: the dipole force revisited. *J. Opt. Soc. Am. B*, 2(11):1707 (1985). 33

[dB24] de Broglie, L.-V.: *Recherches sur la théorie des Quanta*. Ph.D. thesis, Faculte des Sciences de Paris (1924). 6, 17

[DeM98] DeMarco, B. and Jin, D. S.: Exploring a quantum degenerate gas of fermionic atoms. *Phys. Rev. A*, 58(6):R4267 (1998). DOI: 10.1103/PhysRevA.58.R4267. 17

[Die01] Dieckmann, K.: *Bose-Einstein Condensation with High Atom Number in a Deep Magnetic Trap*. Ph.D. thesis, Universiteit van Amsterdam (2001). URL `http://www.amolf.nl/publications/theses/dieckmann/dieckmann.pdf`. 75

[Dür00] Dür, W.; Vidal, G.; and Cirac, J. I.: Three qubits can be entangled in two inequivalent ways. *Phys. Rev. A*, 62(6):062314 (2000). DOI: 10.1103/PhysRevA.62.062314. 10, 21

[Ein24] Einstein, A.: Quantentheorie des einatomigen idealen Gases. *Sitzungsberichte der preussischen Akademie der Wissenschaften*, 71:463 (1924). 6, 17

[Ein25] Einstein, A.: Quantentheorie des einatomigen idealen Gases. Zweite Abhandlung. *Sitzungsberichte der preussischen Akademie der Wissenschaften*, p. 3 (1925). URL http://www.lorentz.leidenuniv.nl/history/Einstein_archive/Einstein_1925_publication/. 6, 17

[Fan61] Fano, U.: Effects of Configuration Interaction on Intensities and Phase Shifts. *Phys. Rev.*, 124(6):1866–1878 (1961). DOI: 10.1103/PhysRev.124.1866. 12, 41

[Fis98] Fisher, M. E.: Renormalization group theory: Its basis and formulation in statistical physics. *Rev. Mod. Phys.*, 70(2):653–681 (1998). DOI: 10.1103/RevModPhys.70.653. 22, 62

[Fle05] Fleischhauer, M.; Imamoglu, A.; and Marangos, J. P.: Electromagnetically induced transparency: Optics in coherent media. *Rev. Mod. Phys.*, 77:633–673 (2005). DOI: 10.1103/RevModPhys.77.633. 12, 37, 38

[Foo05] Foot, C. J.: *Atomic Physics*. Oxford University Press (2005). 75

[För48] Förster, T.: Zwischenmolekulare Energiewanderung und Fluoreszenz. *Annalen der Physik*, 437:55–75 (1948). DOI: 10.1002/andp.19484370105. 47

[Gal94] Gallagher, T. F.: *Rydberg Atoms*. Cambridge University Press (1994). 45, 46

[Gra06] Grabowski, A.: *Aufbau einer Messapparatur zur Laserkühlung und hochauflösende Rydberg-Spektroskopie an ^{87}Rb-Atomen*. Ph.D. thesis, Universität Stuttgart (2006). URL http://elib.uni-stuttgart.de/opus/volltexte/2006/2586/index.html. 45, 46, 124, 131

[Gre00] Greene, C. H.; Dickinson, A. S.; and Sadeghpour, H. R.: Creation of Polar and Nonpolar Ultra-Long-Range Rydberg Molecules. *Phys. Rev. Lett.*, 85(12):2458–2461 (2000). DOI: 10.1103/PhysRevLett.85.2458. 145

[Gre02] Greiner, M.; Mandel, O.; Esslinger, T. W.; Hänsch, T.; and Bloch, I.: Quantum phase transition from a superfluid to a Mott insulator in a gas of ultracold atoms. *Nature*, 415:39 (2002). DOI: 10.1038/415039a. 20

[Gre06] Greene, C. H.; Hamilton, E. L.; Crowell, H.; Vadla, C.; and Niemax, K.: Experimental Verification of Minima in Excited Long-Range Rydberg States of Rb_2. *Phys. Rev. Lett.*, 97(23):233002 (2006). DOI: 10.1103/PhysRevLett.97.233002. 145

[Gri00] Grimm, R.; Weidemüller, M.; and Ovchinnikov, Y. B.: Optical dipol traps for neutral atoms. *Advances in ATOMIC, MOLECULAR, and OPTICAL PHYSICS*, 42:95–170 (2000). URL `arXiv:physics/9902072`. 84

[Gug45] Guggenheim, E. A.: The Principle of Corresponding States. *The Journal of Chemical Physics*, 13(7):253–261 (1945). DOI: 10.1063/1.1724033. 8, 22, 62

[Han04] Hancox, C. I.; Doret, S. C.; Hummon, M. T.; Luo, L.; and Doyle, J. M.: Magnetic trapping of rare-earth atoms at millikelvin temperatures. *Nature*, 431(7006):281–284 (2004). DOI: 10.1038/nature02938. 47

[Har77] Harvey, K. C. and Stoicheff, B. P.: Fine Structure of the $nD2$ Series in Rubidium near the Ionization Limit. *Phys. Rev. Lett.*, 38(10):537–540 (1977). DOI: 10.1103/PhysRevLett.38.537. 19

[Har90] Harris, S. E.; Field, J. E.; and Imamoğlu, A.: Nonlinear optical processes using electromagnetically induced transparency. *Phys. Rev. Lett.*, 64:1107–1110 (1990). DOI: 10.1103/PhysRevLett.64.1107. 12, 39

[Hei07] Heidemann, R.; Raitzsch, U.; Bendkowsky, V.; Butscher, B.; Löw, R.; Santos, L.; and Pfau, T.: Evidence for Coherent Collective Rydberg Excitation in the Strong Blockade Regime. *Phys. Rev. Lett.*, 99(16):163601 (2007). DOI: 10.1103/PhysRevLett.99.163601. 7, 9, 10, 20, 21, 22, 24, 51, 103, 105, 106, 117, 141, 142

[Hei08a] Heidemann, R.: *Rydberg Excitation of Bose-Einstein Condensates: Coherent Collective Dynamics*. Ph.D. thesis, Universität Stuttgart (2008). URL `http://www.pi5.uni-stuttgart.de/dissertations/heidemann2008.pdf`. 7, 21, 22, 35, 37, 45, 55, 58, 59, 86, 92, 113, 117, 132, 141, 142

[Hei08b] Heidemann, R.; Raitzsch, U.; Bendkowsky, V.; Butscher, B.; Löw, R.; and Pfau, T.: Rydberg Excitation of Bose-Einstein Condensates. *Phys. Rev. Lett.*, 100(3):033601 (2008). DOI: 10.1103/PhysRevLett.100.033601. 51, 58

[Her08] Hernández, J. V. and Robicheaux, F.: Simulations using echo sequences to observe coherence in a cold Rydberg gas. *Journal of Physics B: Atomic, Molecular and Optical Physics*, 41(19):195301 (2008). DOI: 10.1088/0953-4075/41/19/195301. 124, 144

[Hua87] Huang, K.: *Statistical Mechanics*. John Wiley & Sons, 2 edition (1987). 8, 61, 62

[Jak00] Jaksch, D.; Cirac, J. I.; Zoller, P.; Rolston, S. L.; Côté, R.; and Lukin, M. D.: Fast Quantum Gates for Neutral Atoms. *Phys. Rev. Lett.*, 85(10):2208–2211 (2000). DOI: 10.1103/PhysRevLett.85.2208. 10, 21, 23, 45, 117

[Joh08] Johnson, T. A.; Urban, E.; Henage, T.; Isenhower, L.; Yavuz, D. D.; Walker, T. G.; and Saffman, M.: Rabi Oscillations between Ground and Rydberg States with Dipole-Dipole Atomic Interactions. *Phys. Rev. Lett.*, 100(11):113003 (2008). DOI: 10.1103/PhysRevLett.100.113003. 10, 22

[Ket02] Ketterle, W.: Nobel Lecture: When atoms behave as waves: Bose-Einstein condensation and the atom laser. *Rev. Mod. Phys.*, 74:1131 (2002). DOI: 10.1103/RevModPhys.74.1131. 6, 17

[Kil07] Killian, T. C.: Ultracold Neutral Plasmas. *Science*, 316:705– (2007). DOI: 10.1126/science.1130556. 20

[Knu06] Knuffman, B. and Raithel, G.: Emission of fast atoms from a cold Rydberg gas. *Phys. Rev. A*, 73(2):020704 (2006). DOI: 10.1103/PhysRevA.73.020704. 20

[Koc08] Koch, T.; Lahaye, T.; Metz, J.; Fröhlich, B.; Griesmaier, A.; and Pfau, T.: Stabilization of a purely dipolar quantum gas against collapse. *Nature Physics*, 4:218 (2008). DOI: 10.1038/nphys887. 18

[Kro04] Krohn, U.: *Aufbau einer UHV-Kammer zur Durchführung von Experimenten mit Bose-Einstein-Kondensaten in optischen Gittern*. Diplomarbeit, Universität Stuttgart (2004). URL `http://www.pi5.uni-stuttgart.de/lehre/diplomarbeiten/krohn2004.pdf`. 24, 69, 77

[Lan32] Landau, L. D.: On the theory of transfer of energy at collisions II. *Phys. Z. Sowjetunion*, 2:46 (1932). 80

[Li05] Li, W.; Tanner, P. J.; and Gallagher, T. F.: Dipole-Dipole Excitation and Ionization in an Ultracold Gas of Rydberg Atoms. *Phys. Rev. Lett.*, 94(17):173001 (2005). DOI: 10.1103/PhysRevLett.94.173001. 20

[Lor80a] Lorentz, H. A.: Ueber die Beziehung zwischen der Fortpflanzungsgeschwindigkeit des Lichtes und der Körperdichte. *Annalen der Physik*, 245:641–665 (1880). DOI: 10.1002/andp.18802450406. 157

[Lor80b] Lorenz, L.: Ueber die Refractionsconstante. *Annalen der Physik*, 247:70–103 (1880). DOI: 10.1002/andp.18802470905. 157

[Löw05] Löw, R.; Gati, R.; Stuhler, J.; and Pfau, T.: Probing the light-induced dipole-dipole interaction in momentum space. *Europhysics Letters*, 71:214–220 (2005). DOI: 10.1209/epl/i2005-10083-5. 18

[Löw06] Löw, R.: *A versatile setup for experiments with Rubidium Bose-Eintein condensates: From optical lattices to Rydberg matter*. Ph.d. thesis, Universität Stuttgart (2006). URL `http://www.pi5.uni-stuttgart.de/dissertations/loew2007.pdf`. 24, 69, 79, 80, 97, 115

[Löw07] Löw, R.; Raitzsch, U.; Heidemann, R.; Bendkowsky, V.; Butscher, B.; Grabowski, A.; and Pfau, T.: Apparatus for excitation and detection of Rydberg atoms in quantum gases (2007). URL `http://de.arxiv.org/abs/0706.2639`. *Preprint* arXiv:0706.2639v1. 69

[Lu96] Lu, Z. T.; Corwin, K. L.; Renn, M. J.; Anderson, M. H.; Cornell, E. A.; and Wieman, C. E.: Low-Velocity Intense Source of Atoms from a Magneto-optical Trap. *Phys. Rev. Lett.*, 77(16):3331–3334 (1996). DOI: 10.1103/PhysRevLett.77.3331. 69

[Luk01] Lukin, M. D.; Fleischhauer, M.; Cote, R.; Duan, L. M.; Jaksch, D.; Cirac, J. I.; and Zoller, P.: Dipole Blockade and Quantum Information Processing in Mesoscopic Atomic Ensembles. *Phys. Rev. Lett.*, 87(3):037901 (2001). DOI: 10.1103/PhysRevLett.87.037901. 10, 21, 23, 45, 117

[Mes08] Mestayer, J. J.; Wyker, B.; Lancaster, J. C.; Dunning, F. B.; Reinhold, C. O.; Yoshida, S.; and Burgdörfer, J.: Realization of Localized Bohr-Like Wave Packets. *Phys. Rev. Lett.*, 100(24):243004 (2008). DOI: 10.1103/PhysRevLett.100.243004. 19

[Met99] Metcalf, H. J. and van der Straten, P.: *Laser Cooling and Trapping*. Springer (1999). 30, 35, 72, 121

[Mey01] Meystre, P.: *Atom optics*. Springer (2001). 42, 72

[Mic91] Michelson, A. A.: Visibility of Interference-Fringes in the Focus of a Telescope. *Publication of the Astronomical Society of the Pacific*, 3:217–220 (1891). 123

[Moh07] Mohapatra, A. K.; Jackson, T. R.; and Adams, C. S.: Coherent Optical Detection of Highly Excited Rydberg States Using Electromagnetically Induced Transparency. *Phys. Rev. Lett.*, 98(11):113003 (2007). DOI: 10.1103/PhysRevLett.98.113003. 13, 22, 144

[Mou98] Mourachko, I.; Comparat, D.; de Tomasi, F.; Fioretti, A.; Nosbaum, P.; Akulin, V. M.; and Pillet, P.: Many-Body Effects in a Frozen Rydberg Gas. *Phys. Rev. Lett.*, 80(2):253–256 (1998). DOI: 10.1103/PhysRevLett.80.253. 20

[O'D00] O'Dell, D.; Giovanazzi, S.; Kurizki, G.; and Akulin, V. M.: Bose-Einstein Condensates with $1/r$ Interatomic Attraction: Electromagnetically Induced ıGravityȷ. *Phys. Rev. Lett.*, 84(25):5687–5690 (2000). DOI: 10.1103/PhysRevLett.84.5687. 18

[Pet02] Pethick, C. J. and Smith, H.: *Bose-Einstein Condensation in Dilute Gases*. Cambridge University Press (2002). 77

[Phi82] Phillips, W. D. and Metcalf, H.: Laser Deceleration of an Atomic Beam. *Phys. Rev. Lett.*, 48(9):596–599 (1982). DOI: 10.1103/PhysRevLett.48.596. 69

[Phi98] Phillips, W. D.: Nobel Lecture: Laser cooling and trapping of neutral atoms. *Rev. Mod. Phys.*, 70(3):721–741 (1998). DOI: 10.1103/RevModPhys.70.721. 6, 17

[Phi01] Phillips, D. F.; Fleischhauer, A.; Mair, A.; Walsworth, R. L.; and Lukin, M. D.: Storage of Light in Atomic Vapor. *Phys. Rev. Lett.*, 86(5):783–786 (2001). DOI: 10.1103/PhysRevLett.86.783. 21

[Pin97] Pinkse, P. W. H.; Mosk, A.; Weidemüller, M.; Reynolds, M. W.; Hijmans, T. W.; and Walraven, J. T. M.: Adiabatically Changing the Phase-Space Density of a Trapped Bose Gas. *Phys. Rev. Lett.*, 78(6):990–993 (1997). DOI: 10.1103/PhysRevLett.78.990. 77

[Pla01] Planck, M.: Über das Gesetz der Energieverteilung im Normalspectrum. *Annalen der Physik*, 309(3):553 (1901). 18

[Rai81] Raimond, J. M.; Vitrant, G.; and Haroche, S.: Spectral line broadening due to the interaction between very excited atoms: 'the dense Rydberg gas'. *Journal of Physics B: Atomic, Molecular and Optical Physics*, 14(21):L655–L660 (1981). DOI: 10.1088/0022-3700/14/21/003. 19

[Rai89] Raizen, M. G.; Thompson, R. J.; Brecha, R. J.; Kimble, H. J.; and Carmichael, H. J.: Normal-mode splitting and linewidth averaging for two-state atoms in an optical cavity. *Phys. Rev. Lett.*, 63(3):240–243 (1989). DOI: 10.1103/PhysRevLett.63.240. 21

[Rai08a] Raitzsch, U.; Bendkowsky, V.; Heidemann, R.; Butscher, B.; Löw, R.; and Pfau, T.: Echo Experiments in a Strongly Interacting Rydberg Gas. *Phys. Rev. Lett.*, 100(1):013002 (2008). DOI: 10.1103/PhysRevLett.100.013002. 11, 22, 117, 141

[Rai08b] Raitzsch, U.; Heidemann, R.; Bendkowsky, V.; Butscher, B.; Kollmann, P.; Löw, R.; and Pfau, T.: Investigation of dephasing rates in an interacting Rydberg gas. *In preparation* (2008). 117, 141, 144

[Rii90] Riis, E.; Weiss, D. S.; Moler, K. A.; and Chu, S.: Atom funnel for the production of a slow, high-density atomic beam. *Phys. Rev. Lett.*, 64(14):1658–1661 (1990). DOI: 10.1103/PhysRevLett.64.1658. 69

[RL08] Reetz-Lamour, M.; Deiglmayr, J.; Amthor, T.; and Weidemüller, M.: Rabi oscillations between ground and Rydberg states and van der Waals blockade in a mesoscopic frozen Rydberg gas. *New Journal of Physics*, 10(4):045026 (17pp) (2008). DOI: 10.1088/1367-2630/10/4/045026. 10, 22

[Rob00] Robinson, M. P.; Tolra, B. L.; Noel, M. W.; Gallagher, T. F.; and Pillet, P.: Spontaneous Evolution of Rydberg Atoms into an Ultracold Plasma. *Phys. Rev. Lett.*, 85:4466–4469 (2000). DOI: 10.1103/PhysRevLett.85.4466. 20

[Rob05] Robicheaux, F. and Hernández, J. V.: Many-body wave function in a dipole blockade configuration. *Phys. Rev. A*, 72(6):063403 (2005). DOI: 10.1103/PhysRevA.72.063403. 55

[Rub81] Rubbmark, J. R.; Kash, M. M.; Littman, M. G.; and Kleppner, D.: Dynamical effects at avoided level crossings: A study of the Landau-Zener effect using Rydberg atoms. *Phys. Rev. A*, 23:3107–3117 (1981). DOI: 10.1103/PhysRevA.23.3107. 80

[San00] Santos, L.; Shlyapnikov, G. V.; Zoller, P.; and Lewenstein, M.: Bose-Einstein Condensation in Trapped Dipolar Gases. *Phys. Rev. Lett.*, 85(9):1791–1794 (2000). DOI: 10.1103/PhysRevLett.85.1791. 18

[Sar93] Sargent III, M.; Scully, M. O.; and Lamb, Jr., W. E.: *Laser physics*. Westview Press (1993). 32

[Shi82] Shirley, J. H.: Modulation transfer processes in optical heterodyne saturation spectroscopy. *Optics Letters*, 7(11):537 (1982). URL http://ol.osa.org/abstract.cfm?URI=ol-7-11-537. 90

[Sin04a] Singer, K.: *Interactions in an ultracold gas of Rydberg atoms*. Ph.d. thesis, Albert-Ludwigs-Universität Freiburg (2004). URL http://www.freidok.uni-freiburg.de/volltexte/1664/pdf/KilianSingerDiss.pdf. 49

[Sin04b] Singer, K.; Reetz-Lamour, M.; Amthor, T.; Marcassa, L. G.; and Weidemüller, M.: Suppression of Excitation and Spectral Broadening Induced by Interactions in a Cold Gas of Rydberg Atoms. *Phys. Rev. Lett.*, 93(16):163001 (2004). DOI: 10.1103/PhysRevLett.93.163001. 7, 20

[Sin05] Singer, K.; Stanojevic, J.; Weidemüller, M.; and Côté, R.: Long-range interactions between alkali Rydberg atom pairs correlated to the ns ns, np np and nd nd asymptotes. *Journal of Physics B: Atomic, Molecular and Optical Physics*, 38:295 (2005). DOI: 10.1088/0953-4075/38/2/021. 7, 49

[Sol59] Solomon, I.: Rotary Spin Echoes. *Phys. Rev. Lett.*, 2:301–302 (1959). DOI: 10.1103/PhysRevLett.2.301. 11, 25, 117

[Ste01] Steck, D. A.: Rubidium 87 D Line Data (2001). URL http://steck.us/alkalidata. 83

[Sto03] Stockton, J. K.; Geremia, J. M.; Doherty, A. C.; and Mabuchi, H.: Characterizing the entanglement of symmetric many-particle spin-$\frac{1}{2}$ systems. *Phys. Rev. A*, 67(2):022112 (2003). DOI: 10.1103/PhysRevA.67.022112. 10, 21

[Str06] Streed, E. W.; Chikkatur, A. P.; Gustavson, T. L.; Boyd, M.; Torii, Y.; Schneble, D.; Campbell, G. K.; Pritchard, D. E.; and Ketterle, W.: Large atom number Bose-Einstein condensate machines. *Review of Scientific Instruments*, 77:3106 (2006). DOI: 10.1063/1.2163977. 71, 75

[Stu05] Stuhler, J.; Griesmaier, A.; Koch, T.; Fattori, M.; Pfau, T.; Giovanazzi, S.; Pedri, P.; and Santos, L.: Observation of Dipole-Dipole Interaction in a Degenerate Quantum Gas. *Phys. Rev. Lett.*, 95(15):150406 (2005). DOI: 10.1103/PhysRevLett.95.150406. 18, 47

[Ton04] Tong, D.; Farooqi, S. M.; Stanojevic, J.; Krishnan, S.; Zhang, Y. P.; Côté, R.; Eyler, E. E.; and Gould, P. L.: Local Blockade of Rydberg Excitation in an Ultracold Gas. *Phys. Rev. Lett.*, 93(6):063001 (2004). DOI: 10.1103/PhysRevLett.93.063001. 7, 20, 55

[Vli06] Vliegen, E. and F., M.: Stark deceleration of hydrogen atoms. *Journal of Physics B: Atomic, Molecular and Optical Physics*, 39(11):L241–L247 (2006). DOI: 10.1103/PhysRevA.76.023405. 19

[Vli07] Vliegen, E.; Hogan, S. D.; Schmutz, H.; and Merkt, F.: Stark deceleration and trapping of hydrogen Rydberg atoms. *Phys. Rev. A*, 76(2):023405 (2007). DOI: 10.1103/PhysRevA.76.023405. 19

[Vog06] Vogt, T.; Viteau, M.; Zhao, J.; Chotia, A.; Comparat, D.; and Pillet, P.: Dipole Blockade at Förster Resonances in High Resolution Laser Excitation of Rydberg States of Cesium Atoms. *Phys. Rev. Lett.*, 97(8):083003 (2006). DOI: 10.1103/PhysRevLett.97.083003. 7, 20

[Vul06] Vuletic, V.: Quantum networks: When superatoms talk photons. *Nature Physics*, 2:801–802 (2006). DOI: 10.1038/nphys469. 7, 21, 54

[Wea08] Weatherill, K. J.; Pritchard, J. D.; Abel, R. P.; Bason, M. G.; Mohapatra, A. K.; and Adams, C. S.: Electromagnetically induced transparency of an interacting cold Rydberg ensemble. *Journal of Physics B: Atomic, Molecular and Optical Physics*,

41(20):201002 (2008). URL http://stacks.iop.org/0953-4075/41/201002. 13

[Wei08] Weimer, H.; Löw, R.; Pfau, T.; and Büchler, H. P.: Quantum Critical Behavior in Strongly Interacting Rydberg Gases. *Phys. Rev. Lett.*, 101(25):250601 (2008). DOI: 10.1103/PhysRevLett.101.250601. 8, 22, 62, 103, 120, 127, 135, 141, 144, 145

[Wes04] West, G. B. and Brown, J. H.: Life's Universal Scaling Laws. *Physics Today*, 57(9):36–42 (2004). DOI: 10.1063/1.1809090. 8, 22, 61

[Whi76] Whitley, R. M. and Stroud, C. R., Jr.: Double optical resonance. *Phys. Rev. A*, 14:1498–1513 (1976). DOI: 10.1103/PhysRevA.14.1498. 39

[Zen32] Zener, C.: Non-Adiabatic Crossing of Energy Levels. *Proceedings of the Royal Society of London. Series A*, 137(833):696–702 (1932). 80

[Zwi05] Zwierlein, M. W.; Abo-Shaeer, J. R.; Schirotzek, A.; Schunck, C. H.; and Ketterle, W.: Vortices and superfluidity in a strongly interacting Fermi gas. *Nature*, 435:1047–1051 (2005). DOI: 10.1038/nature03858. 20

Danksagung

Der letzte Teil dieser Arbeit ist all jenen gewidmet, die mich während meiner Zeit am Institut unterstützt und somit zum Gelingen dieser Dissertation beigetragen haben.

Tilman Pfau danke ich für die Aufnahme an sein Institut und die Möglichkeit sowohl die Diplomarbeit als auch die Doktorarbeit unter seiner Ägide anzufertigen. Vielen Dank für die vielen guten Ideen, die stets offene Tür und die unerschöpfliche Motivation.

Charles Adams danke ich für die Übernahme des Mitberichts meiner Arbeit und für die daraus entstandenen Diskussionen, die bei mir zu einem tieferen Verständnis der Materie beigetragen haben.

Hans Peter Büchler danke ich für die Übernahme des Vorsitzes der mündlichen Prüfung und seine Geduld bei den Gesprächen mit uns Experimentalphysikern.

Robert Löw danke ich für den Aufbau des Experimentes und dafür, dass er die Schnittstelle zwischen den vielen guten Ideen und der experimentellen Welt gebildet hat. Des Weiteren vielen Dank für die Diskussionen, die bayrische Art („Des baast scho'“) und die Fourier-Ebene.

Rolf Heidemann danke ich ebenfalls für die unzähligen Gespräche, seine Hilfsbereitschaft und Fähigkeit die komplizierten Sachverhalte so herunterzubrechen, dass sie verständlich werden. Vielen Dank für die Steuer- und Auswerteprogramme und die vielen anderen experimentellen und theoretischen Grundlagen auf die sich diese Arbeit stützt.

Vera Bendkowsky danke ich für die Pflege der diversen Lasersysteme, die Hilfe bei den Veröffentlichungen und die wertvollen Diskussionen.

Björn Butscher danke ich für den unermüdlichen Einsatz am Experiment

und seine stets heitere Art und dafür, dass er immer den Eindruck vermittelte als würde ihm auch die langweilgste Aufgabe Spaß machen.

Hendrik Weimer danke ich für die vielen Versuche die Theorie so zu erklären, dass ich sie verstehen konnte. Es war nicht vergebens.

Helmar Bender und **Peter Kollmann** danke ich für ihre Hilfe am Experiment während ihrer Diplomarbeiten.

Jürgen Stuhler danke ich für die Unterstützung während der Anfangszeit meiner Doktorarbeit und den hervorragenden Frühstücksvortrag, den ich in Appendix B übernehmen durfte.

Kevin Weatherill und **Richard Abel** danke ich für die sprachlichen Korrekturen der vorliegenden Arbeit. Des Weiteren danke ich **Mark Bason** und **Jonathan Pritchard** für die Einweihung in die Besonderheiten der englischen Sprache.

Karin Otter, **Sylvia Tassy**, **Nadine Prellwitz** und **Oliver Nagel** danke ich dafür, dass sie für mich den Kampf gegen die Windmühlen der universitären Bürokratie übernahmen.

Dem gesamten **PI 5** danke ich für die familiäre Atmosphäre, die Hilfsbereitschaft und die Freundschaft.

Dem **deutschen Steuerzahler** danke ich für die finanzielle Unterstützung durch das Stipendium nach dem Landesgraduiertenförderungsgesetz. Desweiteren Danke ich **Wilfried Roth** für die administrative Unterstützung das Stipendium betreffend.

Am Ende, aber nicht zuletzt, geht ein großer Dank an meine Familie, die mich in all den Jahren unterstützt hat und den zweiten Pol in meinem Leben bildet.

Durham, der 19. November 2008